Radiative Tau Production and Decay

Thesis by
Dolly Yu-ting Wu

In Partial Fulfillment of the Requirements
for the Degree of
Doctor of Philosophy

California Institute of Technology
Pasadena, California

1990
(Submitted April 24, 1990)

Abstract

A study of the muon decay channel of the τ lepton with the presence of a photon has been carried out to verify theoretical predictions for the production rate of $e^+e^- \rightarrow \tau^+\tau^-\gamma$ and for the branching ratio of $\tau^- \rightarrow \nu_\tau \mu^- \bar{\nu}_\mu \gamma$. Included in this study is the first direct measurement of radiative tau decay. Using e^+e^- annihilation data taken at 29 GeV center-of-mass energy with the Mark II detector, we find the ratio of the measured $\tau^- \rightarrow \nu_\tau \mu^- \bar{\nu}_\mu \gamma$ branching fraction to the expected value from QED to be 1.03 ± 0.42. The ratio of measured-to-predicted number of events from radiative τ production, $e^+e^- \rightarrow \tau^+\tau^-\gamma$, where one of the τ's decay to $\mu\nu\bar{\nu}$ is found to be 0.91 ± 0.20. We have not seen an indication of anomalous behavior in radiative tau events.

Acknowledgments

I am most grateful to my parents, particularly to my mom, and hope for lovely days ahead for my parents, sisters and aunts.

Many thanks to all the Mark II members at SLC and PEP for showing me various aspects of high energy physics. Discussions with many people and much prior work described in scores of internal memos and theses have been very useful to this tau analysis.

At Caltech, I thank my advisor, Barry Barish, for many years of support, and Frank Porter, Eric Soderstrom. At SLAC, I'm very indebted to Andy Lankford for helping me get integrated into the Mark II, learn online software, etc etc. I'm very grateful to Martin Perl for an excellent analysis topic, and to Ken Hayes for letting me work on the analysis, for enjoyable chats. Definitely on the fun side: I thank the Mark II group at Berkeley in 1985-86 for their hospitality, jokes and whatnot. My thanks to the American public for (unwittingly) forking over taxes for my graduate studies.

And finally, I'm immensely grateful to Keith Riles.

Table of Contents

Abstract iii

Acknowledgements iv

Table of contents v

List of tables vii

List of figures ix

CHAPTER 1 Introduction 1

1.1 Motivation for a Radiative Tau Investigation 4

1.1.1 One Prong Tau Discrepancy 5

CHAPTER 2 Radiative Tau-Pair Production 9

2.1 Non-radiative Tau-Pair Production 9

2.2 Radiative Tau-Pair Production Cross Section and Kinematics 12

2.3 Tau-Pair Monte Carlo 20

CHAPTER 3 Radiative Tau Decay 26

3.1 Non-radiative Tau Decay 26

3.2 Total Leptonic Tau Decay Width 27

3.3 Differential Decay Width For Inner Bremsstrahlung 33

3.4 Monte Carlo Simulation of Radiative Tau Decay 34

3.5 Numerical Results for Radiative Tau Decay Process 37

3.6 Kinematics of Radiative Tau Decay Process 39

CHAPTER 4 The Mark II Detector 43

4.1 Introduction to the Mark II Detector 44

4.2 Momentum Measurement 45

4.3 Time-of-Flight System 48

4.4 Central Electromagnetic Calorimeter 50

4.4.1 Muons, Photons and Calorimeter Performance 53
4.5 Endcap Calorimeter 62
4.6 Muon Detector 62
4.6.1 Muon Detection Efficiency and Pion Misidentification 63
4.7 Small Angle Luminosity Monitor 68
4.8 Mark II Trigger 69
CHAPTER 5 Data Analysis 73
5.1 Characteristics of Tau Events 73
5.2 Event Selection Criteria 74
5.3 Background Rejection 75
5.4 Estimates of Signal and Background Contributions 80
5.5 Corrections for Monte Carlo Simulation 81
5.6 Analysis Results: Radiative Tau Decay 83
5.6.1 Radiative Tau production 89
5.7 Cross-checks on Results 91
CHAPTER 6 Discussion 94
6.1 Summary of Results 94
6.1.1 Radiative Tau Decay at Other Energies 94
APPENDIX A Appendix 97
A.1 Decay Channels in the Tau-Pair Monte Carlo 97
A.2 Details of Signal and Background Contribution Estimates 98
A.2.1 Radiative Tau-Pair Production 98
A.2.2 Radiative Tau Decay 100
A.2.3 Misidentified Tau Processes 100
A.2.4 Radiative Mu-Pair Processes 104
A.2.5 Two-Photon Processes 107
A.2.6 Miscellaneous Small Backgrounds 112

REFERENCES 115

List of Tables

1.1	One-charged-prong tau branching ratios	7
2.1	The $\cos\theta$ distribution for initial state photons	16
3.1	Magnitude of corrections to $B(\tau^- \rightarrow \nu_\tau \mu^- \bar{\nu}_\mu)$	32
4.1	Detector components	47
5.1	Estimated contributions from signal and background processes	82
5.2	Results of the likelihood calculation to extract a signal	86
6.1	Radiative tau decay at other center-of-mass energies	95
A.1	Tau branching ratios used by LULEPT	98
A.2	Detection efficiency for radiative tau-pair production	99
A.3	Detection efficiency for radiative tau decay to the muon mode	101
A.4	Sample pion decay and punchthrough probabilities	102
A.5	Detection efficiency for radiative mu-pair production	104

List of Figures

1.1	Examples of permitted weak couplings in the lepton sector	4
2.1	Lowest order diagram for tau-pair production	11
2.2	Diagrams for tau-pair production with emission of a real photon	13
2.3	Diagrams of tau production with virtual bremsstrahlung	14
2.4	Distribution of $\cos\theta$ for photons in radiative tau production	17
2.5	Photon energy spectrum for initial and final state radiation	18
2.6	The $\cos\theta$ distribution of tau pairs	21
2.7	Tau momentum spectrum in radiative tau-pair production	22
2.8	Distribution of the radiative tau-pair acollinearity	23
2.9	Mass of the tau and the photon	24
2.10	Mass of the muon from tau decay and photon from production	24
2.11	Mass of the muon and photon again, now with acceptance cuts	25
3.1	General diagram of tau decay	27
3.2	Muonic tau decay via the weak interaction	28
3.3	Point four-fermion diagram of tau decay	30
3.4	Examples of virtual QED correction to muonic tau decay	31
3.5	Diagrams of tau decay accompanied by the emission of real photons	32
3.6	Energy spectrum of photons emitted in radiative tau decay	40
3.7	Energy spectrum of muons in radiative and non-radiative tau decay	41
3.8	Angle between the muon and photon in radiative tau decay	42
3.9	The μ-γ mass from radiative tau production and decay	42
4.1	The Mark II detector	46
4.2	Wire configuration of vertex chamber inner layers	47
4.3	Main drift chamber wire configuration	49

4.4	Momentum spectrum for Bhabha tracks	50
4.5	Time-of-flight acceptance	51
4.6	Cutaway view of a liquid argon calorimeter module	52
4.7	Ganging scheme for liquid argon calorimeter channels	53
4.8	Longitudinal shower profiles for electrons	55
4.9	Transverse shower profile for electrons	56
4.10	Energy residuals for the barrel calorimeter	57
4.11	Photon detection efficiency	58
4.12	Photon detection efficiency near the edges of the calorimeter	59
4.13	Level of electronic noise in the calorimeter	60
4.14	Energy deposited in the calorimeter by muons	60
4.15	Position resolution of showers in the calorimeter	61
4.16	Cross section of a muon proportional tube module	63
4.17	Position residuals for the muon system	65
4.18	Muon identification efficiency	66
4.19	Position of the walls in the muon system	67
4.20	Side view of the Small Angle Tagger(SAT)	69
4.21	Probability of electronic noise in SAT calorimeter	70
4.22	Probability of electronic noise in SAT calorimeter plus gross counter	70
4.23	Hardware charged track finding	72
5.1	Energy balance along the beam direction	76
5.2	Total visible energy for two-photon, muon and tau-pair processes	77
5.3	χ^2 spectrum for $e^+e^- \rightarrow \mu^+\mu^-\gamma$ kinematic constraint	78
5.4	Missing mass calculated from charged tracks only	79
5.5	χ^2 spectrum for $e^+e^- \rightarrow \mu^+\mu^-\gamma(\gamma)$ kinematic constraint	79
5.6	μ-γ mass spectra of the background processes	85
5.7	Data and fitted μ-γ mass spectra	87

5.8 A candidate data tau event with μ-γ mass of 0.22 GeV 87
5.9 Data and Monte Carlo mass spectrum from $\tau^- \to \nu_\tau \rho^-$ events 89
5.10 A candidate data tau event with μ-γ mass of 1.65 GeV 90
5.11 Photon energy spectrum from the data and expected contributions 91
5.12 Likelihood function vs B($\tau^- \to \nu_\tau \mu^- \bar{\nu}_\mu \gamma$) 93
A.1 Agreement between data and Monte Carlo $e^+e^- \to \mu^+\mu^-\gamma(\gamma)$ events 106
A.2 Feynman diagrams for the $e^+e^- \to e^+e^-\mu^+\mu^-$ process 108
A.3 Fit functions for μ-γ mass spectrum for $e^+e^- \to e^+e^-\mu^+\mu^-\gamma$ events 111
A.4 Minimum charged multiplicity-per-hemisphere in hadronic events 113
A.5 Maximum charged multiplicity-per-hemisphere in hadronic events 113
A.6 μ-γ mass distribution for "fake" photons 114

Chapter 1

Introduction

This thesis examines the production of the tau (τ) lepton and its decay via the weak interaction to the muon lepton, when the muon is accompanied by a detectable nearby photon. Chapters 2 and 3 describe the physics of radiative tau production and decay, respectively. The Mark II detector at the PEP e^+e^- collider facility, with which the data were taken, and the detector performance are described in Chapter 4. Finally, Chapter 5 summarizes the strategy and the analysis to measure radiative tau production and decay, involving the muon channel. The Appendix gives the details of the estimation of the various signal and background detection efficiencies. Provided below is a brief introduction to elementary particles physics and the motivation for a radiative tau study.

Elementary particles are classified as leptons, quarks, or gauge bosons and they participate in the electromagnetic, weak, strong and/or gravitational interactions. Presently, there are three known families of leptons, which may be grouped in weak doublets,

$$\begin{pmatrix} e \\ \nu_e \end{pmatrix} \qquad \begin{pmatrix} \mu \\ \nu_\mu \end{pmatrix} \qquad \begin{pmatrix} \tau \\ \nu_\tau \end{pmatrix}$$

three families of quarks:

$$\begin{pmatrix} u \\ d \end{pmatrix} \qquad \begin{pmatrix} c \\ s \end{pmatrix} \qquad \begin{pmatrix} t \\ b \end{pmatrix}$$

and three types of gauge bosons:

$$(\text{photon}),\ (W^{\pm},\ Z^{0}),\ (\text{gluons}).$$

The quarks and leptons have spin $\frac{1}{2}$ and the bosons spin 1.

Only the quarks participate in the strong interaction, which occurs on a typical time scale of 10^{-23} seconds and is mediated by gluons. The strong interaction has a quantum number, called color, which is conserved in such a way that quarks and gluons, which are singly colored, cannot be free particles; only certain combined colors exist as free particles (*e.g.*, the proton is RBG (red, blue, green and the pion is $R\bar{R} + B\bar{B} + G\bar{G}$).

Both leptons and quarks participate in the electroweak process which consists of the electromagnetic and weak interactions, occurring at time scales of $\sim\ 10^{-16}$ sec and $>\ 10^{-12}$ sec, respectively. Any particle carrying electric charge can participate in the electromagnetic process, mediated by a virtual photon. This process can, however, create a non-charged particle, a real photon. For example, in $e^{+}e^{-} \rightarrow \tau^{+}\tau^{-}$, the colliding electron and positron may emit real photons (called initial state radiation), or the emerging taus may radiate (called final state radiation), or photons may emerge during tau decay (decay radiation). There is interference between initial and final state radiation; whereas the interference between production (initial or final state) and decay radiation is negligible because the tau decays only via the weak interaction, which is much slower than the electromagnetic process. The aspects of quantum electrodynamics (QED) relevant to this thesis are given in the next chapter.

The weak interaction is unusual and does not have its own ad hoc quantum number like electric charge and color, though it does have mediating particles, the $W^{\pm}$ and Z^{0}. The weak process conserves lepton flavor at the interaction vertex; so for example in the lepton sector, the coupling of a charged lepton is permitted only

with itself or with its neutrino partner – *i.e.*, coupling within the same family only (see fig. 1.1). For quarks, the situation is a little different. The Z^0 still allows quarks to couple with themselves, but the $W^{\pm}$ allows coupling between *any* member of the upper row with *any* member of the lower row in the quark doublets shown earlier, though favoring coupling within the same family. Direct coupling of different quarks of only the upper row or of only the lower row is not observed (*e.g.*, the d and s quarks do not couple at the same vertex; so phenomena like $K^0 - \bar{K}^0$ mixing proceeds only via higher order weak diagrams). The $W^{\pm}$ allows transitions between leptons and quarks, such as b quark to tau lepton through a W boson, where in addition to the tau, the process produces a tau anti-neutrino and one quark such as charm ($b \rightarrow \tau \bar{\nu_\tau}\, c$).

In the low-energy limit, such as at $E_{cm} = 29$ GeV, the effects of the massive $W^{\pm}$ and Z^0 propagators are very small (see Chapters 2 and 3) and for many years the weak interaction was approximated by a point-like process occurring with strength proportional to the Fermi constant. In Chapter 2, we'll see that the large mass of the W allows the use of leptonic-decay-width calculations based on a point-like interaction.

The charged "current," *i.e.*, transition probability mediated by the W boson, features a vector and axial vector (V–A) nature, but the neutral current (mediated by the Z^0) permits both V–A and V+A components. The mixture of V and A interactions implies the weak process violates parity (P). The weak interaction also violates charge conjugation (C) and the combination CP.

A major consequence of the V–A form of the weak current, one important in understanding $\tau^- \rightarrow \nu_\tau\, \mu^-\, \bar{\nu}_\mu$ events, is that only the left-handed components of the leptons participate in the interaction. The effects of spin and helicity on the kinematics of tau events are discussed in Chapters 2 and 3.

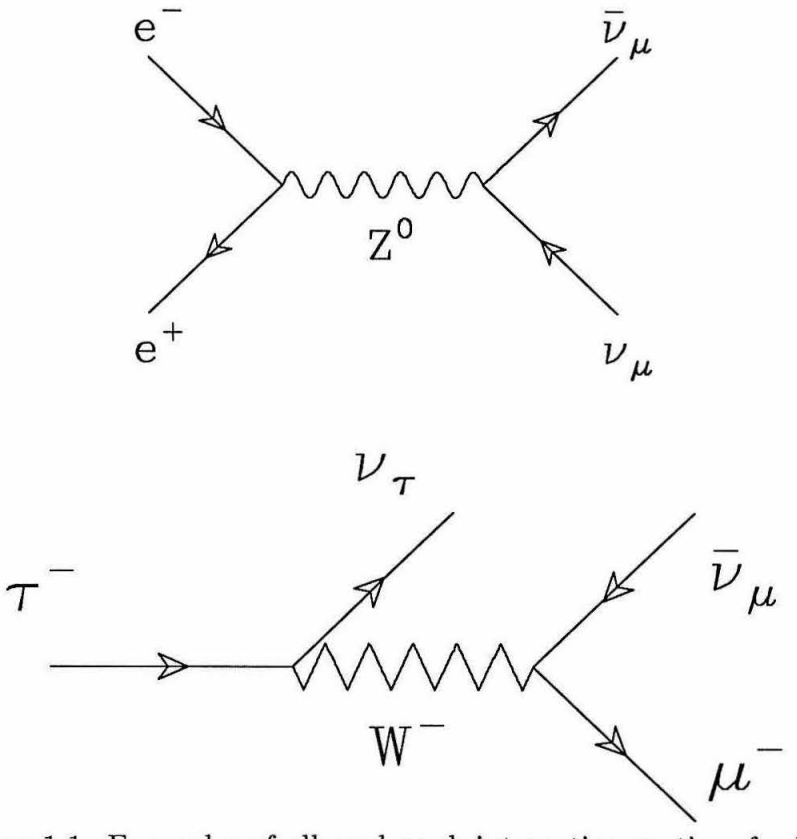

Figure 1.1. Examples of allowed weak interaction vertices for leptons. Charged and neutral leptons can only couple to themselves as in the Z^0-mediated diagram, or couple to their doublet partner as in the W-mediated graph.

1.1 Motivation for a Radiative Tau Investigation

The tau lepton has a mass of 1.784 GeV and decays to many modes via the weak interaction with a mean lifetime of 3.04×10^{-13} sec. The very success in understanding weak decays and in measuring the properties of the tau (see tau reviews ref. 1, ref. 2, ref. 3) has also led to the uncovering of a possible problem. There seems to be a discrepancy between the measured *inclusive* one-charged prong tau branching ratios (B_1) and the sum of the *exclusive* branching ratios ($\sum B_i$).[4-6] The discrepancy is described in more detail in the next section. The experiments at CESR and Beijing in this decade will be able to measure the tau branching ratios much more precisely

and shed new light on the problem. Until then, this radiative tau study is carried out with the following motivation:

- Verify QED in tau production and decay, including the expected magnitude of decay radiation. In the past, Monte Carlo estimates of tau event detection efficiencies have not accounted for radiative decay[6] (in some analyses photons were not allowed to be near the tagged charged track). Sometimes even the larger contribution from final state radiation was not included (most pre-1984 tau Monte Carlos do not include final-state radiation).[7–10] In particular, one other radiative tau production analysis has been carried out in 1986 by the Jade Collaboration which considered many decay modes and required at least one isolated photon well separated (by about 30 degrees) from the other decay products of the tau.[11] This analysis will instead examine the case where a photon is emitted within 1.8–90 degrees of the muon from tau decay.
- Investigate whether accounting for conventional decay radiation is important to the one-prong tau discrepancy. For the muon channel with a detectable photon, detectable decay radiation is expected to occur at the level of a percent of the total decay rate to $\mu\nu\bar{\nu}$,[12] which would be too small to affect presently measured tau branching ratios.
- Look for anomalous radiation (aside from conventional QED predictions) as a source of the one-prong discrepancy. Future radiative tau measurements will provide a more definitive test of this possibility, given higher statistics and a more refined detector. The issues considered in the present analysis will be relevant to those future studies.

1.1.1 One Prong Tau Discrepancy

The one-charged-prong tau decay problem refers to the discrepancy between the measured *inclusive* one-charged prong branching ratio (B_1) and the sum of the

exclusive branching ratios ($\sum B_i$). The discrepancy is a ~3 sigma effect, on the order of 6±2%, and is apparent only when theoretically predicted branching ratios are substituted for decay modes that are unmeasured or measured with large errors such as $\tau^{\pm} \rightarrow \pi^{\pm}(\geq 3\pi^0)\nu_\tau$. Many references describe this problem in great detail (see ref. 6, ref. 13, ref. 14). Reference 14 provides one way of summing the exclusive modes, combining the measured and calculated branching ratios as shown in Table 1.1 to give $\sum B_i \approx (80.4 \pm 1.8)\%$. The calculated values are normalized to the electronic tau decay branching ratio, which was obtained from a constrained fit to $\tau^- \rightarrow \nu_\tau e^- \bar{\nu}_e$ and $\tau^- \rightarrow \nu_\tau \mu^- \bar{\nu}_\mu$ measurements[13] with $B_\mu = .973B_e$. In addition, the calculations include $O(\alpha)$ radiative corrections in the decay process which are on the order of a percent of the decay width for each decay mode[12] (see Chapter 3 for the calculation for the muon decay mode). The inclusive branching ratio $B_1 = (86.0\pm0.3)\%$ includes the 1989 HRS and CELLO experimental values, which lowered the 1988 world average B_1 value of $(86.6 \pm 0.3)\%$ by 0.6%.

The methods of calculating the theoretical branching ratio values, given in Table 1.1, are summarized in ref. 2, ref. 4, and ref. 15. The theoretical values typically require information from experimental measurements; for example, the calculation for $B(\tau^- \rightarrow \nu_\tau \mu^- \bar{\nu}_\mu)$ requires the measured value of the tau lifetime (see Chapter 3). For decay modes with many hadrons, various rules are invoked to "calculate" the decay widths; for example, the conserved-vector current theorem relates the decay width of $\tau^- \rightarrow \nu_\tau + \pi^- + \pi^0 + \pi^0 + \pi^0$ to the cross section for $e^+e^- \rightarrow \pi^- + \pi^+ + \pi^- + \pi^+$, which is measured independently.

The cause of the discrepancy is unknown, and being only a ~3 sigma effect (though it is nearly 5 sigma if the calculated branching ratio for $\tau^- \rightarrow \pi^- 2\pi^0 \nu_\tau$ is substituted for the measured value), it is not necessarily even a real "problem." The solution may just require hard work on the part of individual experiments with high statistics to simultaneously measure the branching ratios for all decay modes, though

Table 1.1. One-charged-prong tau branching ratios from ref. 14. The calculated values are normalized to the electronic tau decay branching ratio, which is obtained from a constrained fit to $\tau^- \rightarrow \nu_\tau\, e^-\, \bar{\nu}_e$ and $\tau^- \rightarrow \nu_\tau\, \mu^-\, \bar{\nu}_\mu$ measurements[13] with $B_\mu = .973 B_e$. The uncertainty in the branching ratios includes both statistical and systematic errors.

Decay Mode	Experiment	Theory
$e^-\nu\nu$	$17.7 \pm .4$	18.0
$\mu^-\nu\nu$	$17.7 \pm .4$	17.5
$\rho^-\nu$	$22.3 \pm .8$	22.7
$\pi^-\nu$	$10.8 \pm .6$	10.8
$K^-(\geq 0\ neutrals)\nu$	$1.71 \pm .29$	
$K^{*-}\nu,\ K^{*-} \rightarrow \pi^-(2\pi^0$ or $K_L)$	$.6 \pm .1$	
$\pi^-(2\pi^0)\nu$	7.4 ± 1.4	$\leq 6.7 \pm .4$
$\pi^-(\geq 3\pi^0)\nu$		< 1.4
$\pi^-(\geq 1\eta)(\geq 0\pi^0)\nu$		$< .8$
Sum of measured modes		78.2 ± 1.8
Theoretical limits on ummeasured modes		< 2.2
Sum of exclusive modes		$\leq 80.4 \pm 1.8$
Measured 1-prong branching ratio B_1		$86.0 \pm .3$
Difference		$> 5.6 \pm 1.8$

without constraining the sum of them to be unity (*e.g.*, as the CELLO collaboration has attempted[16]).

One area of difficulty in the measurement of branching ratios is the accounting of photons. There are two dominant sources of photons in tau events, one from the

decay of π^0's (in hadronic tau decays), and the other from QED. Unfortunately, the statistics of the Mark II data do not permit a precision measurement of the branching ratios for the hadronic modes with a precise accounting of the neutrals in the event and the identification of the hadron. The reliability of identifying a charged particle as a hadron (not even to say whether it is a kaon, pion, etc.) is generally poorer than for lepton identification. The counting of the number of photons and the identification of their sources (*i.e.*, radiative processes vs $\pi^0 \rightarrow 2\gamma$ decay) are also very difficult because of the merging of the two photons in the calorimeter and the accuracy of the Monte Carlo simulation of hadronic showers, etc. Hadronic tau decay events contain photons due both to π^0 decay and to radiative processes. To measure the contribution from QED processes alone and the detection efficiency of such events, it is easier to study the muonic tau decays, where it is possible to detect photons emitted very near the muon, and where the photon may only be from radiative processes (or from new physics).

Chapter 2

Radiative Tau-Pair Production

The lowest order production of tau leptons via e^+e^- annihilation $e^+e^- \rightarrow \tau^+\tau^-$ and some of its basic characteristics such as angular asymmetry and spin correlations are discussed first in this chapter. The remainder of this chapter is then devoted to the subject of tau production with the emission of a real photon. The order α^3 QED process $e^+e^- \rightarrow \tau^+\tau^-\gamma$ is expected to give the largest contribution to radiative tau event candidates. Monte Carlo event simulations are a convenient way of including effects like spin correlation, radiative corrections, etc., in an overall estimate of event detection efficiency. Therefore, the main tau Monte Carlo KORALB[17], used in this thesis analysis is presented and discussed in parallel with the tau event characteristics which are accurately modeled by KORALB at $E_{cm} = 29$ GeV. The number of expected events from radiative tau production and many event distributions (*e.g.*, photon energy) predicted by KORALB are provided in the last section.

2.1 Non-radiative Tau-Pair Production

Tau leptons are produced at e^+e^- annihilation experiments through a virtual photon or Z gauge boson as shown in fig. 2.1. At $E_{cm} = 29$ GeV, the main contribution is through the virtual photon, with a lowest order QED cross-section equation of

$$\sigma_0(s) = \frac{4\pi}{3}\frac{\alpha^2}{s}Q_f^2. \tag{2.1}$$

For the production of a point-like charged ($Q_f = 1$ for τ) fermion-antifermion pair at center of mass energy $\sqrt{s}$=29 GeV, where α is the fine structure constant, the cross section is $\sim$ 0.103 nb. Accounting for the tau mass (M_τ) introduces an additional factor which has a value very nearly one in the production cross-section:

$$\sigma_0(s) \equiv \sigma(e^+e^- \rightarrow \tau^+\tau^-) = \frac{4\pi}{3}\frac{\alpha^2}{s}\left[\frac{\beta(3-\beta^2)}{2}\right] \quad ; \quad \beta \equiv \sqrt{1-\left(\frac{M_\tau}{E_B}\right)^2} \tag{2.2}$$

where E_B is the beam energy and β the final speed of the τ in the center of mass. Differential forms of the cross section equation, such as

$$\frac{d\sigma(e^+e^- \rightarrow \tau^+\tau^-)}{d\Omega_{\tau^-}} = \frac{1}{4}\frac{\alpha^2}{s}\beta[1+\cos^2\theta+(1-\beta^2)\sin^2\theta] \tag{2.3}$$

where $d\Omega_{\tau^-} \equiv d(\cos\theta)d\phi$, with θ and ϕ the polar and azimuthal angles of the τ^-, provide insights to the nature of the QED production process. Equation 2.3 is valid for the collision of unpolarized beams (as was the case for the PEP data) and shows that when tau pairs are produced via a virtual photon, the taus emerge symmetrically in θ and uniformly in ϕ. Although there is no net spin orientation (polarization) over all events, the helicity of the two taus are correlated and opposite in each individual event because of helicity conservation when $s \gg m_\tau^2$ and $s \gg m_e^2$.[2] This spin-spin correlation causes the momentum spectra of the decay products of the two taus to be correlated (see Chapter 3) and are accounted for in the main tau-pair Monte Carlo, KORALB[17], used to estimate tau event detection efficiency in this thesis analysis. The process $e^+e^- \rightarrow$ virtual $Z^0 \rightarrow \tau^+\tau^-$ diagram (including interference between the γ and Z^0 diagrams) introduces a forward-backward (angular) asymmetry and a non-zero polarization of the taus because the Z^0 couples to left-handed and right-handed leptons unequally.

The KORALB Monte Carlo includes tau production through the exchange of a photon along with $O(\alpha)$ QED radiative corrections, as will be discussed in the next

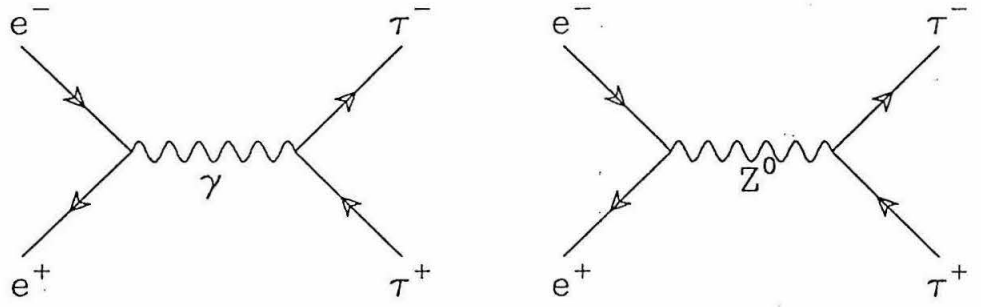

Figure 2.1. Tau-pair production through a virtual photon or Z boson.

section, and tau production through the exchange of the Z boson but only in the lowest order (γ-Z interference) which is needed to reproduce an accurate forward-backward asymmetry. There are also radiative corrections to the Z exchange diagrams but to a very good approximation it is sufficient to neglect both the pure Z amplitude and the radiative corrections to this amplitude for the PEP energy range $E_{cm} = 29$ GeV, as can be seen from the following differential cross section equation which includes the γ, Z, and interference contributions (without any radiative corrections and in a form provided in ref. 18):[19,18]

$$
\begin{aligned}
\frac{d\sigma(e^+e^- \to \tau^+\tau^-)}{d\Omega_{\tau^-}} = & \frac{1}{4}\frac{\alpha^2}{s}\beta\Big[(1+\cos^2\theta+(1-\beta^2)\sin^2\theta) \\
(\gamma - Z\ term:) \quad & + \frac{1}{8\sin^2\theta_W\cos^2\theta_W}\,\frac{s(s-M_Z^2)}{(s-M_Z^2)^2+M_Z^2\Gamma_Z^2} \\
& \times\Big\{(1-4\sin^2\theta_W)^2\left(1+\cos^2\theta+(1-\beta^2)\sin^2\theta\right)+2\beta\cos\theta\Big\} \\
(\ Z\ term:) \quad & + \frac{1}{64\sin^4\theta_W\cos^4\theta_W}\,\frac{s^2}{(s-M_Z^2)^2+M_Z^2\Gamma_Z^2} \\
& \times\Big\{(1-4\sin^2\theta_W+8\sin^4\theta_W)^2(1+\beta^2\cos^2\theta) \\
& -4(1-\beta^2)(1-4\sin^2\theta_W+8\sin^4\theta_W)(\sin^2\theta_W-2\sin^4\theta_W) \\
& +2(1-4\sin^2\theta_W)^2\beta\cos\theta\Big\}\Big]
\end{aligned}
$$

where M_Z and Γ_Z are the mass and total decay width of the Z boson and θ_W is the weak mixing angle. For the values $M_Z \sim 91$ Gev, $\Gamma_Z \sim 2.6$ GeV and $\sin^2\theta_W \sim 0.23$, this becomes at $E_{cm} = 29$ GeV:

$$\frac{d\sigma(e^+e^- \to \tau^+\tau^-)}{d\Omega_{\tau^-}} \approx \frac{1}{4}\frac{\alpha^2}{s}\beta\Big\{(1+\cos^2\theta+(1-\beta^2)\sin^2\theta) - (.00053)(1+\cos^2\theta+(1-\beta^2)\sin^2\theta) + (.17)\beta\cos\theta + (.0018)(1+\beta^2\cos^2\theta) - (.0016)(1-\beta^2) + .00018\beta\cos\theta\Big\}.$$

The Mark II detector is symmetric about θ; the $\cos\theta$ (odd-powers) terms* contribute nothing to the total cross section. All of the terms in the pure Z contribution are much smaller than the pure γ terms; therefore, the pure Z amplitude and radiative corrections to the Z exchange diagram, which are even smaller, are negligible at E_{cm} = 29 GeV. Being small, the electroweak contribution will not be further discussed in the remainder of this chapter.

2.2 Radiative Tau-Pair Production Cross Section and Kinematics

The quantum electro-dynamics (QED) theory has been amazingly successful in predicting many electromagnetic phenomena, such as atomic hyperfine structure and radiative muon decay to very high accuracy. A perturbative approach is used in the calculations of higher order QED diagrams, and its success is due to the smallness of the coupling strength $\alpha \approx 1/137$ between charged particles and the photon. For e^+e^- annihilation at $E_{cm} = 29$ GeV, it is usually necessary to include only the lowest order radiative corrections in order to understand the data to sufficient accuracy.

For the analysis presented in this thesis, it is particularly important to examine the nature of the $O(\alpha^3)$ QED process, $e^+e^- \to \tau^+\tau^-\gamma$, because most of the tau

* The first $\cos\theta$ term gives rise to a measureable forward-backward asymmetry.

event candidates from the data will be from this process, as we'll see in Chapter 5. The diagrams which contribute to the $O(\alpha^3)$ calculation are the lowest order diagram (the left diagram shown in fig. 2.1), the external bremsstrahlung diagrams shown in fig. 2.2, and the virtual bremsstrahlung diagrams shown in fig. 2.3. The virtual bremsstrahlung diagrams, being of $O(\alpha^4)$, contribute to the $O(\alpha^3)$ calculation only through interference with the lowest order diagram.

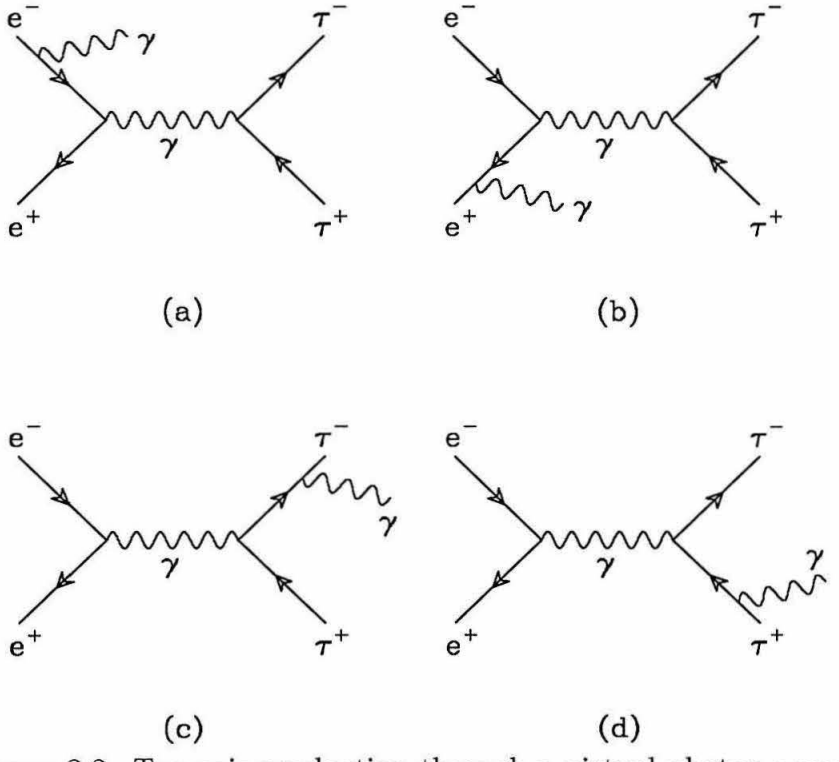

Figure 2.2. Tau-pair production through a virtual photon accompanied by the emission of a *real* photon from the initial-state (a - b), or the final-state (c - d).

Because higher order QED calculations are a perturbative problem, it is appropriate to express the differential cross section for $e^+e^- \rightarrow \tau^+\tau^-(\gamma)^*$ in terms of the

* A parenthesis around the γ is used to indicate that a photon may or may not be detected.

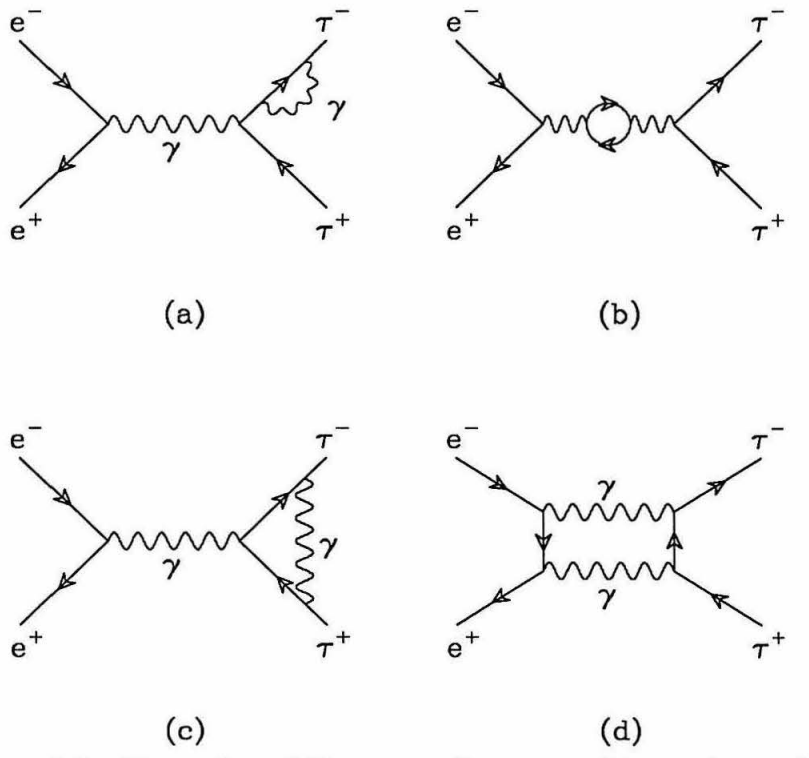

Figure 2.3. Examples of Feynman diagrams of tau-pair production with virtual radiative corrections: (a) fermion self-mass, (b) vacuum polarization where the closed loop represents quarks and leptons, (c) vertex correction, and (d) box diagram.

lowest order QED process, $d\sigma_0(e^+e^- \to \tau^+\tau^-)$:

$$d\sigma(e^+e^- \to \tau^+\tau^-(\gamma)) = d\sigma_0\,(1 \;+\; \delta_{\rm rad}) \tag{2.4}$$

where $\delta_{\rm rad}$ is the radiative correction term. The $\delta_{\rm rad}$ term consists of the sum of the amplitudes from 1) the external bremsstrahlung diagrams (fig. 2.2) and 2) the interference of the basic diagram (left diagram fig. 2.1) with each of the virtual bremsstrahlung processes (fig. 2.3). That is, schematically,

$$\begin{aligned} d\sigma(\alpha^3) &= |(\sqrt{\alpha})^2 R_{\rm basic} \;+\; (\sqrt{\alpha})^3 R_{\rm bremsstrahlung} \;+\; (\sqrt{\alpha})^4 R_{\rm virtual}|^2 \\ &\approx \alpha^2 R^2_{\rm basic} \;+\; \alpha^3 R^2_{\rm bremsstrahlung} \;+\; 2\alpha^3 R_{\rm basic} R_{\rm virtual}. \end{aligned}$$

The α^4 term is neglected and the order α^2 basic term $d\sigma_0$ is factored out to give eqn. 2.4 with

$$\delta_{\rm rad} \equiv \alpha R'^2_{\rm bremsstrahlung} + \alpha R'^2_{\rm virtual}.$$

In the next few paragraphs various forms of the differential and total cross section equations for the external bremsstrahlung diagrams, fig. 2.2, are given to indicate certain characteristics of $e^+e^- \to \tau^+\tau^-\gamma$ events. For the diagrams in fig. 2.2, the differential cross section from Berends *et al.*, written in a form provided by ref. 18, is as follows:[20]

$$d\sigma(e^+e^- \to \tau^+\tau^-\gamma) = \frac{\alpha^3}{4\pi^2 s}\left[A_{\rm ini} + A_{\rm fin} + A_{\rm int}\right] d\Gamma \tag{2.5}$$

where $d\Gamma$ is the Lorentz invariant differential phase space volume:

$$d\Gamma \equiv \frac{d^3q_-}{E_-}\frac{d^3q_+}{E_+}\frac{d^3k}{E_\gamma}\delta^4(p_- + p_+ - q_- - q_+ - k)$$

and the initial state, final state and interference contributions are

$$\begin{aligned} A_{\rm ini} \equiv \frac{1}{\hat{s}_1 x_1 x_2}\Bigg\{ &\left[\hat{t}^2 + \hat{u}^2 + M_\tau^2\frac{(\hat{t}+\hat{u})^2}{\hat{s}_1}\right]\left(1 - \frac{m_e^2 x_1}{\hat{s}_1 x_2}\right) \\ &+ \left[\hat{t}_1^2 + \hat{u}_1^2 + M_\tau^2\frac{(\hat{t}_1+\hat{u}_1)^2}{\hat{s}_1}\right]\left(1 - \frac{m_e^2 x_2}{\hat{s}_1 x_1}\right)\Bigg\} \end{aligned} \tag{2.6}$$

$$\begin{aligned} A_{\rm fin} \equiv \frac{1}{\hat{s} y_1 y_2}\Bigg\{ &\left[\hat{t}^2 + \hat{u}_1^2 + M_\tau^2\hat{s}\right]\left[1 - \frac{M_\tau^2}{\hat{s}}\left(1 + \frac{y_1}{y_2}\right)\right] \\ &+ \left[\hat{u}^2 + \hat{t}_1^2 + M_\tau^2\hat{s}\right]\left[1 - \frac{M_\tau^2}{\hat{s}}\left(1 + \frac{y_2}{y_1}\right)\right] \\ &+ \frac{M_\tau^2}{\hat{s}}(x_1^2 + x_2^2) - 4M_\tau^2(\hat{s} - \hat{s}_1)\Bigg\} \end{aligned} \tag{2.7}$$

$$\begin{aligned} A_{\rm int} \equiv \frac{1}{\sin\theta \hat{s}_1 x_1 x_2 y_1 y_2}\Bigg\{ &(\hat{t} x_2 y_2 + \hat{t}_1 x_1 y_1 - \hat{u} x_2 y_1 - \hat{u}_1 x_1 y_2) \\ &\times \left[\hat{t}^2 + \hat{t}_1^2 + \hat{u}^2 + \hat{u}_1^2 + M_\tau^2(\hat{s} + \hat{s}_1)\right] \\ &+ M_\tau^2 x_1 x_2\left[(\hat{s} - \hat{s}_1)(\hat{t} + \hat{t}_1 - \hat{u} - \hat{u}_1) - (x_1 - x_2)(y_1 - y_2)\right]\Bigg\} \end{aligned} \tag{2.8}$$

where p_-, p_+, q_-, q_+, and k are the 4-momenta of the e^-, e^+, τ^-, τ^+, and γ, respectively, and E_-, E_+, and E_γ are the final particle energies. The Lorentz invariant quantities are defined by:

$$\hat{s} \equiv p_- \cdot p_+ \qquad \hat{t} \equiv p_- \cdot q_- \qquad \hat{u} \equiv p_- \cdot q_+$$

$$\hat{s}_1 \equiv q_- \cdot q_+ + M_\tau^2 \qquad \hat{t}_1 \equiv p_+ \cdot q_+ \qquad \hat{u}_1 \equiv p_+ \cdot q_-$$

$$x_1 \equiv p_- \cdot k \qquad y_1 \equiv q_- \cdot k$$

$$x_2 \equiv p_+ \cdot k \qquad y_2 \equiv q_+ \cdot k$$

The initial state eqn. 2.6 and final state eqn. 2.7 pieces contain a $1/(x_1x_2)$ or $1/(y_1y_2)$ factor indicating that radiation is largest when the photon emerges nearly parallel to one of the fermions. Reference 21 provides a useful table for the angular distribution of initial state radiation based on a Bonneau and Martin[22] calculation. Table 2.1 shows that initial state radiation is emitted mostly in the beam direction as claimed earlier (see also fig. 2.4). Equation 2.5 clearly can be used for radiative mu-pair production as well by substituting the muon mass for the tau mass M_τ. As the mass of the final lepton grows in the $e^+e^- \rightarrow \text{lepton}^+\text{lepton}^-\gamma$ process, the total amount of initial and final state radiation, both, decrease. The initial state decreases because it is no longer kinematically possible to emit a photon very near the beam energy and still produce a lepton of high mass; and the final state radiation diminishes for heavier leptons because they are accelerated less under the influence of the same electromagnetic forces.

Table 2.1– The probability P(x) for initial state radiation to be emitted at $|\cos\theta| > x$ at $E_{cm} = 29$ GeV, from ref. 21.

x	.7	.8	.9	.99	.9999
P(x)	.92	.90	.86	.74	.53

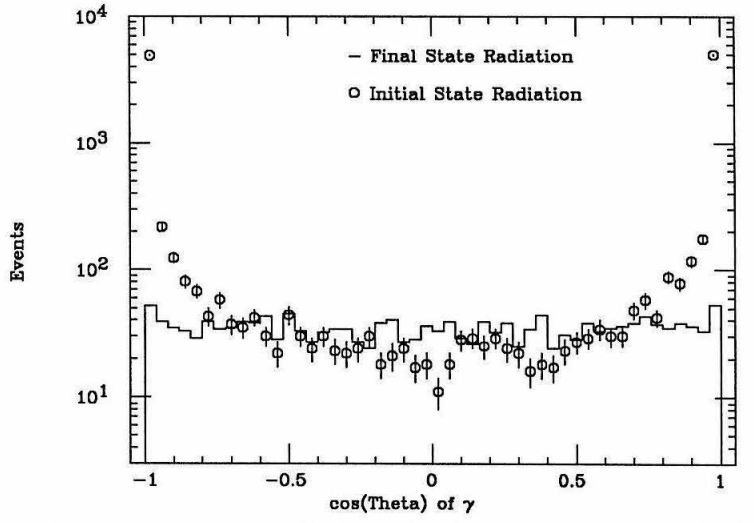

Figure 2.4. The $\cos\theta$ distribution for initial state and final state radiation.

Equation 2.5 can be integrated over all solid angle to give a total initial state and final state contribution (the integral of the interference term is zero):[20]

$$\begin{aligned}
\frac{d\sigma_{\text{ini}}}{d\kappa} &= \sigma_0 \frac{2}{\beta(3-\beta^2)} \beta_{\text{ini}} \frac{1+(1-\kappa)^2}{4\kappa(1-\kappa)} v(\kappa)\left[3-v^2(\kappa)\right] \\
\frac{d\sigma_{\text{fin}}}{d\kappa} &= \sigma_0 \frac{2}{\beta(3-\beta^2)} \frac{\alpha}{\pi}\frac{1}{\kappa}\left\{\left[1+(1-\kappa)^2-\mu^2\kappa-\frac{\mu^4}{2}\right]\ln\left(\frac{1+v(\kappa)}{1-v(\kappa)}\right)\right. \\
&\qquad \left. - v(\kappa)\left[\kappa^2+(2+\mu^2)(1-\kappa)\right]\right\}
\end{aligned} \tag{2.9}$$

where E_B is the beam energy, $\kappa \equiv E_\gamma/E_B$, and

$$\mu \equiv \frac{M_\tau}{E_B} \qquad \beta_{\text{ini}} \equiv \frac{2\alpha}{\pi}\left[\ln\frac{s}{m_e^2}-1\right]$$

and

$$v(\kappa) \equiv \left(1-\frac{\mu^2}{1-\kappa}\right)^{\frac{1}{2}}.$$

Reference 18 provides useful plots for these in fig. 2.5 for $e^+e^- \to \mu^+\mu^-\gamma$ and $e^+e^- \to \tau^+\tau^-\gamma$. The plots show that at very high photon energies the initial state contribution rises more for the smaller muon mass case because of kinematics, as explained earlier

and the peak results from the $(1-\kappa)$ term in the denominator.* At $E_{cm} = 29$ GeV, the $O(\alpha^3)$ cross section for mu-pair production is 165 pb and only 135 pb for tau pairs because of more energetic initial state radiation in the muon case. The difference can be understood from eqn. 2.1, showing that the basic cross section depends inversely on the center of mass energy. When a very energetic initial state photon is emitted, the electron and positron collide at a lower center of mass energy $(= \sqrt{s'})$, causing the interaction cross section to grow:

$$\sigma_0[s'] = \sigma_0[s(1-\kappa)] \propto \frac{1}{s(1-\kappa)}.$$

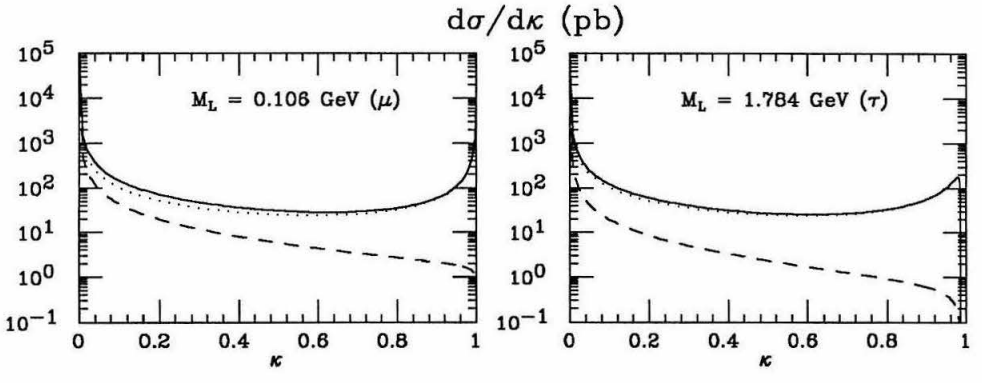

Figure 2.5. The photon energy spectrum for initial (dotted) and final (dashed) state radiation and the total (solid) for the radiative production of muon and tau pairs.

At small κ, low photon energies, eqn. 2.9 falls off like $1/\kappa$. This form results in the famous infrared divergence problem for soft bremsstrahlung. There is also an

* The photon spectrum for candidate events usually do not show such a rise and the spectrum behaves more like $1/\kappa$ because very large initial state radiation causes the tau pairs to be emitted very acollinearly, causing the event kinematics to fail the selection criteria discussed in Chapter 5.

infrared divergence associated with virtual photon emission which cancels the soft photon divergence to give a finite valued radiative correction $\delta_{\rm rad}$.[23] Because of the divergence, eqn. 2.9 is normally integrated from an arbitrary low value cutoff, $E_{\gamma_{\rm min}}$, to the maximum kinematically allowed photon energy of

$$E_{\gamma_{\rm max}} = E_B \left[1 - \left(\frac{M_\tau}{E_B}\right)^2\right] \tag{2.10}$$

to give (the form provided in ref. 18)[20]

$$\sigma_{\rm ini}(\kappa_0 \leq \kappa \leq \kappa_{\rm max}) = \sigma_0 \beta_{\rm ini}\left\{\ln\frac{1}{\kappa_0} - \frac{4}{3} + \ln\frac{4\beta^2}{\mu^2} + \frac{1}{\beta(3-\beta^2)}\ln\frac{\mu^2}{(1+\beta)^2}\right\} \tag{2.11}$$

$$\begin{aligned}\sigma_{\rm fin}(\kappa_0 \leq \kappa \leq \kappa_{\rm max}) = \sigma_0 \Bigg\{ & \beta_{\rm fin}\ln\frac{1}{\kappa_0} \\ & + \frac{\alpha}{\pi}\Bigg[\frac{2(1+\beta)^2}{\beta}\Bigg[{\rm Li}_2\left(\frac{1-\beta}{1+\beta}\right) - {\rm Li}_2\left(\frac{1-\beta}{2}\right) \\ & - \frac{\pi^2}{12} - \frac{1}{2}\ln\left(\frac{1+\beta}{2}\right)\ln\left(\frac{(1-\beta)^2}{2(1+\beta)}\right)\Bigg] \\ & + \beta(3-\beta^2)\ln\left(\frac{1-\beta^2}{4\beta^2}\right) + \frac{39}{8}\beta - \frac{17}{8}\beta^3 \\ & + \frac{1}{16}(9 - 2\beta^2 + \beta^4)\ln\left(\frac{1+\beta}{1-\beta}\right)\Bigg]\Bigg\}\end{aligned} \tag{2.12}$$

where $\kappa_0 \equiv E_{\gamma_{\rm min}}/E_B$, $\kappa_{\rm max} \equiv E_{\gamma_{\rm max}}/E_B$ and

$$Y \equiv \ln\left(\frac{(1+\beta)^2}{\mu^2}\right) \qquad \beta_{\rm fin} \equiv \frac{2\alpha}{\pi}\left[\frac{1+\beta^2}{2\beta}Y - 1\right]$$

and

$${\rm Li}_2(x) \equiv \int_{1-x}^{1} \frac{\ln(1-z)}{z}dz.$$

For the purpose of Monte Carlo event generation, a very small value of κ_0 (= .003, $E_{\gamma_{\rm min}}$ = .0435 GeV) is chosen to ensure that it is much smaller than the required

detected energy for a photon candidate. In the tau analysis described in Chapter 5, tau event candidates are required to have a photon of $\geq$ 0.3GeV energy as an indication of initial or final state or decay radiation. The 0.3 GeV value has the advantage of being high enough to reduce the possibility of 1) it being due to the muon candidate's energy deposition (on average, muons deposit 0.3$\pm$0.08 GeV energy in the Mark II calorimeter), 2) inaccuracy in Monte Carlo simulation of low energy photons, and 3) it being a fake photon due to spurious electronic noise.

The results of the tau analysis are not very sensitive to the minimum energy requirement of 0.3 GeV for the detected photon because of the logarithmic dependence of the cross section on κ_0 in eqn. 2.11 and eqn. 2.12. For example, if $E_{\gamma_{min}}$ were lowered to 0.2 GeV or if the energy were mismeasured by about one sigma (the energy resolution is $\delta E/E \approx .14/\sqrt{E}$ (E in GeV), 0.3 $\pm$ 0.08 GeV), the increase in cross section is only about 10%. This is more easily seen from eqn. 2.11 and eqn. 2.12, by taking the limit $\beta \rightarrow 1$ ($M_\tau/E_B \rightarrow 0$) giving

$$\begin{aligned} \sigma_{\rm ini} &\rightarrow \sigma_0 \beta_{\rm ini} \left\{ \ln\left(\frac{1}{\kappa_0}\right) + \frac{1}{2}\ln\left(\frac{4}{\mu^2}\right) - \frac{4}{3} \right\} \\ \sigma_{\rm fin} &\rightarrow \sigma_0 \left\{ \beta_{\rm fin} \left[\ln\left(\frac{1}{\kappa_0}\right) - \frac{3}{4} \right] + \frac{\alpha}{\pi}\left[\frac{5}{4} - \frac{\pi^2}{3}\right] \right\} \end{aligned} \tag{2.13}$$

with

$$\mu \equiv \frac{M_\tau}{E_B} \qquad \beta_{\rm fin} \rightarrow \frac{2\alpha}{\pi}\left[\ln\left(\frac{4}{\mu^2}\right) - 1\right].$$

A similar situation applies also to the branching ratio for the radiative tau decay $\tau^- \rightarrow \nu_\tau \mu^- \bar{\nu}_\mu \gamma$ process, described in the next chapter. The branching ratio is affected only on the order of 10% by lowering the energy cut off or by energy mismeasurement. Ten percent will be small compared to the statistical error on the measurement results presented in Chapter 5.

2.3 Tau-Pair Monte Carlo

This section further describes the Monte Carlo, KORALB, used to estimate the efficiency for detecting tau-pair events. KORALB incorporates the radiative-correction calculations from Berends *et al.*[20] (*e.g.* eqn. 2.5) to generate an event. In a later step all spin effects, the dependence of the tau decay on its polarization, are introduced by rejecting some part of the generated events according to the *ratio* of 1) the correct and much more complicated cross section[24] involving spins for tau production and decay to 2) the spinless cross section. Therefore, the Monte Carlo includes $O(\alpha^3)$ QED corrections, spin effects and finite mass of the tau. As mentioned previously, the radiative corrections can be included as a $(1 + \delta_{\rm rad})$ factor to a basic distribution like eqn. 2.3; the radiative factor distorts the $(1 + \cos^2\theta)$ distribution of $e^+e^- \rightarrow \tau^+\tau^-$ events to peak higher at small angles (see fig. 2.6). This results from very energetic initial state photon emission close to the beam where momentum conservation requires the taus to be emitted close to the beam (small angles) in the opposite direction.

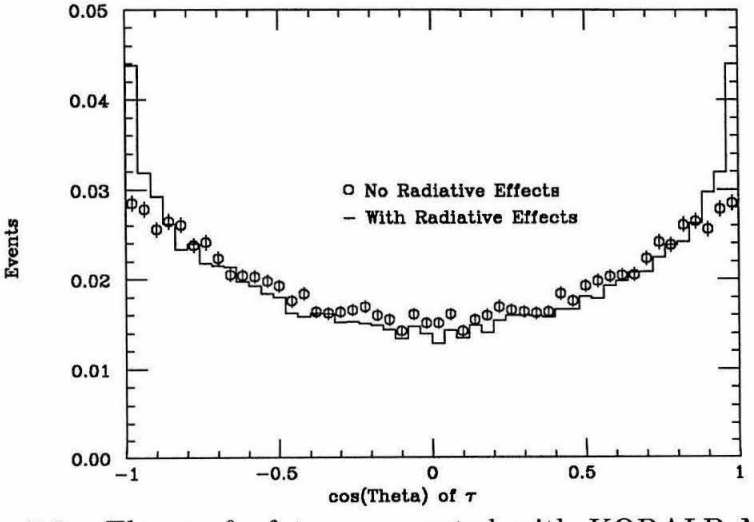

Figure 2.6. The $\cos\theta$ of taus generated with KORALB Monte Carlo, with and without radiative effects enabled.

The tau events are generated with a minimum photon energy of $k_0 = .003$ ($E_{\gamma_{\rm min}} =$

0.0435GeV), as explained earlier. For this $E_{\gamma_{min}}$, the ratio of soft : hard initial state : hard final state bremsstrahlung events is 4.88 : 6.74 : 1.0, where the soft photon is defined as having zero energy in the Monte Carlo. At this level (*i.e.*, over the entire solid angle and at fairly low energies), final state radiation is not negligible; later, the analysis results which are based only on the wide angle region will show final state radiation to be even more important and to comprise about 60% of all detected tau candidate events. As shown in fig. 2.5, the photon energy spectrum is fairly soft except for a slight peaking of initial state radiation at very high energies. Correspondingly, the tau momentum is generally very near the beam energy, except for a slight dip at very low energies (fig. 2.7) and the tau pair acollinearity rises slightly at small angles – high acollinearity – when the taus emerge close together (see fig. 2.8).

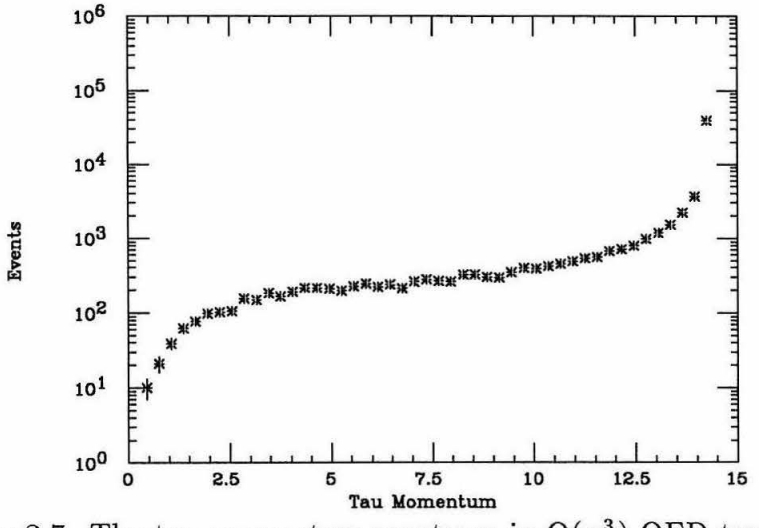

Figure 2.7. The tau momentum spectrum in $O(\alpha^3)$ QED tau-pair production.

The softness of final state radiation and its proximity to the tau is reflected in the $\tau - \gamma$ mass distribution, where the value is peaked at the tau mass without much of a tail at high energies, unlike initial state radiation with about 45% of the events being above 5 GeV (see fig. 2.9). Clearly, at $E_{cm} = 29$ GeV the tau itself is

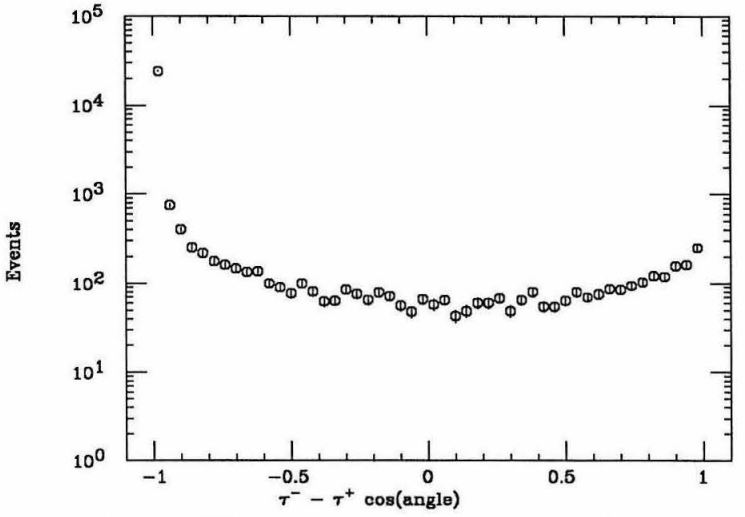

Figure 2.8. Tau acollinearity in radiative tau-pair events. Very acollinear events usually arise from very hard initial state radiation where taus emerge close together against the photon, and will not pass the event selection criteria, described in Chapter 5.

not detected, but rather its decay particles are. Figure 2.10 shows the mass of the photon from initial or final state radiation and the muon from tau decay to $\mu\nu\bar{\nu}$. The μ-γ mass spectrum shifts towards higher values when the muon momentum is above 2 GeV, a requirement used in the analysis to help identify clean muons. The requirement in event selection that reduces and affects the distribution with *initial* state photons most is that the photon be within $|\cos\theta| < .7$ (the calorimeter coverage) because initial state radiation is emitted at small angles ($|\cos\theta| \approx 1$). With the $\cos\theta$ condition, it becomes possible to distinguish regions containing mostly initial state (mass above 0.7 GeV) from final state (mass below 0.7 GeV) photon events using the mass spectrum (see fig. 2.11). The spectrum will turn out to be a very helpful variable in distinguishing radiative tau signal from backgrounds.

For a Mark II integrated luminosity of 207.9 pb^{-1}, a $e^+e^- \rightarrow \tau^+\tau^-(\gamma)$ cross section of 135 pb, and a tau branching ratio $\tau^- \rightarrow \nu_\tau\, \mu^-\, \bar{\nu}_\mu$ of 17.8%, there are approximately 10,000 $\tau^- \rightarrow \nu_\tau\, \mu^-\, \bar{\nu}_\mu$ decays produced over all solid angle. There

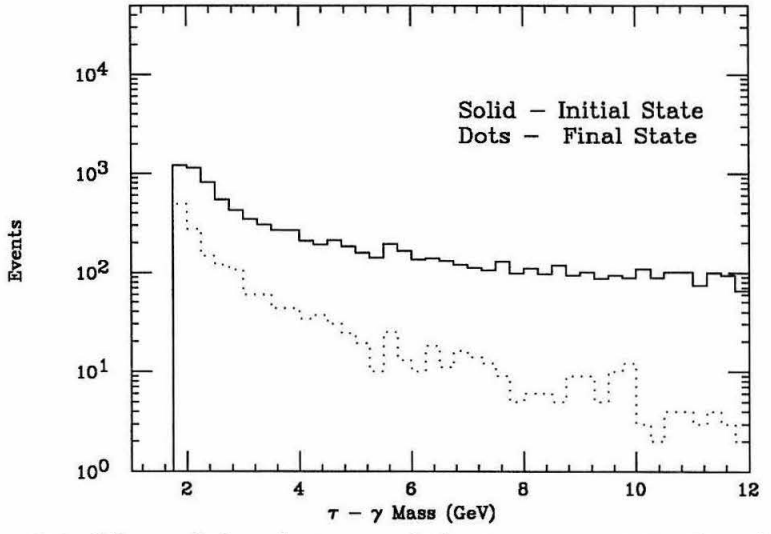

Figure 2.9. Mass of the photon and the tau nearest to the photon in $e^+e^- \rightarrow \tau^+\tau^-\gamma$ events, using particle four-vectors.

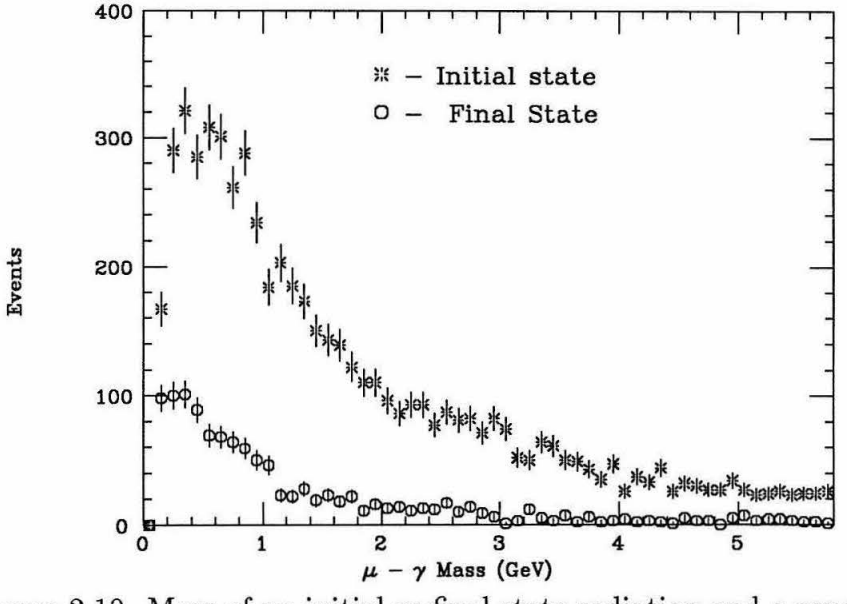

Figure 2.10. Mass of an initial or final state radiation and a muon from tau decay, where the two particles are within 90 deg of each other.

is about 20% efficiency for detecting such decays with the requirement of a muon above 2 GeV in the muon system and $\sim$ 3.5% of these events have a $>$ .3 GeV photon near the muon and in the calorimeter region. Therefore, prior to other event

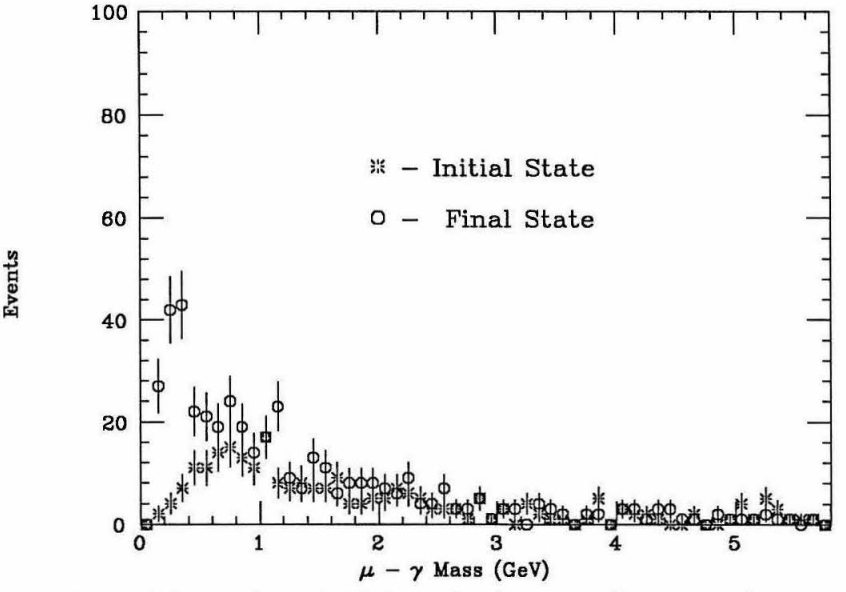

Figure 2.11. Mass of an initial or final state photon and a muon from tau decay, where the two particles are within 90° of each other. Same as previous plot but with photon $|\cos\theta| < 0.7$ and muon momentum > 2 GeV. The size of the initial state radiation contribution relative to the final state has greatly diminished, compared to the previous figure.

selection criteria, there are about 70 detectable events stemming from radiative tau production.

Chapter 3

Radiative Tau Decay

This chapter discusses the phenomenology of the decays of the tau, particularly the muon decay channel. The decay width formulas for $\tau^- \rightarrow \nu_\tau\, l^-\, \bar{\nu}_l (l = e, \mu)$ are presented along with formulas that include $O(\alpha)$ radiative corrections (*i.e.*, the process $\tau^- \rightarrow \nu_\tau\, l^-\, \bar{\nu}_l(\gamma)$). One of the main goals of this thesis analysis is to measure the branching ratio for $\tau^- \rightarrow \nu_\tau\, \mu^-\, \bar{\nu}_\mu \gamma$.[6] A Monte Carlo technique, used to simulate radiative tau decay events for the purpose of comparison with experiment, is described. Distributions of kinematic variables and expected branching ratios are presented.

3.1 Non-radiative Tau Decay

Being short-lived ($\tau_\tau = 3.04 \times 10^{-13}$ sec), the tau lepton may only be detected via its decay products at the presently available energies. The tau decays through the weak interaction to its neutrino partner and to other particles through a virtual charged W boson as shown in fig. 3.1. The decay modes are leptonic, $\nu_\tau\, e^-\, \bar{\nu}_e$ or $\nu_\tau\, \mu^-\, \bar{\nu}_\mu$, and hadronic $\nu_\tau\, (\bar{u}d)$ or $\nu_\tau\, (\bar{u}s)$, where the mass of the tau is too small to permit decays to products of heavier quarks. The partial widths for tau decays to leptons and quarks may be calculated from first principles. However, in the case of the quarks, the situation is more complex because the quarks interact strongly in the final state to form observed hadrons.[25] During the hadronization process, the quark and anti-quark pair may join to form a single hadron like the charged pion, or the pair may

fly apart and "stretch the binding color lines of force" until the increasing potential energy is sufficient to create more quarks and gluons. The newly formed clusters of quarks and gluons have lower internal momenta and therefore stronger color coupling which binds them to form several hadrons. The exact transformation of the quarks and gluons into hadrons is still an unsolved, non-perturbative problem. Therefore, to calculate the numerical value of hadronic tau decay widths, other schemes must be employed. Conservation principles, inversion methods, etc., are often used to relate hadronic tau decay widths to other measured processes.[3] For example, $\tau^- \rightarrow \nu_\tau \pi^-$ can be related to the inverse process of a charged pion decaying to a muon, $\pi^- \rightarrow \mu^- \bar{\nu}_\mu$.

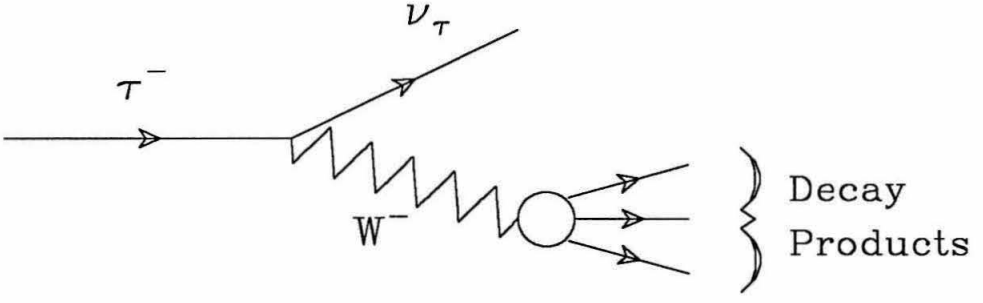

Figure 3.1. Diagram of tau decay to the tau-neutrino and to the virtual W boson, which then materializes as leptons or quarks.

3.2 Total Leptonic Tau Decay Width

For this thesis, the main interest is the leptonic tau decay modes, which will be described in the remainder of this chapter. A diagram of the decay $\tau^- \rightarrow \nu_\tau \mu^- \bar{\nu}_\mu$ via the weak interaction is given in fig. 3.2. The W^- boson mediating the decay is believed to couple to the (τ, ν_τ) and to the $(\mu, \bar{\nu}_\mu)$ with the same coupling strength and through the same (V−A) interactions. The (V−A) interaction gives rise to a particular spectrum for the decay particles and a measurement of these are embodied in the so-called Michel parameters. The only parameter determined thus far for tau

decay is the momentum shape parameter ρ. The (V−A) coupling yields a value of $\rho = .75$, while the measured values of the parameter for tau decay ($.73 \pm .07$) and for muon decay ($.7518 \pm .0026$) agree with each other and with the predicted value. This result is consistent (within 10%) with universal $e - \mu - \tau$ weak coupling, which allows the application of the calculations for $\mu^- \rightarrow \nu_\mu \, e^- \, \bar{\nu}_e$ to $\tau^- \rightarrow \nu_\tau \, l^- \, \bar{\nu}_l$ $(l = e, \mu)$, and $\mu^- \rightarrow \nu_\mu \, e^- \, \bar{\nu}_e \gamma$ to $\tau^- \rightarrow \nu_\tau \, l^- \, \bar{\nu}_l \gamma$.

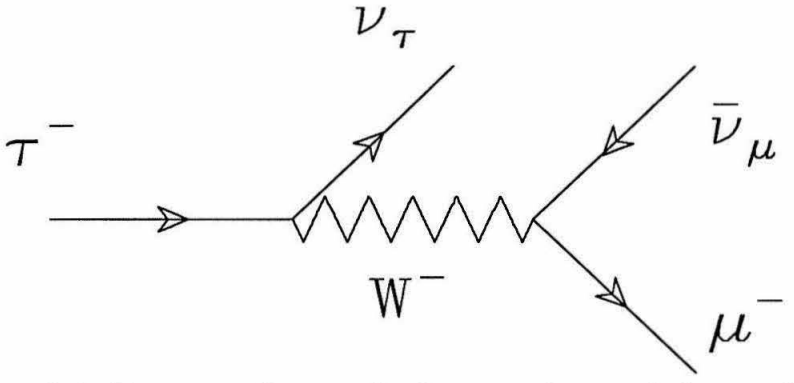

Figure 3.2. Feynman diagram for lowest order weak decay of tau lepton to the muon mode.

Various textbooks[19] provide a calculation for the pure leptonic decay probability for muons. By substituting the tau mass (m_τ) for the muon mass, the total decay rate for $\tau^- \rightarrow \nu_\tau \, l^- \, \bar{\nu}_l$ $(l = e, \mu)$ is

$$\Gamma(\tau^- \rightarrow \nu_\tau \, \mu^- \, \bar{\nu}_\mu) \quad = \quad \frac{G_F^2 \, m_\tau^5}{192\pi^3} \tag{3.1}$$

where G_F is the Fermi coupling constant.

The decay rate given by eqn. 3.1 does not include the effects of the finite mass of the final-state charged lepton (muon in this case), or of the electroweak radiative

processes. Including these effects gives the following corrected total decay rate:[12]

$$\begin{aligned}\Gamma(\tau^- \to \nu_\tau \mu^- \bar{\nu}_\mu(\gamma)) &= \frac{G_F^2 m_\tau^5}{192\pi^3} F\left(\frac{m_\mu^2}{m_\tau^2}\right)\left[1 + \frac{3}{5}\frac{m_\tau^2}{m_W^2}\right]\left[1 + \frac{\alpha(m_\tau)}{2\pi}\left(\frac{25}{4} - \pi^2\right)\right] \\ \Gamma(\tau^- \to \nu_\tau \mu^- \bar{\nu}_\mu(\gamma)) &= (4.003 \pm 0.036) \times 10^{-13}\,\text{GeV}\end{aligned} \tag{3.2}$$

for

$$\alpha(m_\tau) \approx \frac{1}{133.3}$$

and where

$$F(y) \quad = \quad \left(1 - 8y + 8y^3 - y^4 - 12y^2 \ln y\right)$$

is a factor to account for the mass of the final state charged lepton. For muonic tau decay, this factor has a value of ~ 0.973, and for electronic tau decay it is ~ 1.0. This mass factor causes the only difference between the electron and muon tau decay branching ratios. The $\alpha(m_\tau)$ parameter is the effective electromagnetic coupling, the value of which depends on the masses of the tau and the fermions lighter than the tau and the fine structure constant $\alpha = 1/137.036$; renormalizing α allows absorption of various radiative corrections.[12]

In eqn. 3.2, the factor

$$\left[1 + \frac{3}{5}\frac{m_\tau^2}{m_W^2}\right]$$

is due to the presence of the virtual W vector boson in tau decay. The finite mass of the W (M $\sim$ 81 GeV) makes the interaction non-local rather than a point four-fermion theory[26] which was originally used to explain muon decay (see fig. 3.3). The value of the factor is 1.0003, barely changing the value of the width.

Finally, in eqn. 3.2, the factor

$$\left[1 + \frac{\alpha(m_\tau)}{2\pi}\left(\frac{25}{4} - \pi^2\right)\right] \tag{3.3}$$

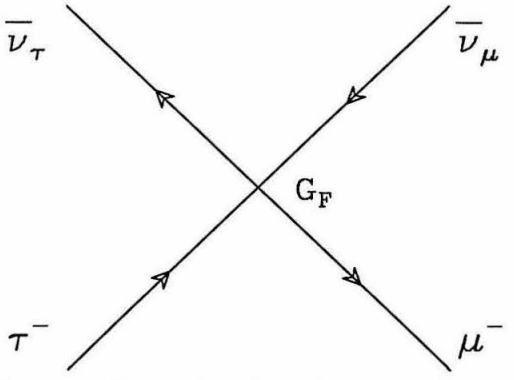

Figure 3.3. Diagram for point four-fermion theory of tau decay where the strength of the interaction is related to the Fermi coupling constant.

has a value of 0.9957 and is a first order QED correction to the decay width and includes virtual corrections as well as soft and hard photon emission.* Examples of virtual corrections to the process $\tau^- \rightarrow \nu_\tau \mu^- \bar{\nu}_\mu$ are shown in fig. 3.4. The analysis reported in this thesis is concerned with the $\tau^- \rightarrow \nu_\tau \mu^- \bar{\nu}_\mu \gamma$ decay process where a *real* photon is emitted, also known as inner bremsstrahlung, shown in fig. 3.5. Bremsstrahlung from the muon contributes more than from the tau in fig. 3.5 because the muon is less massive. The QED correction factor, eqn. 3.3, may be expressed as a factor containing two corrections (1 + virtual correction + bremsstrahlung correction). It was shown by S. Berman for radiative muon decay, in a calculation also applicable to leptonic radiative tau decay, that for the low region of the muon energy spectrum in radiative tau decay, the magnitude of the bremsstrahlung correction is larger than that of the virtual corrections, and that the opposite is true for the high energy region.[27] For the integral over all muon energy, the virtual piece dominates and since it is negative, the *total* QED correction factor is slightly less than one.

If measurements of the branching ratio, $B(\tau^- \rightarrow \nu_\tau \mu^- \bar{\nu}_\mu)$, do not include the contribution from inner bremmstrahlung (real photon emitted), then the measured

* A parenthesis around the γ, such as in $\tau^- \rightarrow \nu_\tau \mu^- \bar{\nu}_\mu(\gamma)$, is used to indicate that the photon may or may not be detected.

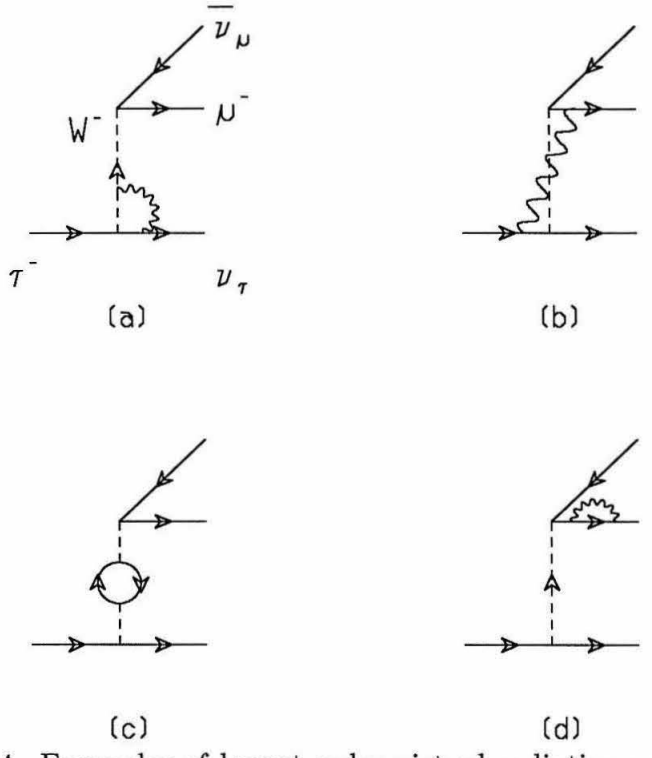

Figure 3.4. Examples of lowest-order virtual radiative corrections to muonic tau decay: (a) vertex corrections, (b) box diagram, (c) vacuum polarization, and (d) self-mass.

value obtained is slightly less than actual. However, the loss is small and is expected to occur at the percent level of the total branching ratio for $\tau^- \rightarrow \nu_\tau \, \mu^- \, \bar{\nu}_\mu$ and, thus, is within the measurement error of the current world-average value for the branching ratio $\mathrm{B}(\tau^- \rightarrow \nu_\tau \, \mu^- \, \bar{\nu}_\mu)$ of $(17.8 \pm 0.4)\%$.[13]

The branching ratio, $\mathrm{B}(\tau^- \rightarrow \nu_\tau \, \mu^- \, \bar{\nu}_\mu)$, and the total decay width are related by

$$B(\tau^- \rightarrow \nu_\tau \, \mu^- \, \bar{\nu}_\mu) \quad = \quad \tau_\tau \; \times \; \Gamma(\tau^- \rightarrow \nu_\tau \, \mu^- \, \bar{\nu}_\mu).$$

For an uncorrected decay width (eqn. 3.1) value of 1.595×10^{-12} sec^{-1} and a measured tau lifetime of $(3.04 \pm .09) \times 10^{-13}$ sec, the branching ratio is $(19.1 \pm .6)\%$. Table 3.1 shows how the muon mass and, to a lesser extent, the electroweak radiative corrections alter the branching ratio value of $(19.1 \pm .6)\%$ to give a final value of $(18.5 \pm .5)\%$ for

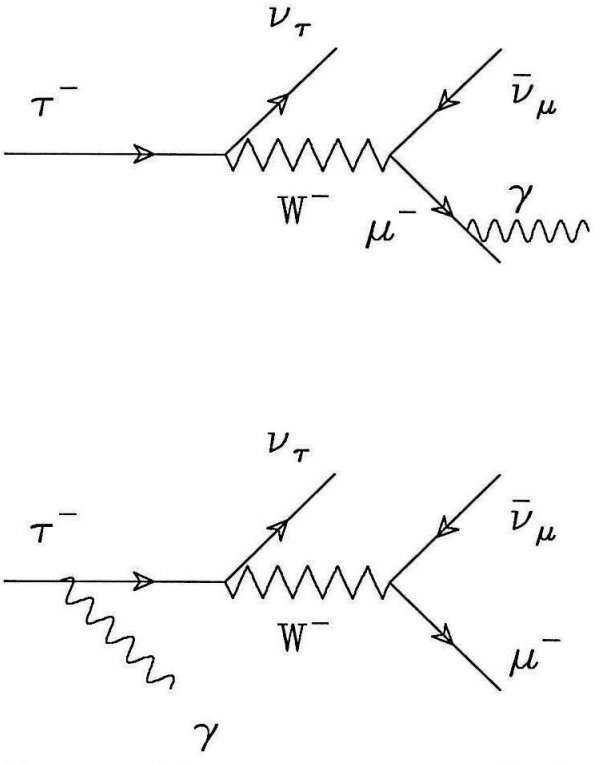

Figure 3.5. Diagrams of tau decay accompanied by the emission of real photons.

$B(\tau^- \to \nu_\tau \mu^- \bar{\nu}_\mu(\gamma))$. This final "calculated" value, which has an error due mainly to the error on the tau lifetime measurement, agrees to within ~ 1.1 standard deviations of the world average measured branching ratio value of $(17.8 \pm 0.4)\%$.

Table 3.1. Magnitude of corrections to the branching ratio $B(\tau^- \to \nu_\tau \mu^- \bar{\nu}_\mu)$ from the inclusion of muon mass and electroweak radiative corrections.

Correction to Γ_0	Magnitude	$B(\tau^- \to \nu_\tau \mu^- \bar{\nu}_\mu)$
uncorrected value	–	19.06%
muon mass	0.9728	18.54%
W propagator	1.0003	18.55%
$O(\alpha)$ QED correction	0.9957	18.46%

The full muonic tau decay width (eqn. 3.2) has a value of $(4.003 \pm 0.036) \times 10^{-13}$ GeV, where the 0.9% error comes from the uncertainty in the measurement of the tau mass. This value will be used to normalize the results of the differential decay width for inner bremsstrahlung, considered in the next section.

3.3 Differential Decay Width For Inner Bremsstrahlung

In order to understand the process of tau decay with the emission of a real photon, $\tau^- \rightarrow \nu_\tau \, \mu^- \, \bar{\nu}_\mu \, \gamma$, as it occurs in a complicated detector, Monte Carlo simulations are often used. The event characteristics, the fine-tuning of selection criteria, and the detection efficiency for individual events may be studied by this method. Processes are simulated by producing sets of particle four-vectors distributed according to a theoretical transition probability. The four-vectors are passed through simulations of the detector response with complicated acceptance and measurement resolution. An expression for the theoretical transition probability, necessary to a Monte Carlo program, must contain the detectable quantities, the four-vectors of the τ, μ, and γ in the process $\tau^- \rightarrow \nu_\tau \, \mu^- \, \bar{\nu}_\mu \, \gamma$. Such expressions can be found in the literature concerning muon decays.

In the 1950's, the understanding of muon decay and the precision of the decay rate measurements made necessary the inclusion of radiative corrections. R.E. Behrends, R.J. Finkelstein and A. Sirlin[28,29,27] have provided differential decay width calculations for muon decay with inner bremsstrahlung, $\mu^- \rightarrow \nu_\mu \, e^- \, \bar{\nu}_e \gamma$, where the mass of the muon and the electron are taken into account. The calculation is based on (V−A) couplings with a point four-fermion interaction, but is still applicable to the current understanding of tau decays* (*e.g.*, the effect of the W propagator is small, as mentioned in the previous section).

Denoting the parent charged lepton as particle 1 and the final-state charged

* A. Sirlin. Private communication.

lepton as 2, then the differential transition probability is[28]

$$d\Gamma = G_F^2(N_v + N_a)\frac{\alpha d^3p\, d^3\kappa}{6(2\pi)^6 E_1 E_2 \epsilon} \tag{3.4}$$

where

$$N_v = \left\{G^2\left[\frac{1}{2}(m_1 - m_2)^2 - 2m_1m_2 - G^2\right] + \frac{1}{2}(m_1^2 - m_2^2)^2\right\}\Omega$$

$$+ 4G^2 + \frac{(\kappa\cdot G)^2\,[2G^2 + (m_1 - m_2)^2]}{(p_1\cdot\kappa)\,(p_2\cdot\kappa)}$$

and

$$N_a = \left\{G^2\left[\frac{1}{2}(m_1 + m_2)^2 + 2m_1m_2 - G^2\right] + \frac{1}{2}(m_1^2 - m_2^2)^2\right\}\Omega$$

$$+ 4G^2 + \frac{(\kappa\cdot G)^2\,[2G^2 + (m_1 + m_2)^2]}{(p_1\cdot\kappa)\,(p_2\cdot\kappa)}.$$

The variables p_1, p_2, and κ are the four-momenta of leptons 1, 2, and the photon, respectively, and E_1, E_2, and ϵ are their energies. In the lab frame of particle 1, d^3p is d^3p_2. G_F and α are the Fermi coupling constant and the fine structure constant, respectively. G, the four-momentum of the two neutrinos taken together, and Ω are defined by

$$G = p_1 - p_2 - \kappa$$

and

$$\Omega = \sum_{i=1,2}\left[\frac{p_2\cdot e_i}{p_2\cdot\kappa} - \frac{p_1\cdot e_i}{p_1\cdot\kappa}\right]^2,$$

where the sum is over photon polarization vectors e_i.

3.4 Monte Carlo Simulation of Radiative Tau Decay

Radiative tau decay events are simulated by generating particle four-vectors distributed according to eqn. 3.4. The details of the procedure used to generate unweighted $\tau^- \to \nu_\tau \mu^- \bar{\nu}_\mu \gamma$ events are as follows:

I) In the tau rest frame, the muon energy, the photon energy, and the angle between the muon and photon are generated randomly but within the kinematic limits allowed for a four-body decay. Because neutrinos are not detected, their momenta have been integrated over and do not appear in eqn. 3.4.

II) The event weight is calculated from the integrand of eqn. 3.4 for the generated configuration and compared against the maximum value the weight can take on. If the ratio of the weight to its maximum value is greater than a random number generated uniformly between zero and one, the event is retained. (Specifically, applying the weighting rejection technique (WRT) means the following. In general, the distribution $f(x)$ of some kinematic variable x is very complicated. Another distribution function $g(x)$ is chosen to approximate $f(x)$ so that it is simple in form and as close as possible to $f(x)$ to ensure high event-generation efficiency. In the first step, the energies and angle are generated according to the simpler distributions: $g(x)$. WRT is then applied by keeping the generated event if

$$\frac{R}{R_{max}} \geq \text{random value between}[0,1]$$

where

$$R = \frac{f(p_1,\ p_2,\ \cos\theta_{1,2})}{g(p_1,\ p_2,\ \cos\theta_{1,2})}.$$

Otherwise, the program returns to step (I)).

III) Once an event has been accepted, the four-vectors generated in the tau rest frame are rotated to a random orientation. (This neglects tau polarization and spin-spin correlations, explained below.)

IV) The events which are kept are now incorporated as another decay mode of the main tau-pair Monte Carlo, KORALB[17], described in chapter 2. The generated

muon and photon are boosted along the tau direction into the lab frame.

Because the tau decays weakly, the angular distribution of its decay products in the tau rest frame is not isotropic with respect to its spin axis. Therefore, if the polarization (average helicity) of the tau is non-zero, then in the lab frame, the distribution of energy-angles of the decay products are different from what they would be if the decays were isotropic in the tau rest frame. Tau polarization is negligible at $E_{cm} = 29$ GeV, however[30]; so, this non-isotropy effect is negligible.

KORALB takes into account another effect, the spin correlations between the two taus produced (at high energies, the taus emerge with opposite helicity due to helicity conservation). Correlation between the taus' spins causes a correlation between the energies of the decay products of the τ^+ and τ^-. This spin–spin correlation effect is neglible for this analysis because 1) spin effects are not large in multi-body decays, and 2) the event selection criteria used in this analysis are insensitive to correlations in decay product energies. Therefore, for the $\nu_\tau\, \mu^-\, \bar{\nu}_\mu \gamma$ decay channel, spin correlation effects are not incorporated in the Monte Carlo.

When $\nu_\tau\, \mu^-\, \bar{\nu}_\mu \gamma$ is incorporated in KORALB as another decay mode, an assumption is made that there is negligible inteference between photons from tau decay and any photons from tau production. Decaying weakly, the tau has a lifetime on the order of 10^{-13} seconds, which is $> 10^3$ times longer than the typical time scales of electromagnetic interactions. Therefore, to a good approximation, radiative tau decay is independent of (radiative) tau production.

Cross checks were performed to ensure the accuracy of the radiative tau decay events generated, including using the Monte Carlo event generator, described in (I–IV), to perform an integration of the differential decay width (eqn. 3.4) for the radiative muon decay, which consists of summing R, now weighted by the integration (kinematic) limits, for all events in step (II). The program reproduces the numerical

results for $\mu^- \rightarrow \nu_\mu e^- \bar{\nu}_e \gamma$ given in ref. 31.

3.5 Numerical Results for Radiative Tau Decay Process

The value of the decay width for only the hard bremsstrahlung part of radiative tau decay, $\tau^- \rightarrow \nu_\tau \mu^- \bar{\nu}_\mu \gamma$, depends on the choice of limits of integration in eqn. 3.4. In the Monte Carlo, the muon and photon energies are permitted to range over all kinematically allowed values; however, a minimum energy $E_{\gamma min}$ cutoff is chosen for the photon. Its necessity can be seen from eqn. 3.4 where the last term diverges when the photon 4-momentum κ approaches zero. An analytic expression may be obtained by integrating eqn. 3.4 to give the width for tau decay accompanied by a photon of energy greater than some value κ_0.[31] The expression contains a term $\frac{1}{\kappa}$ which diverges in the soft photon limit, $\kappa \rightarrow 0$. As shown in chapter 2, this soft photon limit divergence also occurs in the $O(\alpha^3)$ calculation for the production cross section of tau pairs. The procedure is to integrate the expression for bremsstrahlung only above some photon energy cutoff value, where the value chosen depends on the photon energy detection threshold of the experimental apparatus. For this analysis, a value of 0.0123 GeV, given in the tau rest frame, is used for the minimum photon energy $E_{\gamma min}$. This corresponds to lab energy values often much less than .2 GeV, after the photon is boosted into the lab frame at $E_{cm} = 29$ GeV. The event selection (chapter 5) uses only photons above .3 GeV; therefore, the $E_{\gamma min}$ value used is a conservative choice.

To quantify the significance of radiative tau decay, it is reasonable to normalize the decay width for radiative events $\tau^- \rightarrow \nu_\tau \mu^- \bar{\nu}_\mu \gamma$ to the total decay width for $\tau^- \rightarrow \nu_\tau \mu^- \bar{\nu}_\mu(\gamma)$. The value of the total width is taken to be 4.003×10^{-13} from eqn. 3.2 which includes muon mass and first order electroweak corrections. The bremsstrahlung width is only $\sim 2\%$ of the total width for a .0123 GeV $E_{\gamma min}$ value. With a photon lab-energy requirement of .3 GeV, not all of the photons above .0123

GeV (tau rest frame) will be above .3 GeV (lab frame); therefore, the bremsstrahlung width with the lab frame cutoff is actually smaller, about 1.1% of the total width.

All of the calculations and Monte Carlo apparatus described for $\tau^- \to \nu_\tau \mu^- \bar{\nu}_\mu \gamma$ may also be used to understand $\tau^- \to \nu_\tau e^- \bar{\nu}_e \gamma$. However, there are several reasons for choosing to analyze and measure the branching ratio for $\tau^- \to \nu_\tau \mu^- \bar{\nu}_\mu \gamma$ and not that for $\tau^- \to \nu_\tau e^- \bar{\nu}_e \gamma$. Because electron tracks lose energy in material through bremsstrahlung and leave wide showers in the calorimeter, it is more difficult to resolve the shower of the photon separately from that of the electron track and thereby extract a $\tau^- \to \nu_\tau e^- \bar{\nu}_e \gamma$ signal. Another disadvantage of an electronic radiative tau measurement is the larger QED background to $\tau^- \to \nu_\tau e^- \bar{\nu}_e \gamma$ than to $\tau^- \to \nu_\tau \mu^- \bar{\nu}_\mu \gamma$ (*e.g.*, background from radiative Bhabha events is larger than from radiative mu-pair because of the additional t-channel diagram for Bhabha scattering).

The expected number of events in the data sample analyzed for this thesis will now be estimated. The Mark II data represent a total integrated luminosty of 207.9 pb^{-1}, and for a total tau-pair production cross section $e^+e^- \to \tau^+\tau^-(\gamma)$ of 135 pb and total muonic tau branching ratio of 17.8%, one expects approximately 108 $\tau^- \to \nu_\tau \mu^- \bar{\nu}_\mu \gamma$ decays produced. However, not all of these events are detectable. Because of limited detector solid angle and muon identification inefficiencies, the probability of detecting the muon in radiative tau decay is only $\sim$ 21%. There is also an inefficiency due to the inability to separately reconstruct the photon when it is emitted very near the muon, reducing the previous figure of 21% by about 60% to give $\sim$ 13.5%. Therefore, prior to applying further event selection criteria, the expected number of $\tau^- \to \nu_\tau \mu^- \bar{\nu}_\mu \gamma$ decays is about 14–15 events. Since this is very few events, it is crucial to have very high efficiency at the event selection stage in order to "yank" out any signal at all. It is also important to find kinematic variables, discussed in the next section, which would naturally enhance the $\nu_\tau \mu^- \bar{\nu}_\mu \gamma$ signal.

3.6 Kinematics of Radiative Tau Decay Process

This section considers some features of events from radiative tau decays to the muons. The energy spectrum of the emitted photon, shown in fig. 3.6. is very soft even after being boosted from the tau rest to the lab frame at $E_{cm} = 29$ GeV. Only photons with energy above .3 GeV are accepted in the event selection, and we see from fig. 3.6 that only 55% of the Monte Carlo events generated with $E_{\gamma min} = .0123$ GeV pass the photon selection criterion. Therefore, even in the presence of a low-energy photon there is little change in the muon momentum spectrum as shown in fig. 3.7. After the muon and photon are boosted by the tau energy, the angle between them is generally small, as depicted in fig. 3.8. When the angle becomes smaller than $\sim$ 1.8°, the calorimeter cluster algorithm tends to associate the photon with the muon. The critical angle of 1.8° is found from studying muon tracks with nearby neutrals, using the data from all processes. One might hope to find radiative tau decays by looking for muon tracks with large associated calorimeter energy because muons are minimum-ionizing particles and normally do not deposit shower energies characteristic of photons. Using cosmic ray events to study the calorimeter response of muons, one finds that Landau fluctuations for muons give shower-like energy depositions which prove to be a large enough background to make this method unfeasible. For cosmic ray muon tracks selected with a momentum range similar to that of muons from $\tau^- \rightarrow \nu_\tau \mu^- \bar{\nu}_\mu$, the probability of finding an additional $\geq .3$ GeV energy deposition in the calorimeter is measured to be $\sim 1.7\%$. With event cuts, the expected number of events from non-radiative tau events, $\tau^- \rightarrow \nu_\tau \mu^- \bar{\nu}_\mu$, is ~ 1000 events, giving $\sim$ 17 events where the muon energy deposition fluctuates high. However, the expected number of $\tau^- \rightarrow \nu_\tau \mu^- \bar{\nu}_\mu \gamma$ events, with sufficiently high photon and muon energy deposition overlap is only ~ 5, which is within one sigma of the statistical error on the expected number (> 21) of total events.

The reconstructed μ-γ mass is a useful variable for distinguishing radiative tau

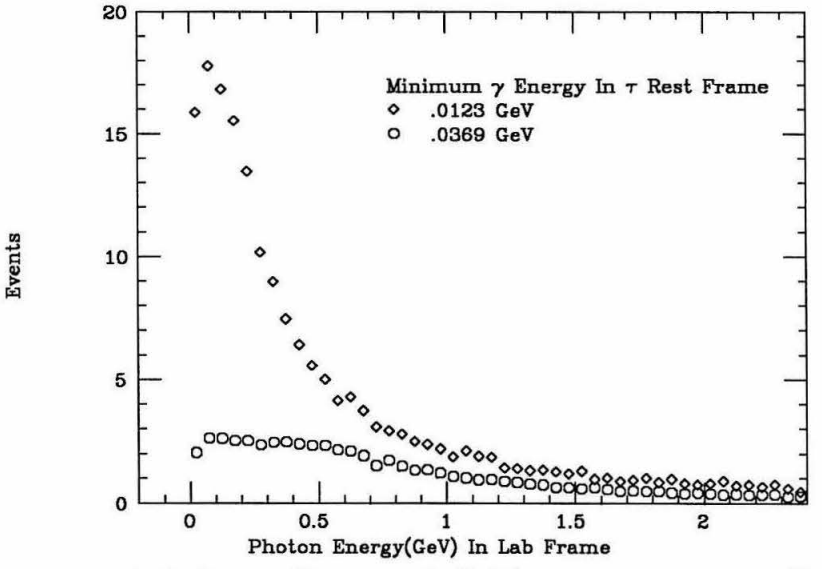

Figure 3.6. Lab frame (E_{cm} = 29 GeV) energy spectrum (four-vector level) of photons emitted in radiative tau decay to the muon channel for two different minimum photon energy values in the tau rest frame. The normalization is based on the Mark II luminosity.

decay events from other processes such as radiative tau production considered in chapter 2. Figure 3.9 shows the μ-γ mass from radiative decay and from radiative production, where photons from the latter process may be from the initial state or from the final state in $e^+e^- \rightarrow \tau^+\tau^-\gamma$. One sees clear separation between the two processes. In order to identify muons and photons, an energy requirement of 2 GeV is placed on the muon, and .3 GeV on the photon. This shifts both mass spectrums shown in fig. 3.9 towards higher average values, but radiative decay still yield μ-γ mass values mostly below .3 GeV and radiative production mostly above. In chapter 5, we'll see that using the mass variable will provide good enough separation between radiative tau decay and backgrounds to extract the radiative decay signal. In summary, the procedure to measure the branching ratio $B(\tau^- \rightarrow \nu_\tau \mu^- \bar{\nu}_\mu \gamma)$ is to make event cuts to select the muon channel of tau decays and to require the presence of a photon. Then the μ-γ spectrum is used to distinguish radiative decay from radiative production and other backgrounds.

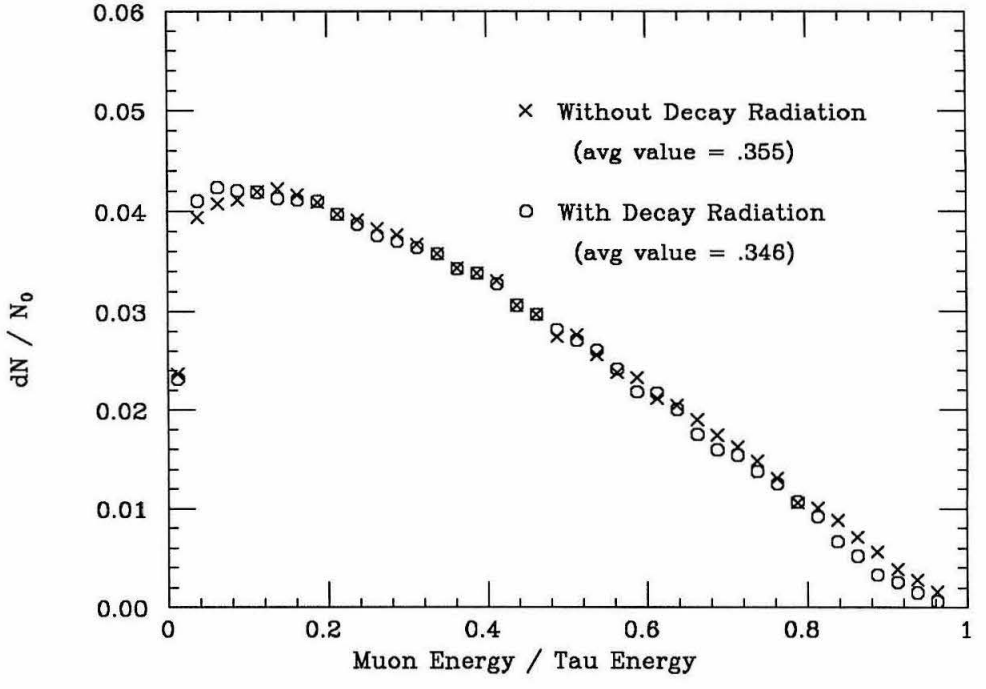

Figure 3.7. Comparison of the muon energy spectrum in radiative and non-radiative tau decay events. The two cases are very similar because radiative decay photons have very low energy.

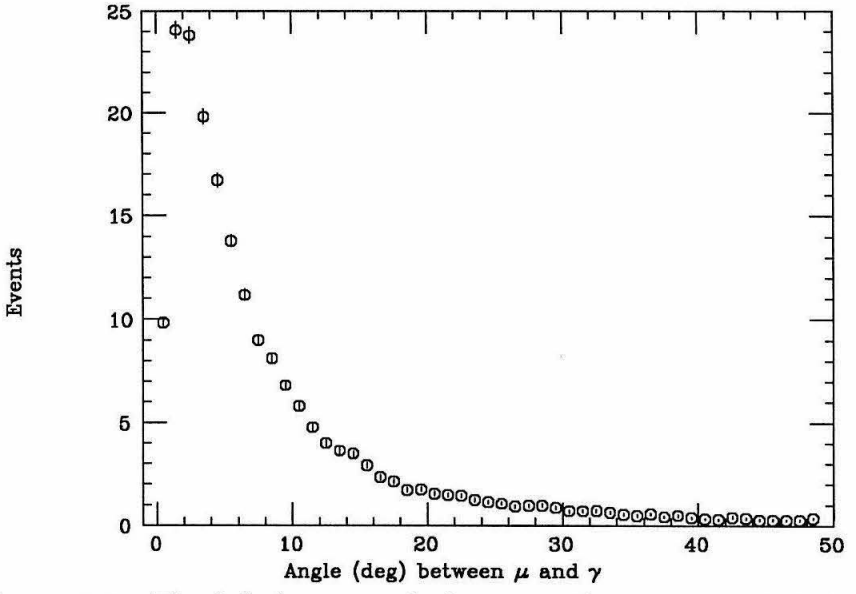

Figure 3.8. The lab frame angle between the muon and photon in radiative tau decay, where the angle is calculated using particle four-vectors.

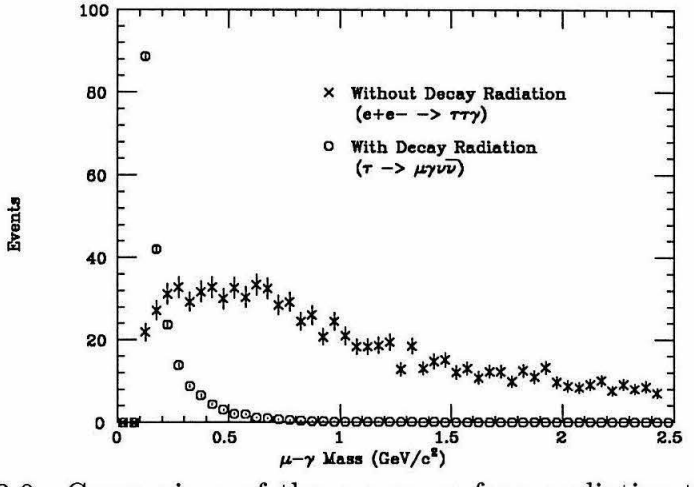

Figure 3.9. Comparison of the μ-γ mass from radiative tau production and radiative tau decay, where the mass is computed from particle four-vectors. The plot contains only events where the photon is within 90 degrees of the muon. The normalization is based on the Mark II integrated luminosity and no event selection criteria have been applied.

Chapter 4

The Mark II Detector

The data used for this thesis analysis was collected by the Mark II detector at PEP (Positron Electron Project) at $E_{cm} = 29$ GeV during the 1981-1984 period. A description of the detector and its performance is provided in this chapter. Much of the detector parameters and work described here is written up in hundreds of internal memos, pre-prints and theses, provided by scores of present and former Mark II and SLAC members.

PEP is a storage ring where electron and positron beams of about 20 mA each with cross section size of 480μm x 65μm collided every 2.4 μs, parameters which provided, during the data taking period, a total integrated luminosity of about 210 pb^{-1}.[32] In practice, the most accurate way of measuring the luminosity is by using Bhabha scattering, a process for which the cross section is well known and is large enough to yield very high statistics. In ref. 33, wide angle Bhabhas were selected by *two* separate methods, each providing an efficiency cross-check on the other. Correction for detection acceptance yielded a total integrated luminosity of $207.9 \pm 0.5 \pm 2.8$ pb^{-1} for the data tapes used. The PEP "beams" are actually short bunches ($\sim$ 1.5 cm long) of electrons (positrons) which travel in an almost-circular orbit guided by magnetic fields and lose about 0.2% of the beam energy through synchrotron radiation after one revolution. Radio frequency cavities provide oscillating electric fields which accelerate the particles back to the desired beam energy, providing a stable

orbit. There is negligible energy spread (~0.1% of beam energy) among the ($\sim 10^{11}$) particles in each bunch at a storage ring; it's sufficient to use a center-of-mass energy of exactly 29 GeV for all of the data events processed. The variation of the positions of the beams at the interaction point (*e.g.*, from orbit variation, from transverse and longitudinal oscillations of the beam particles with respect to their average direction of motion) is small. Placed 4.9 m on either side of the interaction were beam position monitors, each with four electrodes, that extended into the beam pipe. These were read out every four minutes, the voltages on the electrodes induced by the passing of the beam, giving a measure of the beam position. Within a run, the position drifted by only $\sim 20 - 50\mu$m; this drift and the bunch length are much smaller than the required distance of closest approach to the interaction point for a track to be deemed "good" in the tau analysis (Chapter 5). Over many runs, the interaction point is calculated from the averaged intersection point of event tracks. Therefore, as far as the analysis in this thesis is concerned, the beams were very well behaved, constant in energy and position.

4.1 Introduction to the Mark II Detector

The Mark II detector in 1981-84 is shown in fig. 4.1. It is a system of subdetectors concentric with the beam that determine the momentum, position and identity of the particles emerging from an e^+e^- interaction. In a radially outward direction, a particle would encounter the elements in the order listed in Table 4.1. All of the detector components are used in the tau analysis, including the small-angle tagger and endcap calorimeter, but the two drift chambers, the barrel calorimeter and muon system are the most important. The outermost layer of the two drift chambers covers $|\cos\theta| < .67$ and the barrel calorimeter covers $|\cos\theta| < .69$, where θ is the polar angle. Covering about 45% of the solid angle, the outer layer of the muon system essentially determines the acceptance of the $\tau^- \rightarrow \nu_\tau \mu^- \bar{\nu}_\mu$ events. In the

following sections, the z coordinate is defined to be parallel to the beam and (x,y) coordinates transverse to the beam.

4.2 Momentum Measurement

The momentum of charged particles is computed from the information provided by both drift chambers, the inner Vertex Chamber and the outer Drift Chamber.

The vertex chamber consists of two bands of wires strung parallel (z-coordinate) to the beam, providing high precision position information for a particle only in the x-y plane. The rms error on the position of a track extrapolated to the interaction point is $\sigma^2 \approx (95\mu\text{m})^2 + (95\mu\text{m}/p)^2$, where p is the transverse momentum of the track and the second term comes from multiple scattering in the beam pipe.[34] There are four (sense + field) wire layers in the inner band and three in the outer band, placed in a configuration as shown in fig. 4.2. The outermost layer of this chamber covers $|\cos\theta| < .88$, and is at a radius of 35 cm.

Energetic charged particles traversing the chambers ionize the ethane-argon gas molecules in these chambers and the ionized electrons drift towards the sense wires, held at a positive potential with respect to the field wires. In addition to the electric field which is approximately transverse to the z-axis, the chambers are inside a magnetic field, uniform to a few percent, running parallel to the z-axis. Therefore, charged particles travel in helical orbits in the chambers, and the radius of curvature of the orbit is proportional to the particle's momentum transverse to the beam. The tracking resolution depend on the number of measurements (sense wire hits) and the radial distance over which the hits are distributed; therefore, in addition to the vertex chamber, there is the main drift chamber to extend the radial coverage.

The main drift chamber has 16 layers (radius: 41-145 cm) of rings of wire *cells*, concentric with the beam pipe; a sense wire is in the middle of each cell with three field wires on each side (see fig. 4.3). Six of the layers have sense wires parallel to the

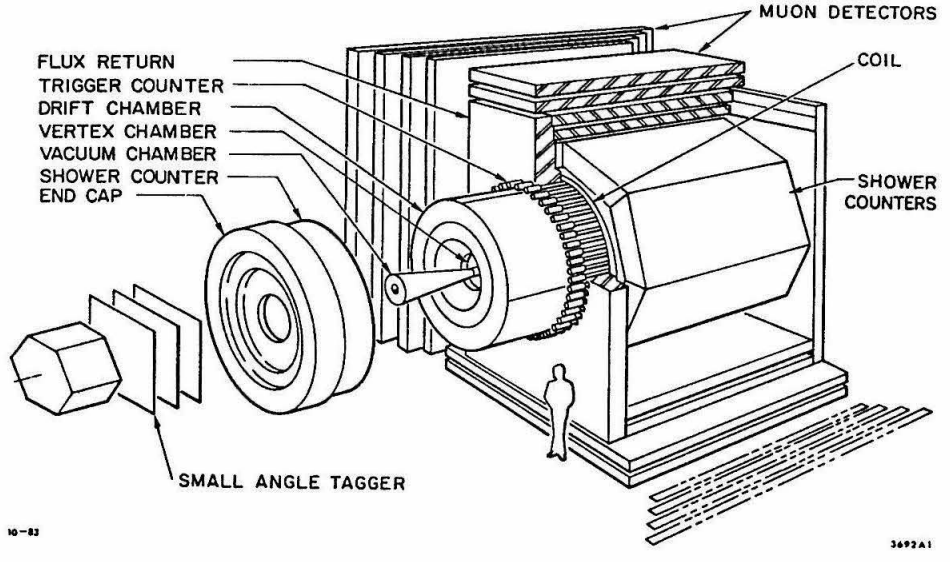

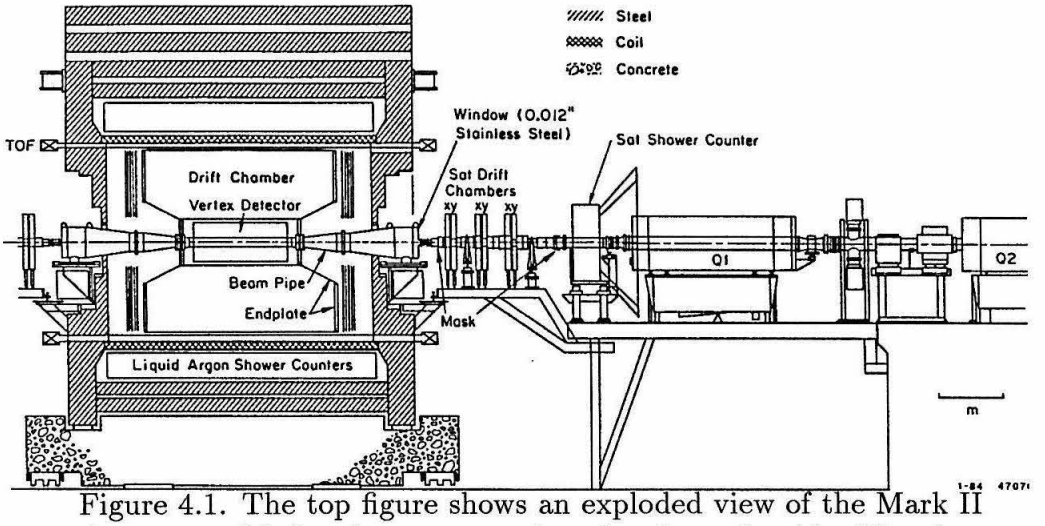

Figure 4.1. The top figure shows an exploded view of the Mark II detector and below is a cross section view from the side. The electrons enter the detector from the right through the beampipe and the quadrupole magnets, Q1 and Q2. Similarly, the positrons enter from the left and collide with electrons at the center of the vertex chamber. In the following sections, the z coordinate is parallel to the beam and (x-y) are coordinates are transverse to the beam.

beam axis; the other ten layers have sense wires pitched at an angle of ± 3 degrees in

Table 4.1. The Mark II detector components traversed by particles at 90° incidence - see ref. 34 and ref. 32.

Element	Material	Mean Radius (cm)	Radiation length
Beam pipe	Be	7.7	0.006
Vertex Chamber	Al, Ar-ethane	7.8-35.0	0.028
Drift Chamber	lexan	37.3	0.037
	Ar-ethane	37.4-150.3	0.046
	Al	150.7	0.117
TOF Counter	Pilot F	152	0.181
Magnet Coil	Al	159. - 173.	1.48
Calorimeter	Pb-Ar	180. - 221.	15.5
Muon System	Fe, side	320. - 450.	75.5
Muon System	Fe, top/bottom	250. - 360.	75.5

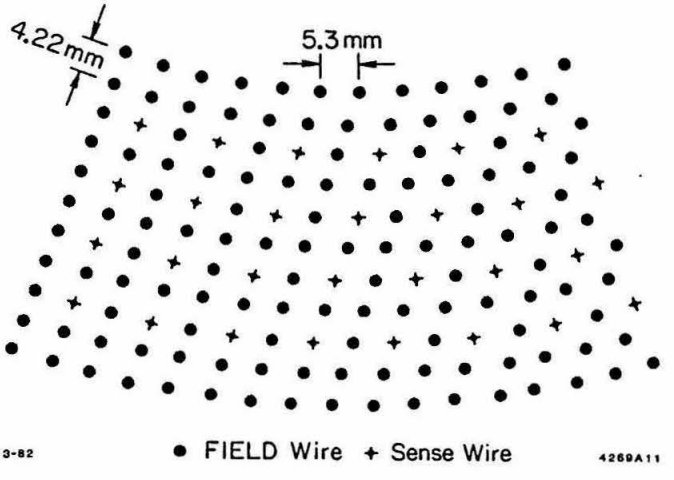

Figure 4.2. The configuration of sense (held at ground potential) and field wires (–2.25 kV) for one sector of the vertex chamber's inner band.

order to reconstruct the z-position of the track. The total momentum of a particle

can now be obtained from the z information, $p = p_{transverse}/\sin\theta$. The resolution on the measured transverse momentum of a charged particle in the magnetic field is:

$$\frac{\delta p_\perp}{p_\perp} = \left[(.01 p_\perp)^2 + (.025)^2\right]^{\frac{1}{2}}$$

where $p_\perp$ is in GeV. The first term on the right dominates at high momenta and arises from the error in sagitta incurred in a χ^2 fit of a helix to a set of wire hits. Dominating at lower momenta, the second term results from multiple scattering occurring mainly at the outer vertex chamber wall. The main drift chamber was operated at lower voltages than nominal for about 40% of the data. There is reasonable agreement between the data and Monte Carlo simulation for the drift chamber momentum and position measurements, and for the track reconstruction efficiency.[35] However, for the lower-voltage data set, the average momentum for Bhabha electrons is about 1.5 GeV lower than for positrons (see fig. 4.4).[35] Based on a Monte Carlo study, the tau analysis results in Chapter 5 do not depend sensitively on this effect because the event cuts select much lower momenta muon candidates where the problem is reduced. For Bhabha events (and more generally for low multiplicity events such as the candidate tau events where the muon is tagged by the muon system and therefore is far from the drift chamber edges and has momentum greater than 2 GeV), the track reconstruction efficiency is $\sim 99.8\%$.[35]

4.3 Time-of-Flight System

The Time-of-Flight (TOF) system consists of a ring of 48 plastic scintillator counters, read out on each end by a photomultiplier tube (see fig. 4.1). Passing through a counter, charged particles excite molecules in the plastic causing ultraviolet light emission that is then converted into visible light by a second material in the counter. The light travels the length of the counter by internal reflection and impinges on the photocathode of photomultiplier tubes, and by the photoelectric effect, liberates

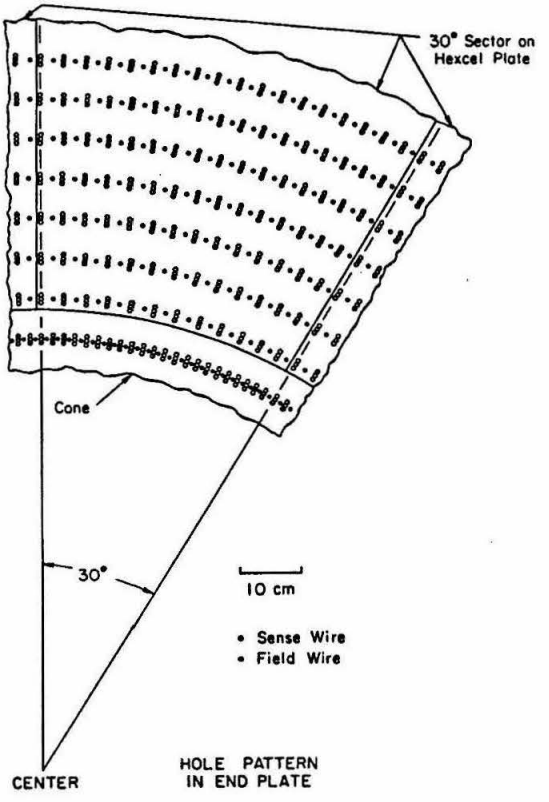

Figure 4.3. Main drift chamber wire configuration: seven large-celled layers and one small-celled layer are shown.

electrons which are then accelerated through a chain of secondary electron-emission electrodes, resulting in signal amplification. With fast electronics (though somewhat radiation damaged scintillators), the time resolution of the TOF is $\sim$ 360 ps when a single track hits a counter.

In this thesis, the TOF is used to reject cosmic rays that traverse one counter earlier than the beam crossing time (the other counter fires within the correct gate time) because the cosmic ray does not emerge from the interaction point. More importantly, the TOF is involved in the charged track trigger, discussed in a later section. For all of the analyses in this thesis, the Monte Carlo simulation of detection

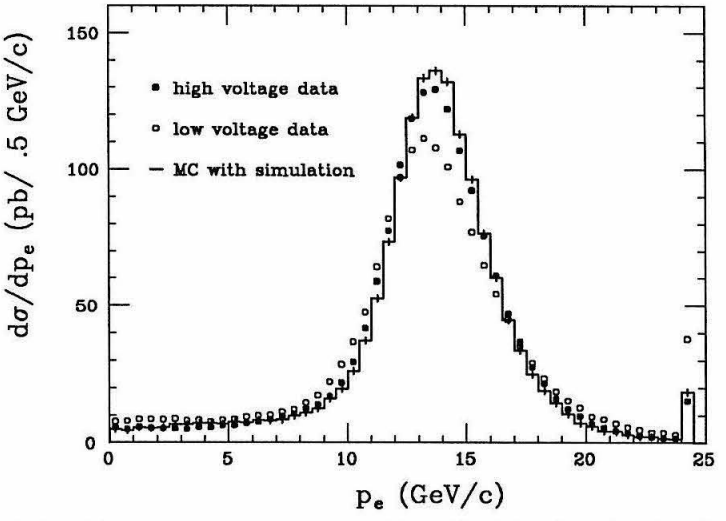

Figure 4.4. Momentum spectrum for Bhabha tracks for low and high voltage drift chamber data and for Monte Carlo Bhabha events which include full detector simulation. This figure is reproduced from ref. 35.

efficiency of the TOF counters is very nearly 100%; however, because of cracks between pairs of counters, the actual detection efficiency is somewhat smaller, 98.7%, and this correction must be applied to Monte Carlo events when TOF quality cuts are applied. Figure 4.5, from ref. 18, shows the detection efficiency vs the TOF azimuthal position for Bhabha electrons found by an independent trigger, the total energy back-to-back trigger.

4.4 Central Electromagnetic Calorimeter

A calorimeter is a device which measures the energy deposited by a particle in the material it traverses. The Mark II barrel calorimeter (called the LA system or liquid argon calorimeter), made of lead and liquid argon, was the largest of its kind when it was first built and operated at SPEAR and is very sturdy, surviving to do physics at PEP and then SLC. The LA system efficiently detects photons with energies from a few hundred MeV to many GeV, and discriminates electrons from hadrons and/or muons based on the way different particle species interact differently with material.

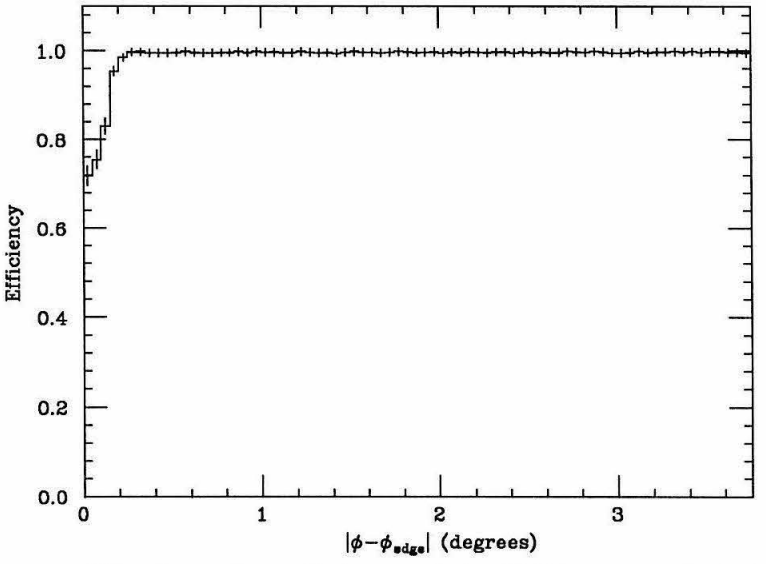

Figure 4.5. The detection efficiency of the TOF system for Bhabha electrons vs the difference in azimuth between the particle position and the nearest TOF counter edge. Detection requires signals from both photomultiplier tubes at the counter ends. Averaging the efficiency over ϕ gives a total efficiency of 98.7% per track.

As shown in fig. 4.1, the LA system is a ring of eight modules concentric with the drift chamber+TOF+solenoid magnet systems. Each module encases a stack of lead planes immersed in $\sim$ 1000 liters of liquid argon. The lead stack is 37 planes of 2mm thick antimony-strengthened lead; adjacent planes are separated by a 3mm liquid argon gap. Alternate planes were solid sheets held at ground potential. The other planes, segmented mostly into 3.8 cm strips, were placed at $\sim$ 3500 V. The energy of a particle incident on the calorimeter is absorbed mainly by lead where the atomic electrons are ionized. For electrons and photons, there would be many ionized particles, leading to shower development in the lead. Then the subsequent ionized electrons of the liquid argon drift towards the positive-potential lead strips, inducing an image charge that provides an electronic signal to be recorded. Only 12% of the ionization, from the argon, is collected. In order to reconstruct the *position* of the shower, the planes of lead strips were oriented at 0°, 90°, or 45° to the beam direction,

forming a "coordinate system," as shown in fig. 4.6. In front (closer to the beam) of these lead planes, there are three layers of 0.16 cm thick aluminum; each pair is separated by 0.8 cm of liquid argon. These planes help identify showers that began in the 1.3 radiation lengths of magnetic coil and are refered to as the "trigger gaps." To reduce the amount of readout electronics, strips oriented in the same direction were ganged (wired) together in depth as shown in fig. 4.7.

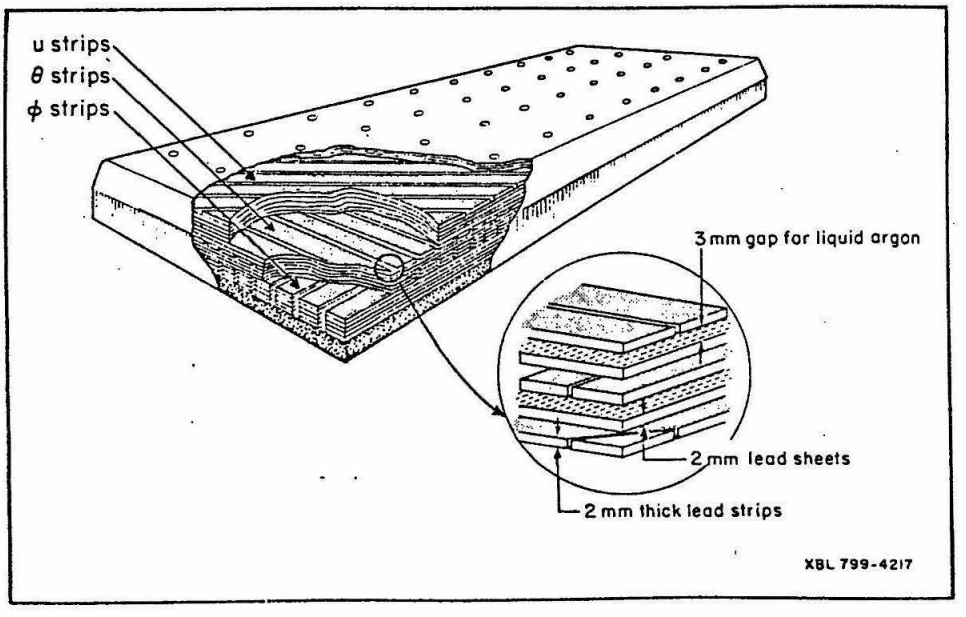

Figure 4.6. Idealized cutaway view of a liquid argon calorimeter module, showing the three possible orientations of lead readout strips.

Electrons and photons shower (deposit all their energy) when they traverse the calorimeter; muons ionize the material minimally, leaving a signal in the calorimeter equivalent to an electromagnetic shower energy of 200–400 MeV; hadrons may either ionize minimally or interact strongly with the atomic nuclei, leaving a broad "shower" deep in the calorimeter. Since this thesis is concerned with muonic tau decay events containing a photon, it is important to consider the behavior of photons and muons

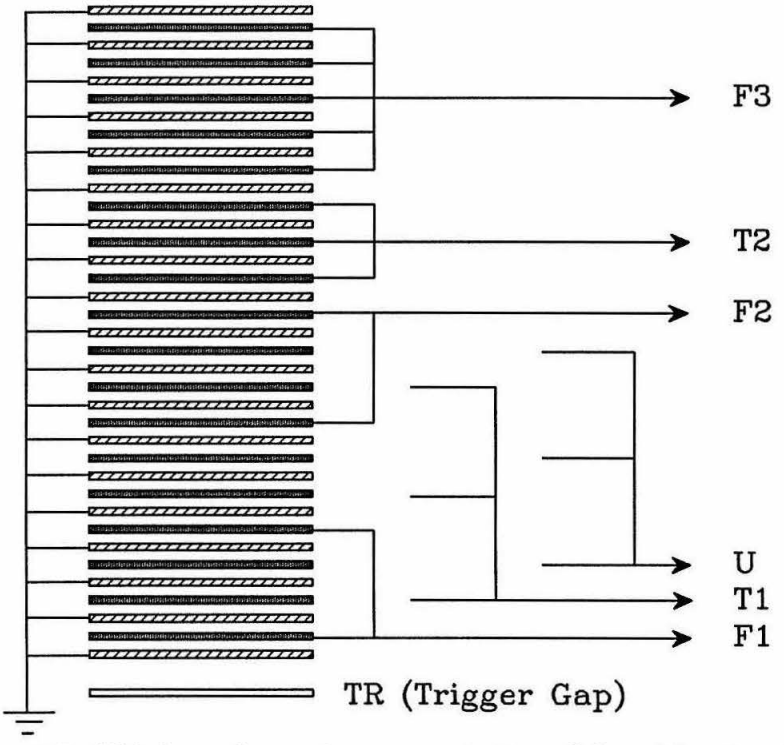

Figure 4.7. This is a schematic representation of the wiring together (labeled on the right) of the liquid argon calorimeter readout strips, where a particle enters at the TR layer and exits at F3. There are seven distinct readout layers: four to measure ϕ, TR, F1, F2, and F3; two to measure θ, T1 and T2; and one at 45°, U.

in the calorimeter more closely.

4.4.1 *Muons, Photons and Calorimeter Performance*

An incident photon with energy above $\sim$ 10 MeV will convert into an electron-positron pair, after traveling an average distance of $\sim 9/7\ X_0$,[36] which is approximately near the coil-calorimeter interface for the Mark II detector. Since photons in this thesis are defined as having ≥ 0.3 GeV energy, electron-positron pairs from such photons will still be very energetic. Energetic electrons lose energy by bremsstrahlung, producing many photons, which in turn produce more pairs, and so on. (As shown in Chapters 2 and 3, more massive particles radiate much less than lighter particles;

hence, muons and hadrons rarely bremsstrahlung in the calorimeter at $E_{cm} = 29$ GeV.) The chain process can result in a shower, producing thousands of electrons and photons. Eventually the average energy of these particles will decrease below some critical point ($\sim$ 7 MeV for lead) where the cascade process stops and ionization or atomic excitation for electrons, compton scattering and photoelectric effect for photons become the dominanat energy-loss mechanisms.

Shown in fig. 4.8 is the longitudinal shower profile for low and high energy *electrons* in the Mark II barrel calorimeter. For *photons*, however, the shower maximum occurs deeper in the module because the probability for photon conversion is less than for electron bremsstrahlung, but the ganging scheme of the calorimeter layers makes this effect less apparent (smearing). Therefore, an understanding of electron showers is sufficient to understand photons, and electrons have the advantage that their energy may be independently confirmed by the drift chamber momentum measurement. For showers, it is quite possible for some of the energy to be deposited in the magnetic coil and the amount is extracted from the trigger gap information; in addition, for high energy showers, there is about 10% leakage out the back of the module. Such losses are taken into account in the shower reconstruction algorithms.

Photon shower cores are approximately 3 cm wide, corresponding to about one strip width for the Mark II calorimeter (see fig. 4.9 which shows the transverse shower development). This width determines how close together a muon and photon (from $\tau^- \rightarrow \nu_\tau \mu^- \bar{\nu}_\mu \gamma$) may be in the calorimeter and still be distinguished apart. The strips subtend $\sim$ 1 degree and the closest angle for distinguishing the two particles turns out to be 1.8 degrees (see Chapter 5).

The calorimeter energy resolution is $\delta E/E \approx .14/\sqrt{E}$ (E in GeV), measured with Bhabha's from PEP. Radiative Bhabhas and/or radiative mu-pair events, where both charged tracks and the photon are within $|\cos\theta| < 0.7$ are useful for verifying the energy resolution agreement between the data and the Monte Carlo. Using only angle

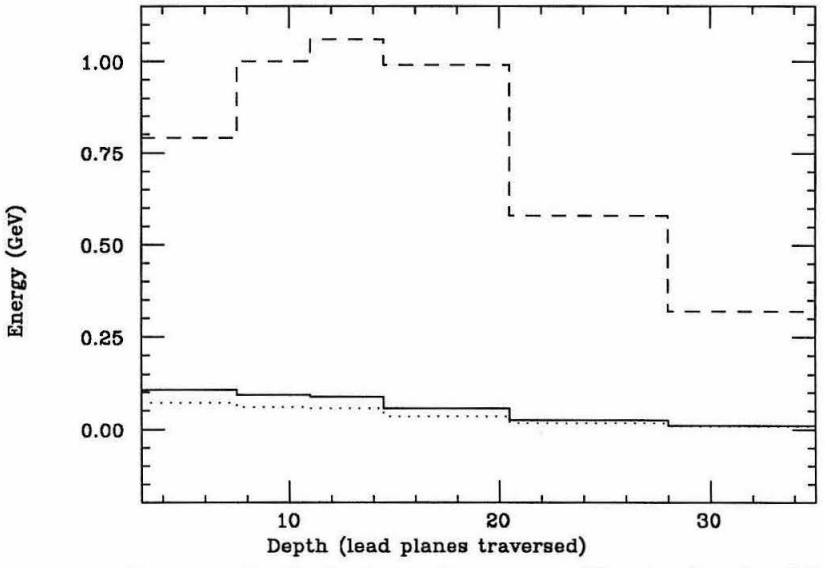

Figure 4.8. Longitudinal electron shower profiles in depth of lead planes traversed (the first three are aluminum planes and the energy deposited in these layers are only indirectly included in the calculation of shower energies and hence not shown above). The dotted line represents .5–1. GeV electrons and the solid line, 1.–2. GeV electrons, both from $e^+e^- \rightarrow e^+e^-e^+e^-$ events. The dashed line is from $\sim$ 14 GeV Bhabha electrons.

information, the expected energy of the photon may be calculated and then compared to the measured value. The agreement shown in fig. 4.10 for the Monte Carlo and the data energy resolution is sufficient for the analysis in this thesis. Various algorithms for smearing the Monte Carlo resolution (in ref. 35, ref. 21, and ref. 18) were tried for improving the resolution agreement with the data, but they do not alter the results of Chapter 5.

The angular resolution for energetic showers is $\sim$ 3.5 mrad (20% of a strip width), and for low energies is $\sim$ 8 mrad.[37]

The efficiency for detecting low energy photons was measured in ref. 37 using SPEAR data, and is $>$ 72% for photon energies above 0.3 GeV. This was checked for both Monte Carlo events with EGS[38] simulation for electromagnetic showers and for

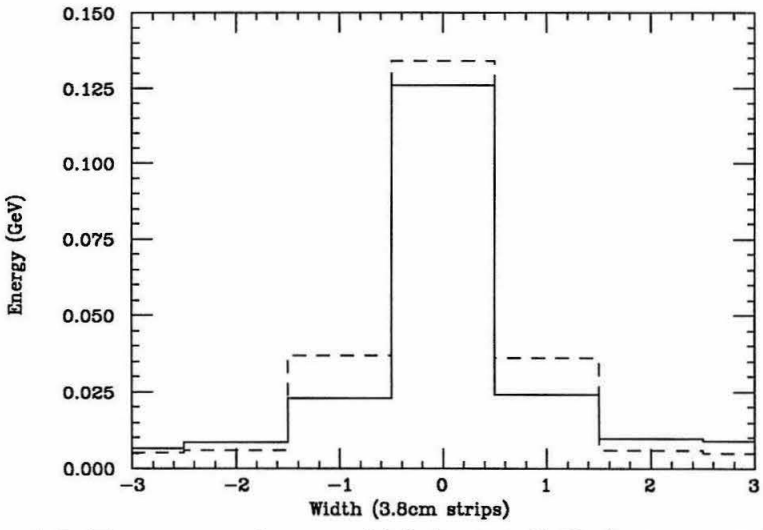

Figure 4.9. Transverse shower width for 1-2 GeV electrons at depth F1 (approximately layer 5 in fig. 4.8) and for ~14 GeV Bhahbas at T1 (approximately layer 10). A shower deposits most of its energy in 1 strip (taken to be the zeroth strip in the histogram and the adjacent strips are ±1, etc).

the data, and there is good agreement between them (see fig. 4.11). Using the decay $\psi \rightarrow \pi^+\pi^-\pi^0$, the momenta of the two charged pions and *one* photon from the π^0 decay are measured. Momentum-energy conservation allows a kinematic fit to determine the second photon's energy and direction, providing a check of photon detection efficiency and resolution. Because of gaps between each pair of the eight calorimeter modules, there is poor detection efficiency and energy resolution for showers near the barrel edges. Requiring Bhabha electrons to deposit at least 7.25 GeV of energy in the calorimeter, ref. 18 gives plots of detection efficiency vs calorimeter-ϕ-edge distance for tracks found by the drift chamber and projected into the calorimeter barrels (see fig. 4.12). To avoid reduced detection efficiency and a possible inaccurate Monte Carlo simulation of edge effects, the tagging photon is required to be 2.5 degrees away from the azimuthal edge and to be within $|\cos\theta| < .675$ (and also away from certain corner strips and mechanical-support regions).

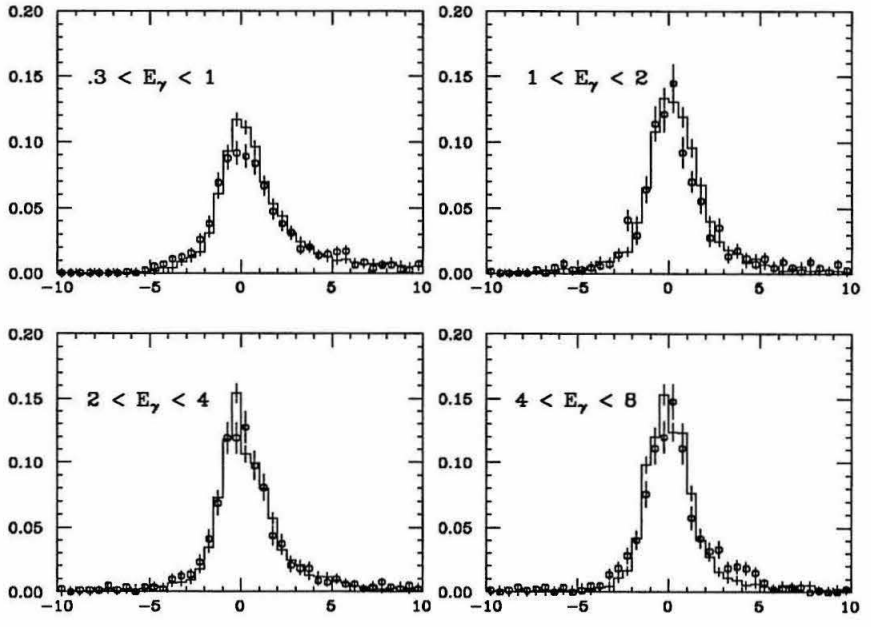

Figure 4.10. The difference between measured and calculated photon energy for radiative Bhabha events in the liquid argon calorimeter, where the error is taken to be $\delta E/E \approx .14/\sqrt{E}$ (E in GeV). The points represent the data and the solid line, Monte Carlo events with full detector simulation.

Small-angle Bhabha events, tagged in the Small Angle Tagger system (discussed later), are selected to study the level of spurious photons reconstructed from electronic noise hits in the calorimeter. As shown in fig. 4.13, there is $\sim$ 0.13% total probability of finding a spurious photon of energy $\geq$ 0.3 GeV (all modules). Another source of fake photons, important to the tau analysis of Chapter 5, occurs when there is a charged track in the calorimeter module, depositing energy on the long readout strips in some of the layers, which may coincide with noise in other layers to be reconstructed as a "photon" plus a charged track in the module. Since *muons* are used to tag the tau events in Chapter 5, it is important to measure the probability of this type of *fake* photons using *muons* in events where there is little chance of there being *real* bremsstrahlung photons. Cosmic rays provide just such events and the

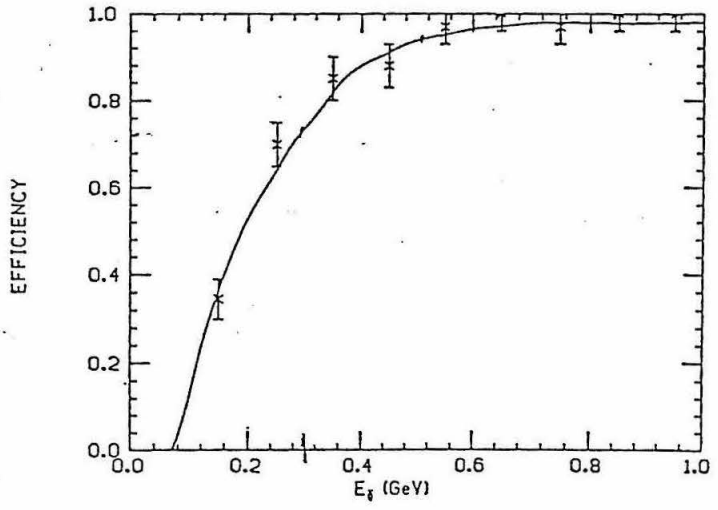

Figure 4.11. Photon detection efficiency measured in ref. 37, using mostly $\psi \rightarrow \pi^+\pi^-\pi^0$ events. The points are the data and the curve is Monte Carlo calculation.

total probability is found to be $\sim$ 0.1% for a fake photon of energy $\geq$ 0.3 GeV per module containing a muon track.

Muons traversing the calorimeter lose about 200-400 MeV photon-equivalent energy, primarily through ionization, depositing about 50 MeV in each read-out layer, and usually in only one channel/layer (the actual energy cluster width is negligible). Occasionally, a muon will suffer an energetic collision at small distances and transfer enough energy to the "knocked on" electrons (called delta rays), which themselves can initiate secondary ionization and create a shower. This results in the famous asymmetric distribution in energy loss for muons (Landau tail). Figure 4.14 gives the spectrum of energy deposited in the calorimeter by cosmic rays (muons), showing the upward fluctuations. For muons with momentum between 2 – 14 GeV, the probability of depositing > 0.6 GeV (twice the average energy) in the calorimeter is only about 1.7%. At E_{cm} = 29 GeV, the probability for muons to bremsstrahlung and thereby shower in the calorimeter is of the order $O(10^{-4})$, even smaller than the probability

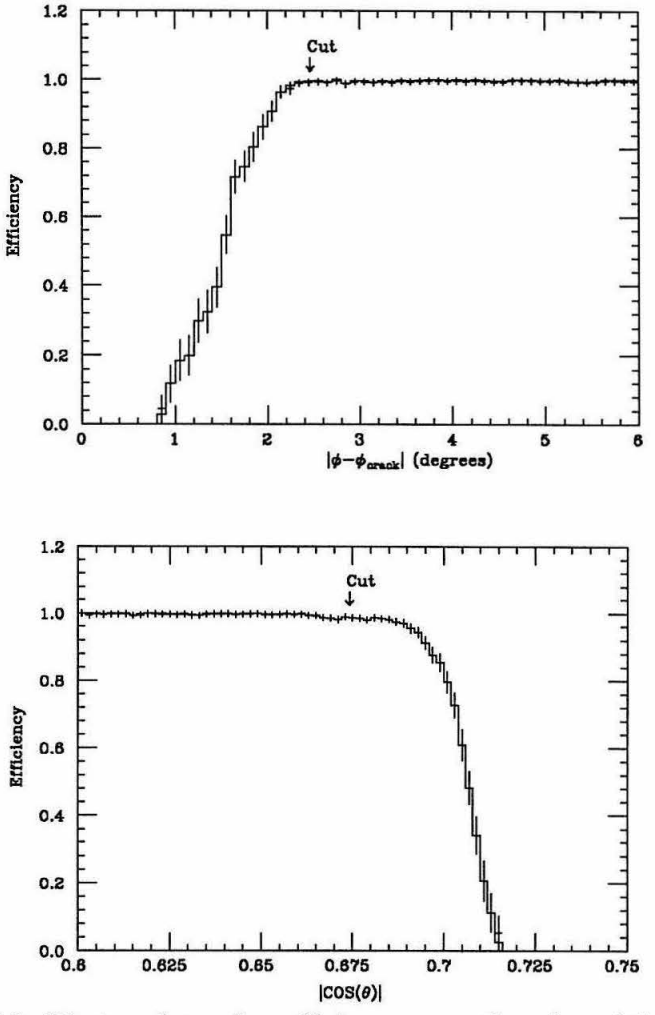

Figure 4.12. Photon detection efficiency near the edge of the calorimeter in the azimuthal (ϕ) and polar (θ) directions. For the ϕ plot, the Bhabha tracks are required to be well in the calorimeter in θ, and vice versa for the θ plot. These histograms are from ref. 18.

for δ rays. The typically narrow, well-defined energy deposition for muons makes this the tau decay mode best-suited for measuring decay radiation.

Minimum-ionizing particles, like muons or (often) pions, deposit the energy equivalent of only a few hundred MeV, for which the detection efficiency is only $\sim$ 50% (see fig. 4.11); therefore, tracking information from the drift chamber is used to guide the calorimeter reconstruction for charged tracks increasing the probability

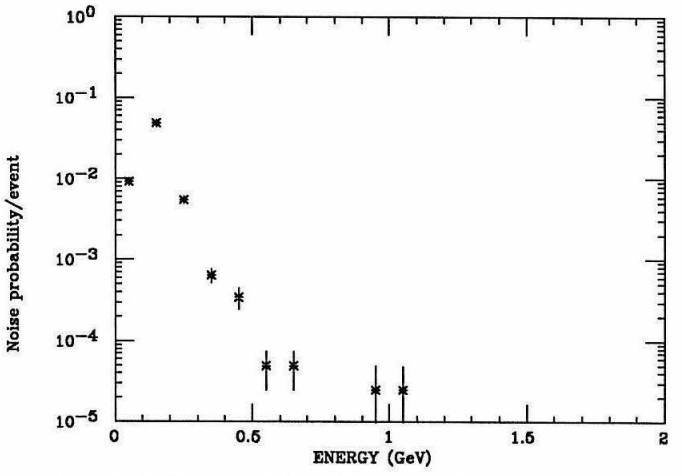

Figure 4.13. Probability of fake photons due to electronic noise in the barrel calorimeter. The probability for individual modules is 1/8 of the above values.

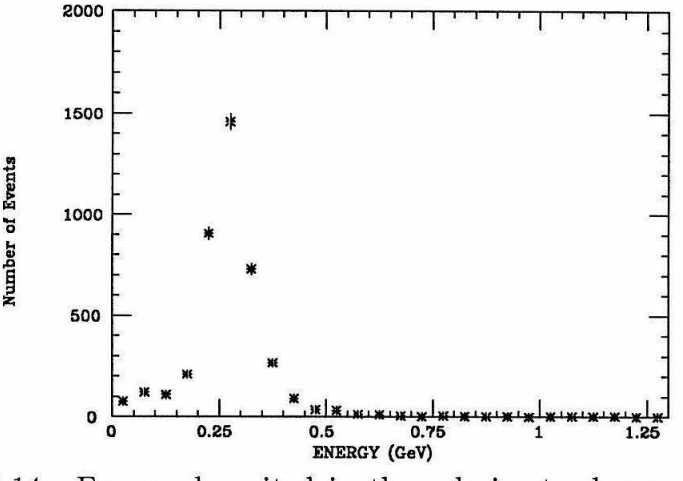

Figure 4.14. Energy deposited in the calorimeter by cosmic ray muons with momentum between 2 – 14 GeV.

of finding the small energy deposition. Charged particles' energies are reconstructed first before attempting to find neutral showers : a track is projected from the drift chamber through the layers of a liquid argon module. Energy deposited within a few strips of the projected position is then associated with that charged track. If a track position is mis-reconstructed by the drift chamber or if the track misses the interaction point (*e.g.*, a cosmic ray), then there is sometimes no calorimeter information

associated with the track; the associated energy may instead be reconstructed as a separate photon track, thus creating a fake charged-track-plus-photon candidate. To avoid this problem, all μ-γ candidates are required to have calorimeter information for the muon. Generally, the extrapolation is adequate for a correct association of the charged track with its calorimeter energy and this is adequately modeled by the Monte Carlo (see fig. 4.15 from ref. 35, showing the difference between the shower position, measured by the calorimeter, and the drift chamber projected position).

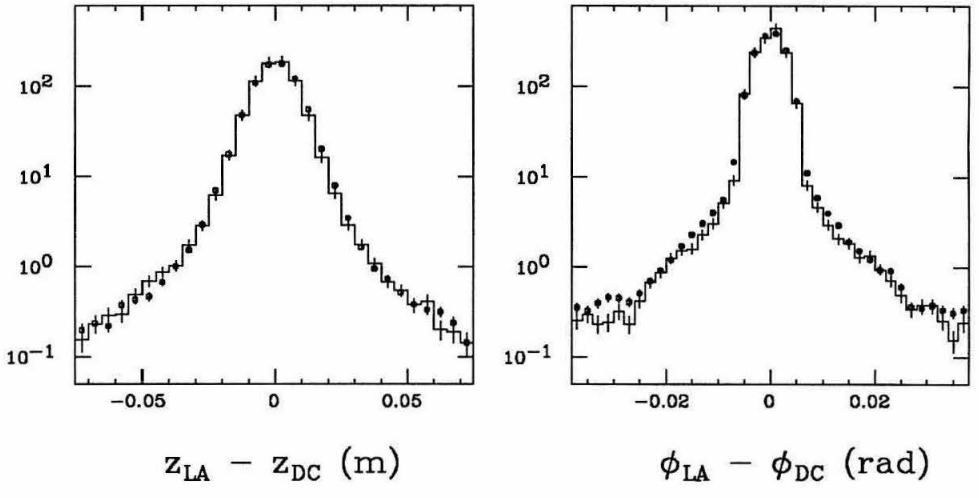

Figure 4.15. A comparison of the shower position measured by the calorimeter with the position of a drift chamber track projected to the first layer of the calorimeter. Shown are Bhabha showers with the data in dots and the Monte Carlo in histogram.

The final step of the event selection criteria in the radiative tau analysis is to reconstruct the invariant mass of the candiate μ-γ pair. For muon momenta measured by the drift and vertex chambers, and photon energies measured by the LA system, the resolution on the μ-γ mass is $\sim$ 0.13 GeV for masses much below 2.0 GeV and $\sim$ 0.5 GeV for masses much above 2.0 GeV. These resolutions are estimated using Monte Carlo events with full detector simulation.

4.5 Endcap Calorimeter

The drift chamber is covered on each end by an endcap calorimeter, made of four planes alternating between solid sheets of lead and multiwire proportional chamber (the MWPC consists of a layer of equally spaced anode wires sandwiched between outer layers with cathode strips painted on them), altogether having about 2.3 radiation lengths of material. Each endcap covers the region $0.76 \leq |\cos\theta| \leq 0.96$, but has a cutout for a support stand, so that the coverage in ϕ is only about 70%. Though the detection efficiency is high (greater than $\sim$ 97% for photon energies $>$ 1 GeV), the energy resolution is $\delta E/E \approx .5/\sqrt{E}$ (E in GeV), which is poor enough that this system is used only to veto events with energetic photons or electrons detected in the endcaps. Using wide-angle Bhabhas, where the tracks are detected in the region $|\cos\theta| < .7$, the probability of a fake photon due to electronic noise with energy $>$ 1 GeV is found to be $<$ 0.1%.

4.6 Muon Detector

The muon system is comprised of four walls, above, below and on either side of the Mark II detector (see fig. 4.1). Each wall contains four layers of steel, with each layer followed by signal-readout layers. The thicknesses of the steel planes vary from 1.4 to 1.8 nuclear interaction lengths; therefore, pions, which have not interacted in the liquid argon calorimeter and survive to reach the muon system, generally undergo nuclear interaction in the first or second steel layer and are stopped. Muons multiple-scatter and lose a small amount of energy, mostly by ionization, but are able to reach the fourth layer if their momenta are above $\sim$ 1.8 GeV.

The signal-readout layers are proportional wire tubes running the length of the steel planes (about 18 feet long, depending on wall and layer). Tubes in the first layer (closest to the beam) are oriented to measure the polar angle, and the other layers measure the azimuthal angle. Groups of eight tubes form a module and a cross

sectional view of such a module is shown in fig. 4.16. The triangular shape of the tubes are for strength and for maximizing the charged particle detection efficiency. Muons traversing the tube ionize the argon-CO_2 gas; the liberated electrons drift towards the wire held at 2 kV, where they undergo gas avalanche and induce a signal on the wire.

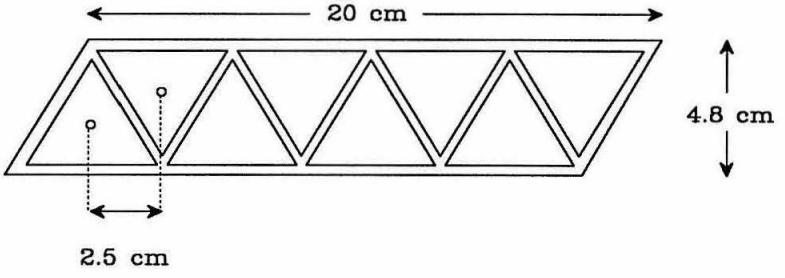

Figure 4.16. Cross sectional view of a muon proportional tube module. The tubes are made of extruded aluminum and contain a gold-plated tungsten sense wire in the center.

4.6.1 Muon Detection Efficiency and Pion Misidentification

Muon candidates are identified by extrapolating charged tracks from the drift chamber to the first three layers of the muon system, and from the position of detected hits in the second and third layers, the projection is finally extrapolated to the fourth layer. If the position of a proportional tube with a signal is within 3 root-mean-square(σ) deviation from the predicted position of a track in all four muon layers, then the track is considered a muon. The 3 σ search region is reduced to 2 σ for the last layer which is electronically noisier than the other layers and would have increased the probability of misidentifying hadrons as muons.

The predicted position is calculated by taking into account dE/dx losses, range straggling, multiple Coulomb scattering, and bending in the magnetic field (wherever

the steel absorber served as flux return). The largest contribution to the extrapolation error is due to multiple scattering of the muon off nuclei in the magnetic coil, the calorimeter, and mainly in the steel absorbers preceding the muon readout tubes. Given by Rossi and Greisen, the mean square scattering angle at depth X is:[39]

$$< \theta >^2 = t(E_0/\beta \mathrm{p})^2 \quad E_0 = 21 \text{ MeV}$$

where t = X/(radiation length of material) is the absorber thickness, β is the velocity and p, the momentum (in MeV) of the incident particle. The root-mean-square (σ) deviation is computed by adding the independent effects of all the traversed detector elements (i) in quadrature. For each layer, which measures only one coordinate (call it x), the deviation is taken to be:

$$\sigma_x^2 = \sum_i \theta_i^2 \left(\mathrm{D}_i^2 + \frac{\mathrm{T}_i^2}{12} \right) + \mathrm{D}_{res}^2$$

where θ_i is the rms multiple scattering angle, D_i is the distance to the detector plane, T_i the thickness of the scattering element (the 12 factor accounts for the uncertainty in the discretely-spaced positions of measurement). The last component, D_{res}, is the extrapolation error due to the drift chamber resolution which is about 2.5 cm and largest for the muon layers measuring the polar angle, θ. The muon chamber sense wires are spaced 2.5 cm apart to match this extrapolation error. Altogether σ_x is on the order of 5 cm for the first layer and 10 cm for the last. Figure 4.17 shows a plot of the difference between the predicted and measured positions divided by the calculated error σ_x. Since these "pulls" are not of unit width, and assuming the distribution is gaussian, it appears that σ_x has been overestimated by $\sim$ 35% over the actual deviation; therefore, the "3" σ search region for muon candidate tracks is somewhat larger than the true "3" σ value. This is not a serious problem, however, since muon and pion identification probabilities can be measured directly from the

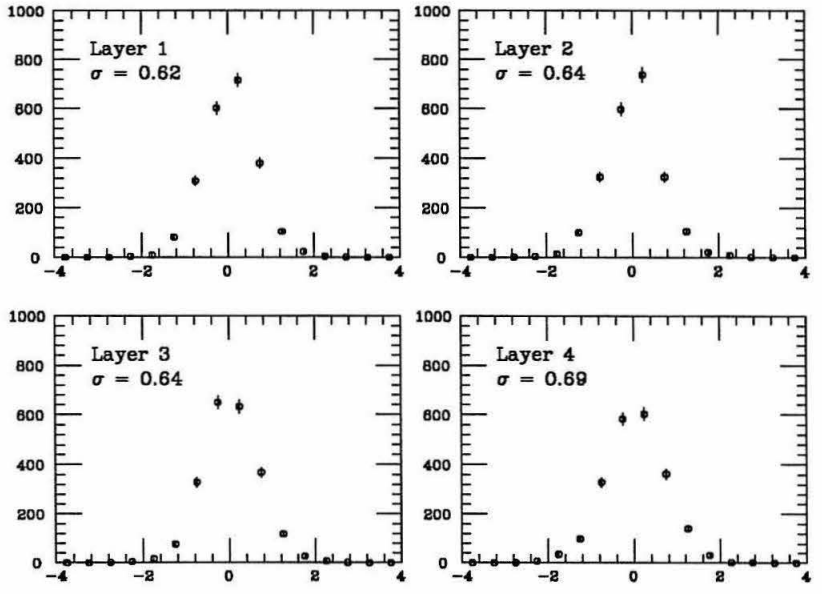

Figure 4.17. Difference between the measured and predicted track position in the muon system, divided by the calculated standard deviation σ_x described in the text. The muon layer number (1 is closest to the interaction point) and the standard deviation σ of the distribution shown above are given as well.

data.

Figure 4.18 shows the muon identification efficiency is about 75–85% as measured from $e^+e^- \rightarrow e^+e^-\mu^+\mu^-$ and $e^+e^- \rightarrow \mu^+\mu^-(\gamma)$ events. Because of low statistics, there are large errors on the efficiency values for lower-momenta muon data; however, the general trend shows the data efficiency to be about 10% lower than expected from the Monte Carlo. The efficiency is measured for tracks lying within the muon acceptance and having momentum ≥ 2 GeV. Because the muon readout tubes are of varying lengths and the coverage of the outermost layer is only $\sim 45\%$, it is costly to impose simple acceptance requirements on $|\cos\theta|$ or ϕ. Instead, if a trajectory is no more than $3\sigma_x$ outside of the individual tube edges and its range is no less than $-3\sigma_{range}$, then it is defined to be within the muon system acceptance.

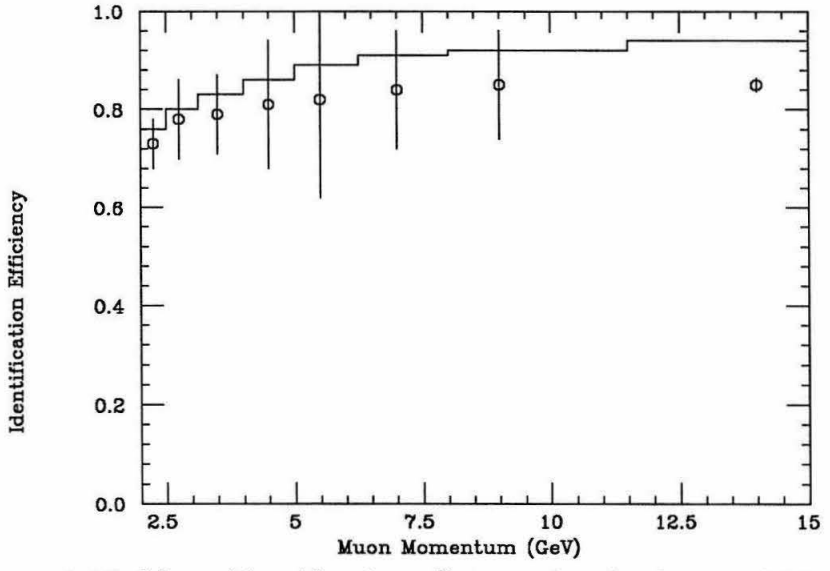

Figure 4.18. Muon identification efficiency for the data and Monte Carlo after full detector simulation.

Detailed discrepancies between actual and Monte Carlo detection efficiencies can sometimes be corrected by better simulation (and sometimes by fixing program bugs, see fig. 4.19), but more often, it is preferable to apply correction factors or event weights to the predictions of a Monte Carlo program.

Several factors cause the muon identifcation 15–25% inefficiency, measured in ref. 39and ref. 34. Multiple Coulomb scattering, which is greater for lower momenta tracks because they scatter through larger angles, contributes about 1% for a 3σ search region about the projected track. Range straggling (variations in ionization energy loss resulting in fluctuations in range) adds 3–6% inefficiency for muons of momentum between 2.0–14.5 GeV. The inefficiency due to proportional tube electronics contributes about 3%. The extrapolation errors from the drift chamber, muon system edges, wall position, etc., contribute the bulk of the remaining inefficiency.

Other particles may pass the muon identification criteria; the probability is much less than 1% for electrons and on the order of 1% for hadrons. Energetic hadrons that don't undergo nuclear interaction may punch through all layers of the muon

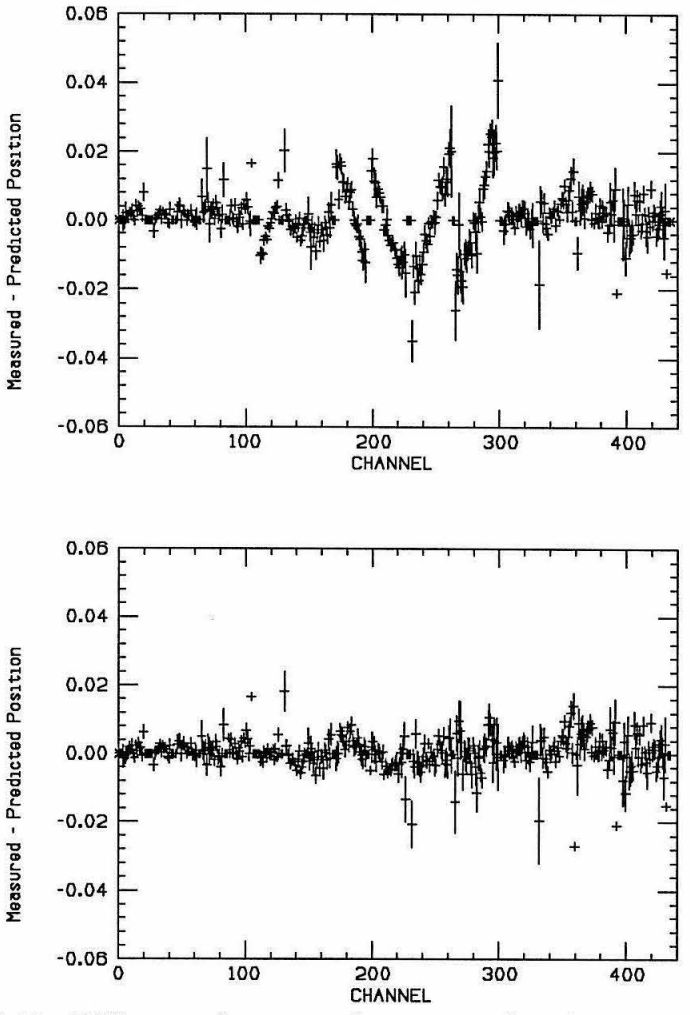

Figure 4.19. Difference between the expected and measured position of a muon track vs the muon readout module numbers, which are ordered so that physically adjacent modules of a particular layer and wall are grouped together in the above plot. In the upper plot, the segments that are skewed and different from zero result from the entire layer being predicted to be either closer or farther in radial distance (in the database) from the interaction point than actual. This problem does not occur for Monte Carlo events. By revising the radial distance in the database, it is possible to improve the situation somewhat, with results shown in the lower figure.

system; or hadrons may punch through the first few layers and then combine with an electronic noise hit in the last layer to pass the muon-identification algorithm. About

5% of all charged tracks in the muon fiducial volume have a random hit in the last layer. Finally, secondary tracks from a strong interaction cascade or from hadron decay (to a muon) may penetrate the muon walls and be misidentified as a direct muon from the interaction point.

In the radiative tau analysis (Chapter 5), the main contribution to tau misidentification background is from hadronic tau decays; since most of the hadrons (one-charged prong) are pions ($e.g., \tau^- \rightarrow \nu_\tau \rho^- \rightarrow \pi^-\pi^0\nu_\tau$) rather than kaons (the ratio is $\sim$ 20:1), it is more important to measure the misidentification probability for pions than for other hadrons. In any case, the misidentification probability for reconstructed kaons is comparable to that for pions.[40] The section on Misidentified Taus in the Appendix describes how the pion misidentification from pion punchthrough and from decay to muons is measured.

4.7 Small Angle Luminosity Monitor

There is a Small Angle Tagger device, covering the polar angle from 21 to 81 mrad, on either side of the Mark II detector (see fig. 4.1). Each device contains three layers of planar drift chambers, small precisely-placed scintillators (precise counters), large plastic scintillator (gross counters), followed by a calorimeter (see fig. 4.20).

Because of the beam pipe, the scintillator counter-calorimeter were halved into two modules and their signals are read out individually (four modules altogether for the entire SAT system, two on either arm of the Mark II). The calorimeter has eighteen alternating layers of lead and plastic scintillator. None of the layers are segmented; therefore, only the total energy deposited may be read out for each of the four calorimeter modules. Electromagnetic showers are well contained in the $\sim$ 20.4 radiation lengths of lead in the calorimeter, and the energy resolution is $\delta E/E \approx .15/\sqrt{E}$ (E in GeV).

Only the gross counter and calorimeter are used in this analysis to tag scattered

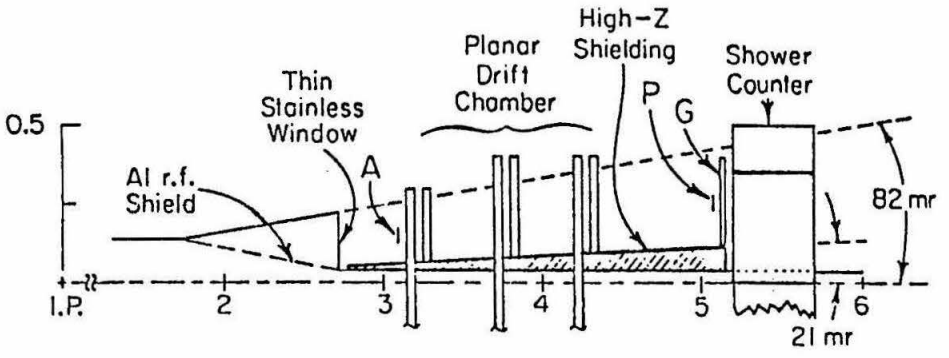

Figure 4.20. The Small Angle Tagger system, where the dimensions shown are in meters. Only the lead-scintillator calorimeter and the plastic scintillator labelled G are used in the analyses.

electrons in two-photon events ($e^+e^- \rightarrow e^+e^-\mu^+\mu^-$, see Appendix) or to reject radiative and two-photon background events in the tau analysis (Chapter 5). A charged particle traversing this region would be detected in both the gross counter and the calorimeter, and a neutral particle only in the calorimeter. For the tau analysis, an event is rejected if the maximum energy among the four SAT calorimeter modules is > 3.5 GeV, or if there is > 2 GeV in a calorimeter module and a gross counter hit associated with the same module. The inefficiency introduced by these vetos is $< 1\%$ (see fig. 4.21 and fig. 4.22), as measured from events with Bhabha electrons in the barrel calorimeter.

4.8 Mark II Trigger

The Mark II detector at PEP has a two level trigger for logging interesting events with only about 7% dead time. The level 1 and 2 trigger efficiencies of the ($\tau^- \rightarrow \nu_\tau \mu^- \bar{\nu}_\mu$)–like events as defined by the stringent cuts described in Chapter 5 are almost 100%. In particular, the requirements of a > 2 GeV muon, of at least 2 charged tracks of good quality, of a back-to-back topology and minimum visible energy, and of the time-of-flight, all help ensure that the event would have passed the

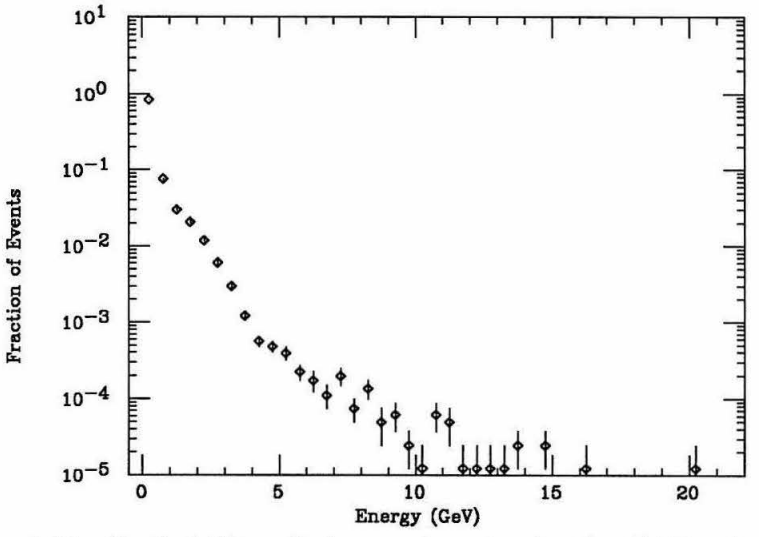

Figure 4.21. Probability of electronic noise in the SAT calorimeter, as measured in wide-angle (liquid argon calorimeter) Bhabha events. The values shown are for the maximum energy among the four modules in each event.

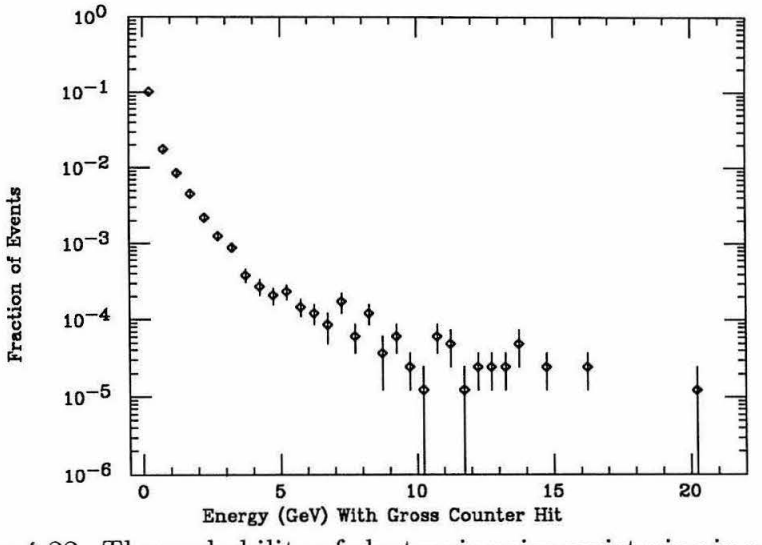

Figure 4.22. The probability of electronic noise registering in a SAT calorimeter module simultaneous with a signal in the associated gross counter.

charged trigger criteria.

The time between beam crossings is 2.4 μsec and the primary trigger decides

within 1 μsec afterwards whether to reject the event immediately or to let the secondary trigger start processing. The primary trigger condition is satisfied at a rate of $\sim$ 1.5 kHz by one of three main ways: the charged particle trigger, the total energy in the calorimeter, and for low-angle Bhabhas, the SAT trigger.

If the primary trigger is satisfied, then a signal is sent to the secondary trigger for the latter to start processing. Taking about 34 μsec to process, the secondary trigger is satisfied at a rate of $\sim$ 3 Hz, after which all the electronics are read out and the event is logged to tape (data acquisition takes $\sim$ 40 msec). Only the charged part of the level 2 trigger is relevant to the tau analysis; it requires that the drift chamber and vertex chamber hits along with TOF information indicate the presence of $\geq$ 2 charged tracks, called A-tracks.

The A-track condition is checked by 24 electronic "curvature" modules, 12 devoted to positively charged tracks, and 12 to negative. The modules are sophisticated shift registers to detect if the pattern of hits in various drift and vertex chambers layers align sufficiently, indicating the passage of a charged track. Each module looks for tracks within a certain range in radius of curvature, corresponding to a particular range in transverse momentum (see fig. 4.23). The modules are designed to find tracks lying within the central part ($\sim$ 67%) of the detector solid angle and with transverse momentum above $\sim$ 130 MeV. For most of the data, however, this threshold was only $\sim$ 65 MeV because the magnet had to be operated at half field after a short. In addition to identification by a curvature module, there must be a signal on both phototubes of the TOF counter associated with the track for it to be called an A-track. The cracks between each pair of TOF counters lead therefore to a $\sim$3% inefficiency for detecting two-charged-track events.

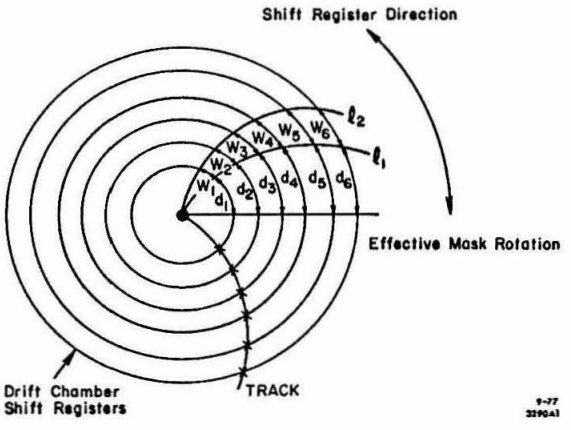

Figure 4.23. This is a simplified illustration of how the charged track trigger searches for hits in the different layers of the drift and vertex chambers, checking if they align within a certain width w_i defined by the arcs l_1 and l_2. All the sense-wire patterns of hits and non-hits of a particular layer are clocked through a shift register. Each layer is clocked through with different delays d_i to account for the different radii of the layers and to vary the detectable curvature.

Chapter 5

Data Analysis

Ah finally .... All of the major analysis steps are presented in this chapter. The event selection procedure and the motivation for the cuts are first presented. Next, there is a discussion of the backgrounds and the expected contribution from each of them and from the signal. Finally, the measurements for radiative tau decay branching ratio, $B(\tau^- \rightarrow \nu_\tau \mu^- \bar{\nu}_\mu \gamma)$, and the number of events from radiative tau production $e^+e^- \rightarrow \tau^+\tau^-\gamma$ are presented and analyzed. The measurements are obtained using the Mark II data taken at $E_{cm} = 29$ GeV with a total integrated luminosity[33] of $207.9 \pm 0.5 \pm 2.8$ pb^{-1}.

5.1 Characteristics of Tau Events

Tau pairs in e^+e^- experiments are produced collinearly unless hard initial-state radiation is emitted. Final-state radiation and decay radiation do not typically alter the event topology. Taus are detected by their decay products, which emerge well collimated along the original τ direction because of the Lorentz boost at $E_{cm} = 29$ GeV. The decay products are characterized by low-charged multiplicity, containing usually one or three charged tracks, and by missing energy due to at least one undetected neutrino. The event selection criteria, which will exploit these properties, are divided in two groups, signal selection and background rejection. There are *two* signals for this analysis, 1) radiative tau production where one tau decays to a muon,

and 2) radiative tau decay to the muon mode. Whenever one of these two is being measured, the other signal is considered a background.

5.2 Event Selection Criteria

This analysis is restricted to the case where at least one tau decays to a muon. In addition, one photon is required to be detected near the muon, as an indication of radiative tau production or of radiative decay. The muon mode allows the detection of a separate photon track more readily than the electron or pion modes because the electron/pion deposits more energy and leaves wide energy showers in the calorimeter. Muon tracks are minimum ionizing and generally deposit energy only on one strip-per-layer as they traverse the Mark II barrel calorimeter, where one strip width is about 3.8 cm and subtends $\sim 1°$. In order to maintain high detection efficiency, the other τ is allowed to decay to any mode, including the muon mode. Candidate events must pass the following criteria:

- 2 to 6 charged tracks, each with drift chamber momentum (p) $>$ .15 GeV.
- Accepted tracks must satisfy the following requirements:

  ≥ 8 drift chamber hits,

  quality of the track fit χ^2/(degree of freedom) $< 8.$,

  distance of closest approach to the beam collision point in the plane transverse to the beam direction < 6 cm and < 9 cm along the beam direction.

  At least 2 tracks in a $<$ 4-charged track event, and at least 3 tracks in a $\geq$ 4-charged track event, must satisfy these quality cuts.
- At least one charged track with p $\geq$ 2 GeV must have associated signals (see Chapter 4 for exact definition) with it in all four layers of the muon system. The muon candidate must be isolated from other charged tracks by $> 90°$, a requirement which naturally divides the event into two hemispheres.
- Only one photon reconstructed in the barrel calorimeter, as described in Chapter 4, with energy $\geq$ 0.3 GeV is allowed within 90° of the muon candidate.

All of the above requirements have a high efficiency for selecting the muonic tau signal, except for the muon identification criterion itself, which suffers from the $\sim$ 45% solid–angle coverage of the muon system. From Monte Carlo τ pair events, where exactly one τ decays to the muon mode, the muon identification requirement alone, including the momentum condition p$\geq$ 2 GeV, has an efficiency of only $\sim$ 21%.

5.3 Background Rejection

Expected backgrounds include radiative two-photon, radiative μ-pair and misidentified hadronic tau decay events. Backgrounds from multihadronic events, cosmic rays and events with spurious photons due to electronic noise in non-radiative tau events are much smaller. Suppressing these various backgrounds requires a variety of cuts. Generally, applying a combination of loose cuts rather than one stringent cut better removes a particular background without sacrificing the signal.

Two photon processes are characterized by low visible energy in the central part of the detector, momentum balance transverse to the beam direction, and high energy loss towards the beam direction, all because the incoming electron and positron scatter at low angles. Requiring the presence of a detected photon in the event significantly suppresses two-photon backgrounds because of the small cross section for events with photons emitted at wide angles.[41] This background is further rejected by requiring the energy balance along the beam to satisfy:

$$\frac{|\sum_i p_{z_i}|}{|\sum_i \vec{p}_i|} \quad < \quad 0.92$$

where the summation is over charged and neutral tracks (see fig. 5.1). In addition, there are requirements on the total energy (E_{VIS}) and on the transverse momentum ($P_\perp$) for the event, which include contributions from both charged and neutral particles. For events with $>$ 2 charged tracks, the E_{VIS} is required to be $>$ 6 GeV. For 2-charged track events, E_{VIS} is required to be $>$ 3 GeV, and if $P_\perp$ $<$ 3.5 GeV then

E_{VIS} must be > 6.5 GeV. The E_{VIS} variable is useful in removing radiative mu-pair background as well. As shown in fig. 5.2, two photon events generally have lower E_{VIS} and radiative mu-pair events have higher E_{VIS} than radiative tau events.

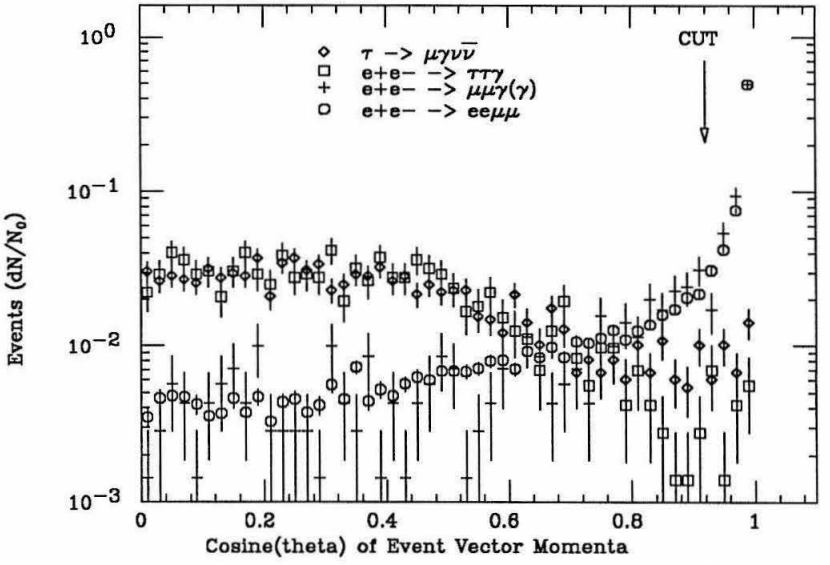

Figure 5.1. Energy balance along the beam direction for tau-pair, $e^+e^- \rightarrow e^+e^-\mu^+\mu^-$, and $e^+e^- \rightarrow \mu^+\mu^-\gamma(\gamma)$ events, where a cut is made at .92 to remove the latter two background processes. A total event energy cut, shown in the next graph, has already been applied. For this and the next few plots, events are normalized to one.

Radiative μ-pair events carry the full 29 GeV center–of–mass energy when all the tracks are detected. Therefore, missing energy due to undetected neutrinos in τ events allows kinematic discrimination against radiative μ-pair events. This background is suppressed by demanding the following for 2-charged track events: E_{VIS} to be < 24 GeV (see fig. 5.2), and the acoplanarity to be > .25° and > 1° if both tracks are consistent with being muons. The acoplanarity is defined to be the acollinearity in the plane (xy) transverse to the beam direction of the total momentum of the charged track plus nearby photons in each hemisphere. Acoplanarity is a useful variable when the emitted photon is very near one of the muon tracks, giving an

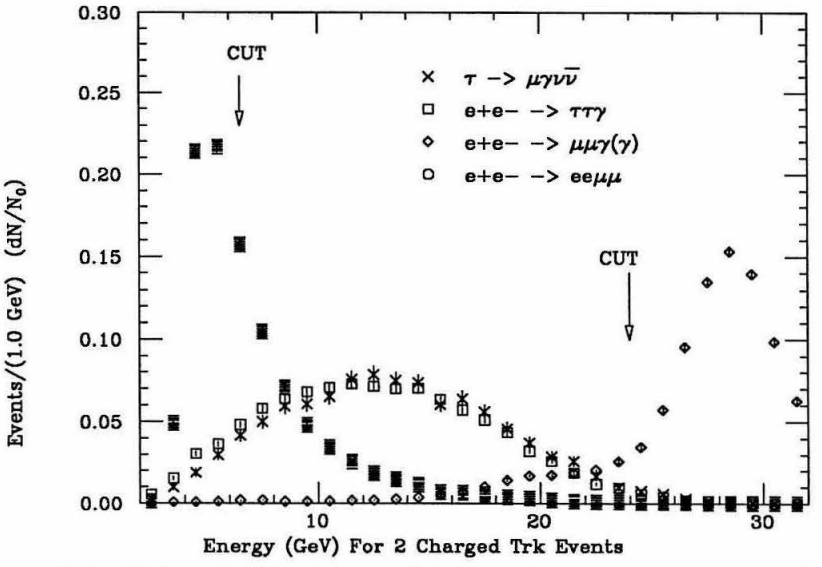

Figure 5.2. Total visible energy for two-photon processes such as $e^+e^- \rightarrow e^+e^-\mu^+\mu^-$ events and for radiative mu-pair and tau-pair events. The spectrum shown is only for events with two charged tracks. The arrows indicate where a cut is made to remove mu-pair and two photon backgrounds (see text for explanation).

event with essentially two back-to-back charged tracks. Because momentum and angle measurements have smaller errors in the xy-plane, an acoplanarity cut is preferable to an acollinearity cut, which uses both xy and z information. When the emitted photon is well separated from the charged tracks, radiative mu-pair events are removed more effectively by requiring the event kinematics to be inconsistent with the $e^+e^- \rightarrow \mu^+\mu^-\gamma$ hypothesis. A χ^2 is formed from the measured and predicted momentum of the two charged tracks and photon, and from the errors on the measured values. The predicted momenta of the tracks may be obtained from angle measurements alone which have much smaller relative errors than the direct energy or momenta measurements. As shown in fig. 5.3, events are rejected if the $\chi^2/3$ is less than 40.

There are also backgrounds from higher order radiative μ-pair events, characterized by missing energy from hard initial-state radiation emitted close to the beam direction. These events are almost completely eliminated by requiring the missing

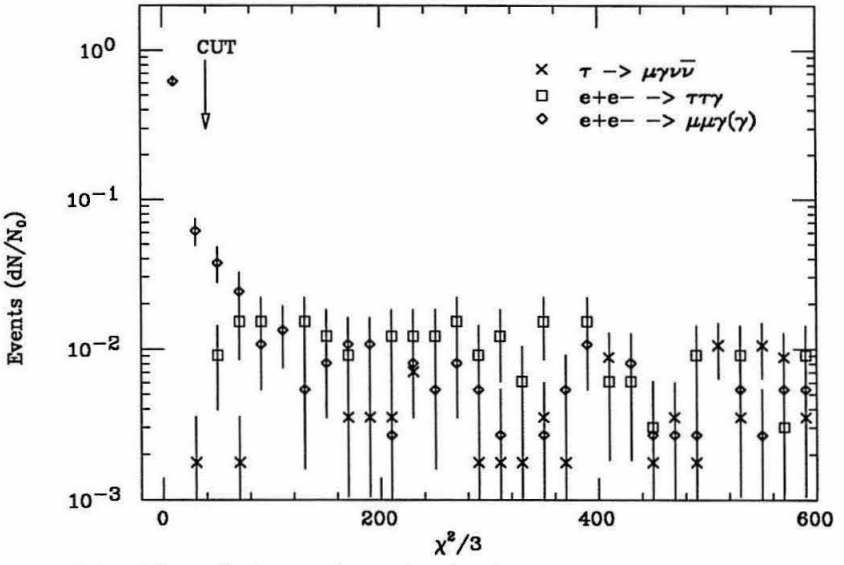

Figure 5.3. The χ^2 formed to check if a two-charged prong event is consistent with being a $e^+e^- \rightarrow \mu^+\mu^-\gamma$ event. A cut is made at $\chi^2/3 = 40$ to remove radiative mu-pair background. Missing points lie below the range shown on the vertical axis.

mass squared to be inconsistent with a photon mass. The missing mass squared calculated from charged tracks must be < 50 GeV^2 (shown in fig. 5.4), and from charged and neutral tracks must be < 20 GeV^2. In addition, a χ^2 is formed from the measured and predicted momenta, assuming the missing energy is along the beam axis, and using angle measurements alone.[21] Events are rejected if the $\chi^2/3$ degrees–of–freedom is less than 30 (see fig. 5.5). Because hard-initial-state radiative and two photon processes sometimes emit electrons/positrons and photons at low angles, events with total endcap-calorimeter energy > 8 GeV or with SAT system hits are discarded. An event is rejected if the maximum energy among the four SAT calorimeter modules is > 3.5 GeV, or > 2 GeV if there is a gross counter hit associated with the module. These particular energy values are selected because there is a low background due to electronic noise simulating real energy deposition from particles (see Chapter 4).

Hadronic tau decays such as $\tau^- \rightarrow \nu_\tau \rho^-$ contribute a background through pion punchthrough or through pion decays to muons, where a photon from π^0 decay tags

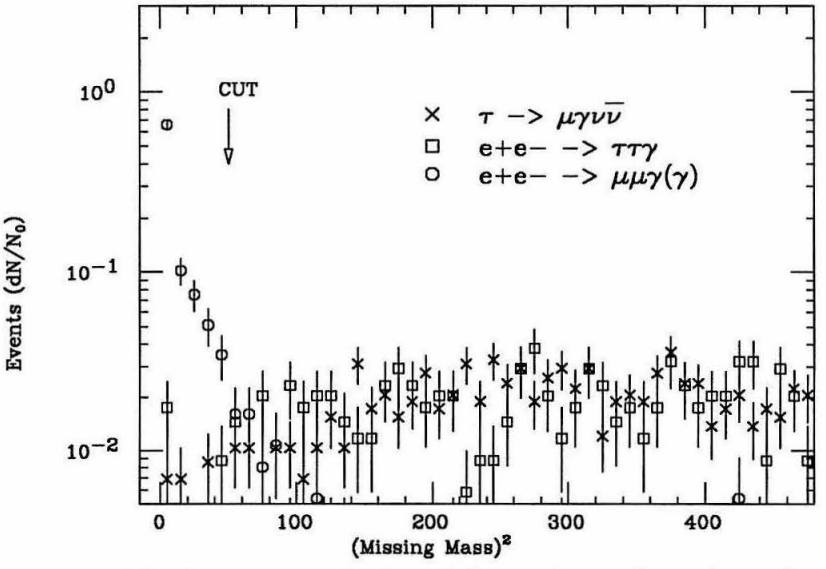

Figure 5.4. Missing mass calculated from charged tracks only supresses radiative mu-pair events. A cut of (missing mass)^2 $>$ 50 is applied to two-charged track events.

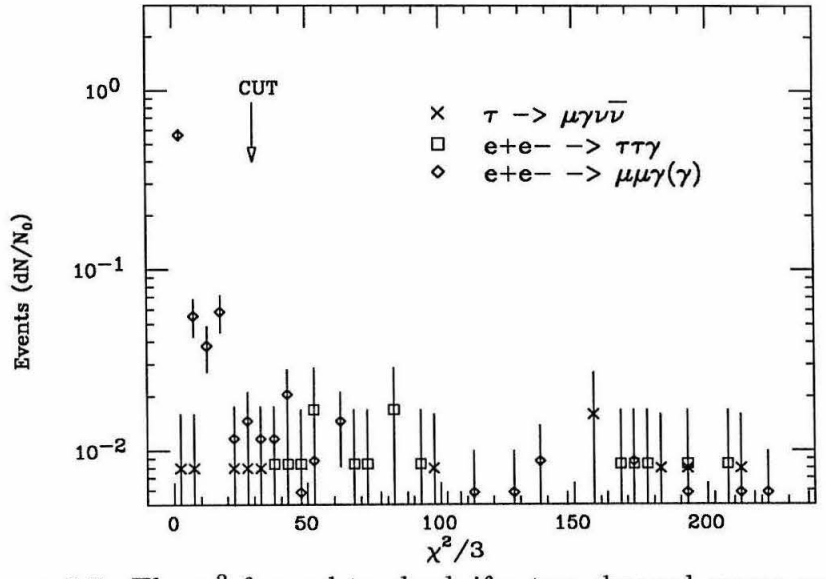

Figure 5.5. The χ^2 formed to check if a two-charged prong event is consistent with being a $e^+e^- \rightarrow \mu^+\mu^-\gamma(\gamma)_{beam}$ event. A cut is made at $\chi^2/3 = 30$ to remove radiative mu-pair background.

the event (and where the other photon goes undetected or where both photons are reconstructed as one). The fairly strict muon definition reduces this background

substantially, but the residual contamination is difficult to remove. Similarly, multi-hadronic events can contribute a background due to hadron decays and punchthrough, accompanied by the presence of nearby photons. This background is very small, however, because of the required isolation of the muon candidate from other charged tracks. Events with > 1 charged tracks in the non-muon hemisphere, having a reconstructed mass > 2.5 GeV are discarded. Another small background comes from cosmic-ray tracks passing near the interaction point. Cosmic-ray events are removed by requiring calorimeter and time–of–flight information for charged tracks and by imposing a TOF cut of < 2.5 ns on the difference between the expected and measured times for both tracks in all 2-charged-track events.

Sixty-seven events survive all the above requirements.

5.4 Estimates of Signal and Background Contributions

Estimates of background contributions and event selection efficiencies are calculated both from Monte Carlo programs and directly from the data. The errors on these estimates arise mostly from the statistics of the data and Monte Carlo samples and from the uncertainties in the assumed branching ratios and cross sections. These errors will later contribute to the estimated systematic errors on measured quantities (*e.g.*, the branching ratio $B(\tau^- \rightarrow \nu_\tau \mu^- \bar{\nu}_\mu \gamma)$) when the μ-γ invariant mass spectrum is fitted with a maximum likelihood technique to determine the contributions from the six sources considered in this analysis. These six sources are the following: radiative tau production ($e^+e^- \rightarrow \tau^+\tau^-\gamma$), radiative tau decay ($\tau^- \rightarrow \nu_\tau \mu^- \bar{\nu}_\mu \gamma$), misidentified hadronic tau decay ($\tau^- \rightarrow \nu_\tau$ (hadrons)$^-$), radiative mu-pairs ($e^+e^- \rightarrow \mu^+\mu^-\gamma(\gamma)$), two-photon processes (*e.g.*, $e^+e^- \rightarrow e^+e^-\mu^+\mu^-\gamma$), and miscellaneous small contributions. The final category includes hadronic events ($e^+e^- \rightarrow q\bar{q} \rightarrow$ X) and backgrounds from spurious electronic noise. Other processes such as higher-order ($\geq \alpha^4$) radiative tau events or muon detector-related

bremsstrahlung are small and neglected here.

A detailed discussion of the procedure for estimating the contributions is given in the Appendix, but a brief summary is given here. For simulating τ-pair production, the Monte Carlo program, KORALB,[17] which includes $O(\alpha)$ initial and final state radiative corrections and accounts for τ mass effects, is used. The multihadronic decays not in KORALB are simulated using the LULEPT [42] Monte Carlo program. The KORALB program is modified to include the radiative decay, $\tau^- \to \nu_\tau \mu^- \bar{\nu}_\mu \gamma$, using formulas originally calculated for the process $\mu \to e\gamma\nu\bar{\nu}$, where the charged-lepton masses are not neglected.[28,27] The expected backgrounds both from τ-pair events and from hadronic events are due to hadrons being misidentified as muons. The total probability of pion decay to muons plus misidentification from punchthrough is measured using pion tracks from $\tau^\pm \to 3\pi^\pm\nu$ and from $\tau^\pm \to \pi^\pm(> 2\gamma)\nu$ to be 0.007 ± 0.002. Using the measured misidentification probability and Monte Carlo simulations, estimates of these backgrounds are obtained. The kinematics of two-photon processes are studied with data and a Monte Carlo program based on the double-equivalent photon approximation.[43] The main two-photon background is from $e^+e^- \to e^+e^-\mu^+\mu^-$ events. Because existing two-photon Monte Carlo generators do not include internal final-state radiation, the $e^+e^- \to e^+e^-\mu^+\mu^-\gamma$ background is estimated directly from the data. The backgrounds from $e^+e^- \to \mu^+\mu^-\gamma$ and $e^+e^- \to \mu^+\mu^-\gamma(\gamma)$ are estimated using a Monte Carlo which allows multiple initial-state and single final-state bremsstrahlung.[44]

Table 5.1 summarizes the expected contributions from signal and background processes. All of the expected number of events shown are after passing the Monte Carlo events through the tau analysis cuts.

5.5 Corrections for Monte Carlo Simulation

Table 5.1. Estimated contributions from signal and background processes, and the uncertainty on the estimates.

Process	Uncertainty in estimated contribution	Estimated Number of Events
$\tau^- \to \nu_\tau \mu^- \bar{\nu}_\mu \gamma$	-	<14
$e^+e^- \to \tau^+\tau^-\gamma$	8%	40.7
misidentified τ	35%	8.9
$e^+e^- \to e^+e^-\mu^+\mu^-\gamma$	45%	3.2
radiative μ-pair	30%	2.6
hadronic+spurious γ	35%	0.2

All Monte Carlo events include a full simulation of the Mark II detector. In addition, estimates from the Monte Carlo are corrected to account for small inaccuracies in the detector simulation and event reconstruction. The largest of these corrections relevant to this analysis is for muon identification efficiency, discussed in Chapter 4. A muon candidate is defined to be a charged particle whose track extrapolation from the drift chamber is aligned with signals in all four layers of the muon system. The difference in efficiency between the data and the Monte Carlo is measured using samples of muons selected from radiative mu-pair and from $e^+e^- \to e^+e^-\mu^+\mu^-$ events. Muon identification is more efficient for the Monte Carlo muons than for data muons by about 2% for tracks with low momentum and by about 9% for higher momentum tracks (see fig. 4.18). Monte Carlo event weights are corrected to account for the discrepancy between the data and Monte Carlo.

The tagging photon in the μ-γ candidate in Monte Carlo events also requires correction for inaccurate simulation of photon shower reconstruction when the muon and photon are very near each other. Using muon tracks from various types of

processes, it was found that the critical separation angle is about 1.8 degrees for resolving the photon shower from the muon's energy deposition. Therefore, Monte Carlo candidate events, where the tagging photon shower lies closer than 1.8 degrees to the muon energy cluster in the calorimeter, are rejected. This causes an estimated 0.8% loss in fully reconstructed Monte Carlo $\tau^- \to \nu_\tau \mu^- \bar{\nu}_\mu \gamma$ events and a negligible loss in other event samples.

A good time–of–flight (TOF) measurement is required of charged tracks to reject cosmic ray backgrounds. The TOF system is also important to this analysis because its inefficiency contributes to the trigger inefficiency for the tau candidate events. The Monte Carlo TOF simulation predicts approximately 100% efficiency for tracks to have TOF information because it does not account for the cracks between TOF counters and the slight loss in detection efficiency near the ends of the counters. Using wide-angle Bhabha events, selected with an independent trigger, based on total electromagnetic shower energy, the TOF efficiency was measured to be $\sim$ 97% for two charged-track events and this correction is applied to all Monte Carlo estimates.[18]

Another small correction accounts for inaccurate modeling of the active region of the SAT (Small Angle Tagger) calorimeter system[35] and the SAT Gross Scintillator Counter[43], both of which are used to reject two-photon and radiative mu-pair backgrounds with electrons or photons emitted at small angles. This correction causes less than a 1% loss in the various Monte Carlo event samples.

5.6 Analysis Results: Radiative Tau Decay

Finally, this section discusses how the branching ratio for radiative tau decay $B(\tau^- \to \nu_\tau \mu^- \bar{\nu}_\mu \gamma)$ and the number of events for radiative tau production $e^+e^- \to \tau^+\tau^-\gamma$ may be derived and compared to theoretically expected values.

The reconstructed mass of the μ-γ candidate is a useful distribution for comparing observation with QED calculations. Each of the predicted event samples has a unique

mass spectrum, allowing extraction of the branching ratio, $B(\tau^- \rightarrow \nu_\tau \mu^- \bar{\nu}_\mu \gamma)$. It is possible to do a simple background subtraction to deduce $B(\tau^- \rightarrow \nu_\tau \mu^- \bar{\nu}_\mu \gamma)$ or to use a likelihood method, both of which yield similar results. A maximum likelihood calculation, using the mass spectrum, is performed to determine the contributions from the six sources considered in this analysis, whose expected contributions are listed in Table 5.1. In the fit, the contribution from radiative τ decay is allowed to vary freely, but the contributions from the other sources (j) are constrained to lie near their predicted values (the ratio of fitted-to-expected contribution $f_j^b = 1$) under the assumption of Gaussian error distributions on those predictions. The likelihood function is defined by

$$L \equiv \left[\prod_j \frac{1}{\sqrt{2\pi}\sigma_j^b} e^{-(f_j^b-1)^2/2\sigma_j^{b\,2}}\right] \times \left[\prod_i \frac{x_i^{n_i} e^{-x_i}}{n_i!}\right] \tag{5.1}$$

where n_i is the number of data points observed in mass bin i, and x_i is the total expected number of events in each bin. The expected number of events is a sum of the backgrounds j, each with uncertainty σ_j^b, (estimated to yield N_{ji} background events in bin i) and of the signal, $\tau^- \rightarrow \nu_\tau \mu^- \bar{\nu}_\mu \gamma$:

$$x_i \equiv 2N_{\tau\tau} B(\tau \rightarrow \mu\gamma\bar{\nu}\nu)\, \epsilon_i^{det} + \sum_j f_j^b N_{ji}.$$

The binned detection efficiency for $\tau^- \rightarrow \nu_\tau \mu^- \bar{\nu}_\mu \gamma$ events is ϵ_i^{det}, and $N_{\tau\tau}$ is the total number of expected tau events for an integrated luminosity[33] of $207.9 \pm 0.5 \pm 2.8$ pb^{-1} and a total cross section, $\sigma(e^+e^- \rightarrow \tau^+\tau^-(\gamma))$, of .135nb. The fit, performed using the MINUIT programs[45], yields the branching ratio $B(\tau^- \rightarrow \nu_\tau \mu^- \bar{\nu}_\mu \gamma)$ and the fitted-to-expected background contribution factors f_j^b's. The expected mass spectra from the four dominant backgrounds are plotted in fig. 5.6, along with their sum. The uncertainties σ_j^b in the predicted background contribution arise mostly from the statistics of the data and of the Monte Carlo samples used to estimate the backgrounds

and from uncertainties in branching ratios and cross sections. Table 5.2 lists the estimated σ_j^b and final fitted f_j^b values, where the $B(\tau^- \to \nu_\tau \mu^- \bar{\nu}_\mu \gamma)$ is divided by its predicted value. Figure 5.7 shows the mass spectrum from the data and from the six predicted contributions, normalized using the fit procedure. In the figure, the mass distribution from the radiative τ decay signal lies mainly below 0.4 GeV. In this low mass region, there are 14 data events; after subtracting the expected background (fig. 5.6), 8.4 ± 3.8 events remain, which is in agreement with the 8.6 ± 3.7 number of signal events predicted by the fit.

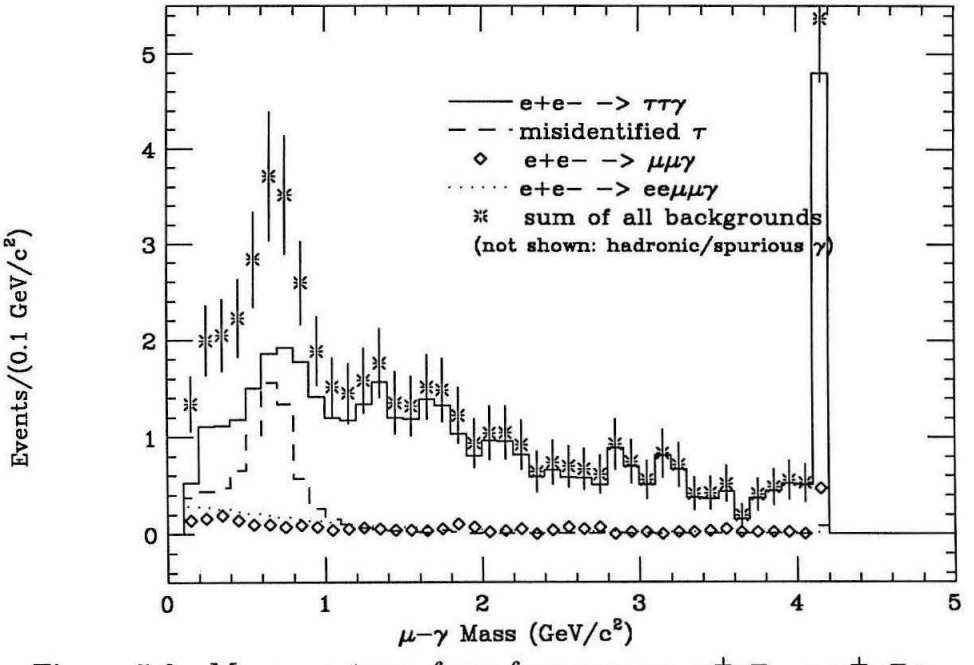

Figure 5.6. Mass spectrum from four sources, $e^+e^- \to \tau^+\tau^-\gamma$, misidentified τ's, $e^+e^- \to e^+e^-\mu^+\mu^-\gamma$, and radiative μ-pairs which are input to the fit. Backgrounds from hadronic events and from spurious electronic noise in the calorimeter are small and not shown. Events are normalized to the Mark II luminosity. (For this and the next several plots, the peak in the last bin is an overflow bin.)

The result for the ratio of fitted to calculated radiative decay branching ratio is 1.03 ± 0.42, where the error is the quadratic sum of the statistical and systematic

Table 5.2. Input parameters and results from the likelihood calculation to extract $B(\tau^- \to \nu_\tau \mu^- \bar{\nu}_\mu \gamma)$ from the μ-γ mass spectrum. The f_j^b's are the ratio of fitted-to-expected contribution, and the σ_j^b's are the uncertainty in each predicted contribution.

Process	Input σ_j^b	Fit Results f_j^b	Fit Results Number of Events
$\tau^- \to \nu_\tau \mu^- \bar{\nu}_\mu \gamma$	–	1.03	10.4
$e^+e^- \to \tau^+\tau^-\gamma$	.08	0.99	40.3
misidentified τ	.35	1.18	10.5
$e^+e^- \to e^+e^-\mu^+\mu^-\gamma$	.45	1.03	3.3
radiative μ-pair	.25	0.99	2.6
hadronic+spurious γ	.35	1.00	0.2

errors. From Monte Carlo studies, about 90% of the radiative decay events passing all event selection criteria arise from decays in which the energy of the photon in the τ rest frame is greater than 0.037 GeV. From this estimate, the ratio of the measured width $\Gamma(\tau^- \to \nu_\tau \mu^- \bar{\nu}_\mu \gamma, E_\gamma > .037$ GeV) to the total width[12] for $\tau^- \to \nu_\tau \mu^- \bar{\nu}_\mu$ is derived to be $1.3 \pm 0.6\%$ (*i.e.*, if $B(\tau^- \to \nu_\tau \mu^- \bar{\nu}_\mu)$ is 17.8%, then $B(\tau^- \to \nu_\tau \mu^- \bar{\nu}_\mu \gamma$, $E_\gamma > .037$ GeV) is $\sim 0.23\%$). A candidate radiative tau decay event from the data is shown in fig. 5.8 where the μ-γ mass is 0.22 GeV.

The fitted-to-expected contribution (the ratio f_j^b) for the last three processes in Table 5.2, deviates from unity by only a small fraction of the uncertainty σ_j^b in the contribution. The fit result for radiative tau decay is not particularly sensitive to these contributions because they are small and the shape of their mass spectrum is different from that of $\tau^- \to \nu_\tau \mu^- \bar{\nu}_\mu \gamma$ events.

Both statistical and systematic errors are included in the estimated error on the

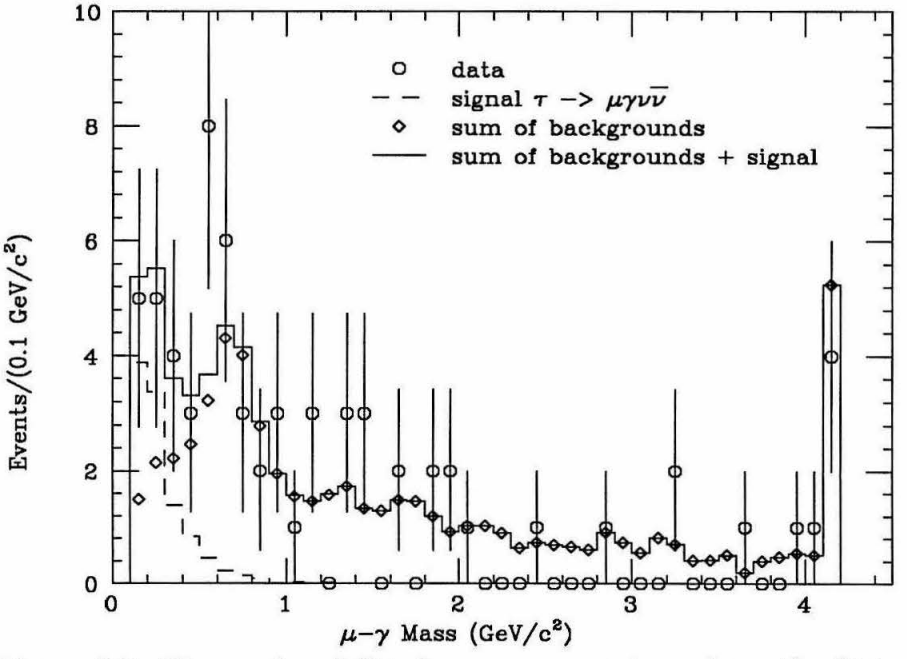

Figure 5.7. Observed and fitted μ-γ mass spectrum from the fit to extract $B(\tau^- \to \nu_\tau \mu^- \bar{\nu}_\mu \gamma)$ described in the text.

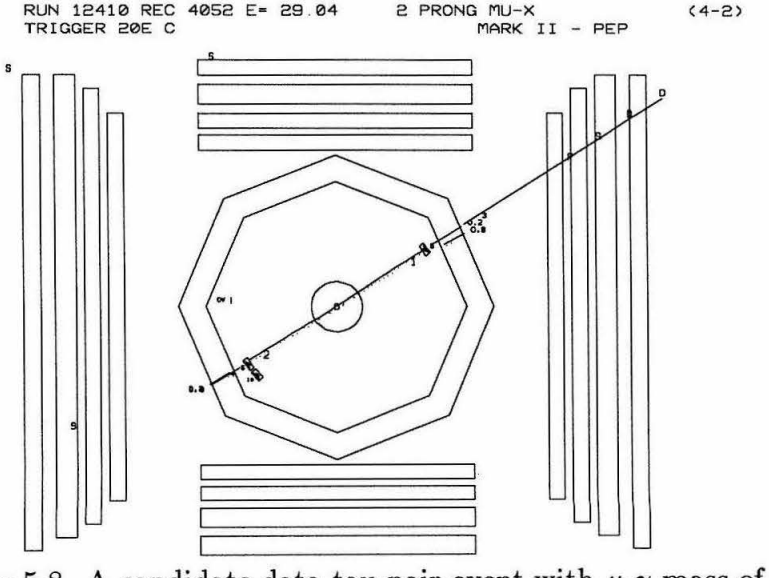

Figure 5.8. A candidate data tau-pair event with μ-γ mass of 0.22 GeV, where track 1 (momentum: 6.8 GeV) is the muon candidate and the photon has a measured energy of 0.8 GeV. This is a muon *vs* pion tau-pair event containing perhaps decay radiation.

measured ratio of partial widths. The statistical part of the error is about 40%, as seen from a subtraction of the number of expected background events from the number of observed events in the .1 – .4 GeV μ-γ mass bins (see fig. 5.7 and fig. 5.6). The fitting program derives a composite error on the fitted branching ratio B($\tau^- \rightarrow \nu_\tau \mu^- \bar{\nu}_\mu \gamma$) that includes both purely statistical and some systematic errors, of which the systematic part is based on the magnitude of the estimated errors σ_j^b on each of the event contributions (see the form of the likelihood function and the Appendix on the method of estimating the σ_j^b's). By varying the individual background levels by one standard deviation, it is possible to check which of the backgrounds contributes most to the systematic error returned by the fit; this turns out to be the misidentified hadronic-tau background ($\sim$ 10% error). This background consists mostly of $\tau^- \rightarrow \nu_\tau \rho^-$ events, where the μ-γ candidate has a reconstructed mass spectrum that peaks just below the rho mass. (Compare fig. 5.6 with the data in fig. 5.7. In a separate analysis, the data is used to check the accuracy of the predicted level of and shape for the μ-γ mass spectrum from misidentified tau events. Figure 5.9 shows good agreement between the data and the Monte Carlo events that pass all the event selection cuts (of section 5.2 and 5.3) where instead of requiring a muon candidate, a pion candidate is required.)

There are other systematic errors (in addition to the error returned by the fitting program) which may be estimated by varying the input parameters in the fit. These include uncertainties in the luminosity measurement (1.4%), in B($\tau^- \rightarrow \nu_\tau \mu^- \bar{\nu}_\mu$) (0.8%), and in the shape of the mass spectrum for the $e^+e^- \rightarrow e^+e^-\mu^+\mu^-\gamma$ background (0.8%, see Appendix section on two-photon background). In the Monte Carlo programs, a library of showers created with the EGS[38] program allows rapid and fairly accurate simulation of electron and photon interactions in the calorimeter. For improved accuracy, it is possible to generate another set of Monte Carlo events using EGS directly instead of the library. Replacing the library-produced $\tau^- \rightarrow \nu_\tau \mu^- \bar{\nu}_\mu \gamma$

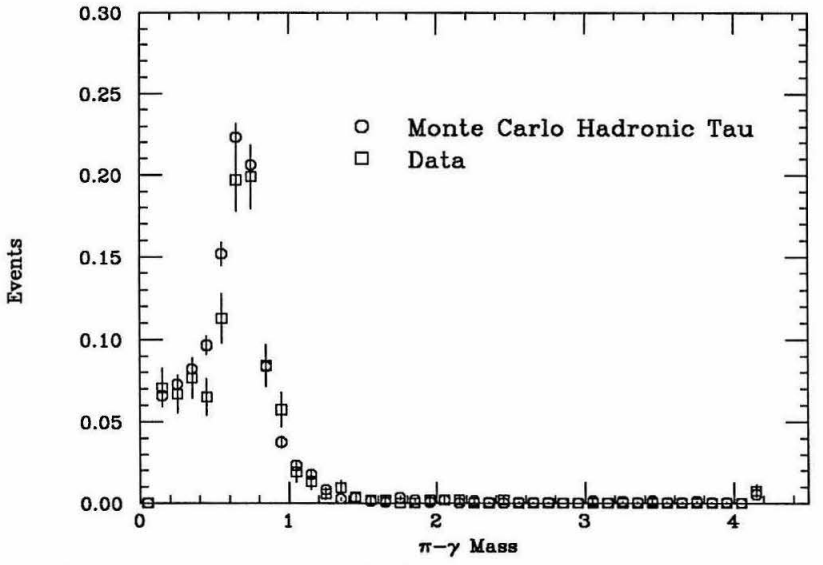

Figure 5.9. Data and Monte Carlo π-γ mass spectrum from $\tau^- \rightarrow \nu_\tau \rho^-$ events, normalized to the same number of events.

events with the EGS-produced ones altered the radiative tau decay branching ratio by 0.5%. A larger source of error comes from the uncertainty in the branching ratios used for the other tau in the Monte Carlo event, which is allowed to decay to all modes (4.5%). (See the radiative tau production section in the Appendix.) Another large source of error (5.5%) is due to uncertainties during event reconstruction: 1) in the apportioning of the calorimeter energy deposited when more than one track hits the same readout strips in a calorimeter module, and 2) in the position of one of the muon walls.

5.6.1 *Radiative Tau production*

To compare radiative τ-pair *production* rate with expectation, the level of $e^+e^- \rightarrow \tau^+\tau^-\gamma$ events is now allowed to vary freely in the likelihood calculation, described in the previous section. The resulting ratio of fitted-to-expected number of events from the radiative production of a τ that decays to a muon and passes event selection criteria is 0.91 ± 0.20, where a branching ratio $\mathrm{B}(\tau^- \rightarrow \nu_\tau \mu^- \bar{\nu}_\mu)$ value of 17.8% and

a tau production cross section of .135nb are used. A candidate event from the data is shown in fig. 5.10 where the μ-γ mass is 1.65 GeV. Systematic errors are similar to those described above for the radiative tau decay branching ratio and are included in the error. Overall, the ratio of radiative events with a single hard initial or final state photon (energy $>$ .3 GeV and $|\cos\theta| <$ .70 and within 90° of the muon) to all $O(\alpha^3)$ events (with or without a photon) is $\sim$ 3.5%, of which $\sim$ 62% are from final state radiation. These results are based on a Monte Carlo study at the four-vector level, where a muon track of momentum $>$ 2 GeV is required within $|\cos\theta| <$ .45. Tau-pair production with visible final-state bremsstrahlung is non-negligible.

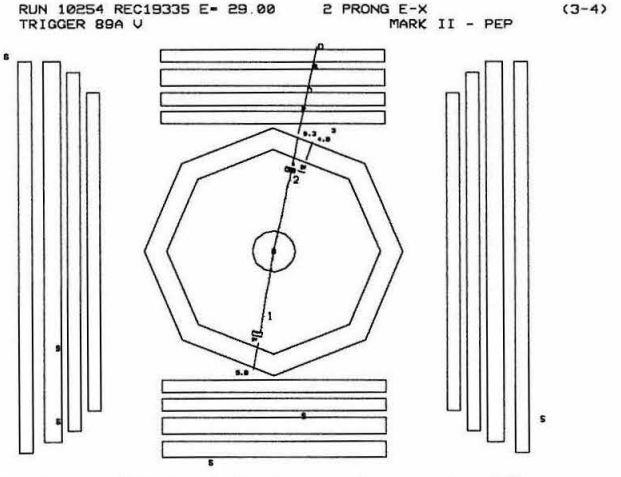

Figure 5.10. A candidate data tau-pair event with μ-γ mass of 1.65 GeV, where track 2 (momentum: 4.3 GeV) is the muon candidate and the photon has a measured energy of 4.6 GeV. This is most likely an electron *vs* muon tau-pair event containing initial-state or final-state radiation.

Other experimental distributions confirm the agreement between the data and predictions. For example, fig. 5.11 shows the observed photon energy spectrum in comparison with the expected distribution obtained from the fit to the μ-γ mass spectrum.

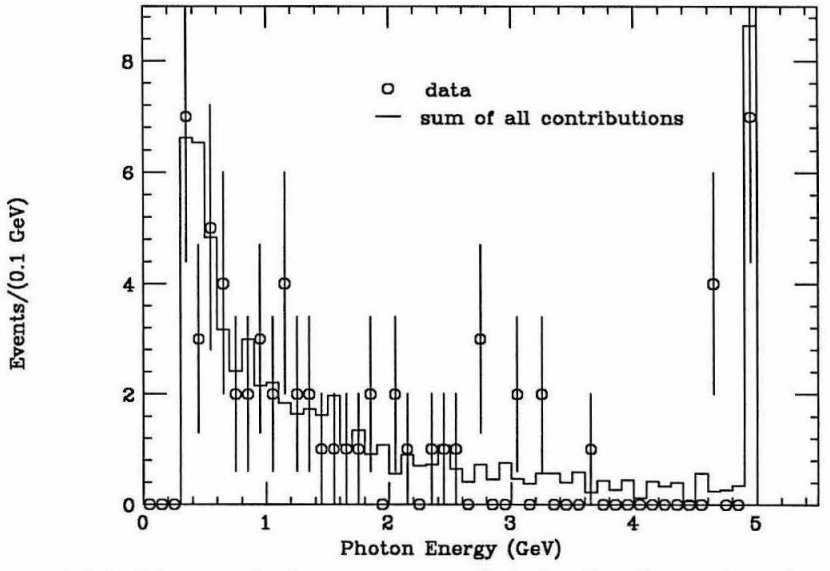

Figure 5.11. Measured photon energy distribution from the selected μ-γ event sample. The sum of the distributions from all predicted sources listed in Table 5.2, normalized using the results of the fit to the μ-γ mass spectrum, is also shown.

5.7 Cross-checks on Results

It is necessary to check the analysis results, particularly to test whether the data require the measured branching ratio for radiative tau decay ($\tau^- \rightarrow \nu_\tau \mu^- \bar{\nu}_\mu \gamma$) to really be non-zero. This check is important because of the large error on the branching ratio measurement due to poor statistics (see fig. 5.7). Several precautions are taken prior to addressing this issue. As mentioned above, the fit results agree well with the results obtained from a simple background subtraction in the μ-γ mass region <0.4 GeV, and this partly checks the fitting procedure. All of the final data events are hand-scanned to ensure that there are no "surprises," such as from detector-related problems. Because radiative tau decay events ($\tau^- \rightarrow \nu_\tau \mu^- \bar{\nu}_\mu \gamma$) are expected to produce a photon very near the muon, it is helpful to examine a variable returned by the calorimeter cluster algorithm which gives a measure of the degree of energy sharing between the two clusters found for the muon and for the photon. The proximity of the muon to the photon and the strip geometry of the calorimeter may cause the

two particles to deposit energy on the same strip in a particular calorimeter layer. The cluster finding algorithm will apportion the energy in the shared strips according to the relative energies deposited by the two particles in the non-shared strips, and return a non-zero value of the variable to indicate sharing. Excessive sharing suggests that the reconstructed photon cluster may actually be the energy deposited by the muon track and not due to the presence of a genuine photon. The μ-γ candidates for radiative tau decay generally have μ-γ mass $< .4$ GeV and the sharing for all of the photon candidates in this mass range turn out to be less than 21%, with 5.2% being the average. Therefore, it is likely that the photons found by the cluster algorithm are indeed separate entities from the muon energy deposition.

Finally, a check is made to determine whether the data require the measured branching ratio for radiative tau decay ($B(\tau^- \rightarrow \nu_\tau \mu^- \bar{\nu}_\mu \gamma)$) to be non-zero. The likelihood-ratio test is a useful method for comparing the null hypothesis H_0 against an alternative hypothesis H_1. Here, H_0 is the hypothesis that the data does not require radiative tau decay and $B(\tau^- \rightarrow \nu_\tau \mu^- \bar{\nu}_\mu \gamma)$ is zero, while H_1 is the non-zero situation. For H_1, the likelihood fit is performed as usual; for H_0, the likelihood fit is repeated after setting $B(\tau^- \rightarrow \nu_\tau \mu^- \bar{\nu}_\mu \gamma)$ to zero in eqn. 5.1. The ratio, λ, of the two likelihood values is defined as

$$\lambda \equiv \frac{L(H_0)}{L(H_1)}$$

and ranges between zero and one, where one indicates there is a large probability of H_0 being true. For the radiative tau decay analysis, the likelihood values give a λ of .0107 which can be transformed into a probability value by using the correspondence[46]

$$-2 \ln \lambda \rightarrow \chi^2(\text{one degree of freedom}).$$

Here, the χ^2 value is ~ 9.08; the probability of the null hypothesis being true is small ($\sim 0.26\%$). The correspondence is strictly true only for Gaussian forms of a likelihood

function, which is not true of the likelihood function used here (eqn. 5.1). However, the distribution of eqn. 5.1 for various values of the $\tau^- \to \nu_\tau \mu^- \bar{\nu}_\mu \gamma$ branching ratio clearly favors a non-zero value for the branching ratio (see fig. 5.12). Therefore, the data *do* require a non-zero branching ratio for $B(\tau^- \to \nu_\tau \mu^- \bar{\nu}_\mu \gamma)$.

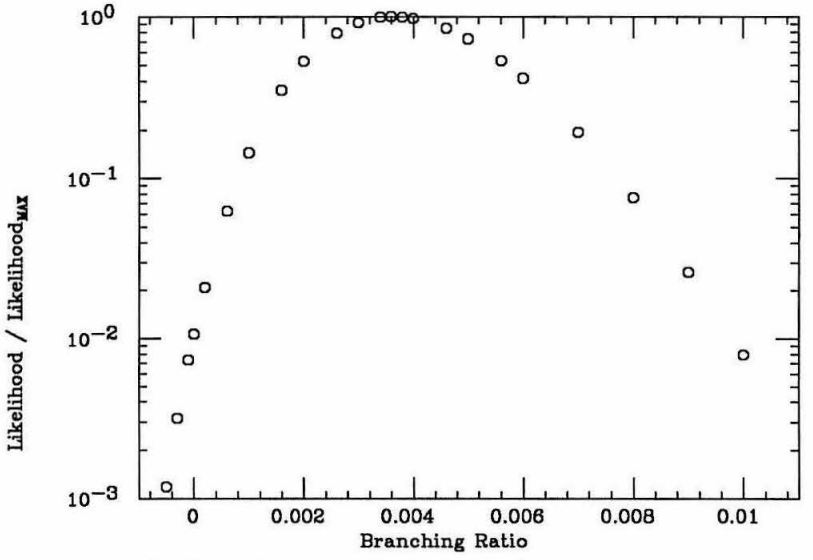

Figure 5.12. The likelihood function vs $B(\tau^- \to \nu_\tau \mu^- \bar{\nu}_\mu \gamma)$, where the fit is repeated at each fixed value of $B(\tau^- \to \nu_\tau \mu^- \bar{\nu}_\mu \gamma)$ with the other parameters allowed to vary.

Chapter 6

Discussion

6.1 Summary of Results

In summary, the QED process radiative τ decay, $\tau^- \rightarrow \nu_\tau \mu^- \bar{\nu}_\mu \gamma$, has been observed in the Mark II data with a ratio of measured-to-calculated rate of 1.03 ± 0.42. The ratio of the measured width $\Gamma(\tau^- \rightarrow \nu_\tau \mu^- \bar{\nu}_\mu \gamma, E_\gamma > .037$ GeV) to the total width[12] for $\tau^- \rightarrow \nu_\tau \mu^- \bar{\nu}_\mu$ is $1.3 \pm 0.6\%$, giving a branching ratio of about 0.2% for $\tau^- \rightarrow \nu_\tau \mu^- \bar{\nu}_\mu \gamma$ for photons with $> .037$ GeV energy in the tau rest frame. The ratio of measured-to-predicted number of events from radiative τ production, $e^+e^- \rightarrow \tau^+\tau^-\gamma$, where one of the τ's decay to $\mu\nu\bar{\nu}$ is found to be 0.91 ± 0.20. Radiative corrections for tau pair production are non-negligible and must be considered carefully in tau analysis. Because detectors at e^+e^- annihilation experiments usually cover the large-angle region rather than the small angle, detected radiative events often result from final-state radiation rather than initial-state radiation. Finally, for the tau analysis reported in this thesis, there is no indication of anomalous behavior in radiative events.

6.1.1 Radiative Tau Decay at Other Energies

It is interesting to see how important radiative tau decay would be at other e^+e^- collision energies. Table 6.1 lists for various beam energies, the fraction of

Table 6.1. Radiative tau decay $\tau^- \rightarrow \nu_\tau \mu^- \bar{\nu}_\mu \gamma$ at other center-of-mass energies for e^+e^- experiments. For each energy, the individual probability of having a muon with momentum > 2 GeV, a photon with energy > 0.3 GeV, and a μ-γ opening angle > 5.7°, and the total probability of requiring all three conditions are given.

Beam energy	Muon p> 2.0GeV	Photon E> 0.3GeV	Angle> 5.7°	Total
5.0 GeV	0.19	0.41	0.85	0.08
	(0.40 p> 4.0GeV	(0.57 E> 0.2GeV)		(0.19)
14.5 GeV	0.69	0.53	0.51	0.12
45.5 GeV	0.90	0.63	0.18	0.04

$\tau^- \rightarrow \nu_\tau \mu^- \bar{\nu}_\mu \gamma$ events with photon energy above 0.3 GeV, muon momentum above 2.0 GeV, and with μ-γ angles > 5.7°.

At higher center-of-mass energies, such as 91 GeV, the decay width of the Z^0 to tau pairs is about 4% of the total visible width. This year, individual experiments at LEP should obtain $\sim$ 1.5 million detected Z events, yielding 60,000 tau pairs, over double the number produced at Mark II/PEP. The calorimeters at the LEP experiments generally define photon clusters not coming from electronic noise to be energies above $\sim$ 100 MeV. For photons above 300 MeV, an individual experiment should have about 13 $\tau^- \rightarrow \nu_\tau \mu^- \bar{\nu}_\mu \gamma$ events (the muon system coverage is larger which compensates for the reduced probability of detecting such events from the smaller μ-γ opening angle).

There are many more detectable radiative decay events at lower energies (*e.g.*, at CLEO-II with center-mass-energy $\sim$ 10 GeV). There is less Lorentz boost so that the lab frame energy of the muon and the photon is smaller, but the opening angle between them is larger. The largest factor in the increase of all type of tau events at lower energies is from the increase in cross section; for example, the $O(\alpha^3)$ tau-

pair production cross section at E_{cm} = 29 GeV is 0.135 nb, but is 1.01 nb at E_{cm} = 10 GeV, a 7.5-fold increase! CLEO-II is expected to have over double the total Mark II luminosity after only one year of running; its muon solid-angle coverage is also approximately double and its finely segmented electromagnetic calorimeter of cesium iodide crystals has little background from electronic noise for detecting photons of $>$ 100 MeV energy.[47] For photons above 300 MeV, after one year of running, CLEO-II should have about 20 times more $\tau^- \rightarrow \nu_\tau \mu^- \bar{\nu}_\mu \gamma$ events than the 10 events extracted from the data here. (A more conservative estimate in the level of increase of number of events may be required, however. The decay products of the other tau may be of too low energy to pass event requirements, etc.) It is also much easier for CLEO-II to detect decay radiation from other tau decay modes because of the larger opening angle between the photon and the charged tagged particle.

The issues considered in this thesis analysis should prove useful to those in the future who study radiative tau events, possible anomalous sources of photons, and the one charged-prong tau discrepancy.

Appendix A

Appendix

A.1 Decay Channels in the Tau-Pair Monte Carlo

KORALB[17] is the main tau-pair Monte Carlo program used in this thesis analysis to estimate the detection efficiency of tau events. The decay channels available in KORALB are all the leptonic tau decay modes and the major hadronic ones: π^-, ρ^-, and a_1^-. Simulations of missing hadronic decay modes, particularly those containing multiple π^0's along with charged hadrons, are handled by incorporating into KORALB simulations of the missing modes from another tau-pair generator, the LULEPT-LUND[42] Monte Carlo. Because the efficiencies for detecting signal events in the 1 vs 1 and 1 vs 3 tau-pair topologies differ by about 20%, it is important that the Monte Carlo reproduces the experimentally-measured topological branching ratios. One complication is the one-prong discrepancy (see the Introduction Chapter) between the inclusive and exclusive branching measurements, since the unknown, missing modes cannot be simulated. The approach taken here is to check that the sum of the individual branching ratios B_i in the Monte Carlo program agrees with the experimentally found topological ratios, $B_1 : B_3 : B_5 = 86.6 : 13.3 : 0.1$. A correction factor is then applied to derived efficiencies for the over-estimated branching ratios. The branching ratio values selected for KORALB listed in Table A.1 are based on a recent Mark II tau branching ratio analysis.[48] In that work, a simulta-

neous fit was performed on a sample of unbiased tau decays which were categorized into e,$\mu, \pi, \pi\pi^0$... modes, where the sum of the branching ratios was constrained to be one.

Table A.1. The following τ branching ratios are used in the tau-pair Monte Carlo, KORALB. Values are based on ref. 48.

Decay	B.R.(%)
$\tau^- \rightarrow \nu_\tau \, e^- \, \bar{\nu}_e$	19.1
$\tau^- \rightarrow \nu_\tau \, \mu^- \, \bar{\nu}_\mu$	18.6
$\tau^- \rightarrow \nu_\tau \, \pi^-$	11.4
$\tau^- \rightarrow \nu_\tau \, \rho^-$	25.6
$\tau^- \rightarrow \nu_\tau \, K^-$	0.7
$\tau^- \rightarrow \nu_\tau \, K^{*-}$	1.3
$\tau^- \rightarrow \nu_\tau \, a_1^-$	13.0
$\tau^- \rightarrow \nu_\tau \, \bar{u}d$	10.2

A.2 Details of Signal and Background Contribution Estimates

The following sections contain a detailed discussion of the procedure for estimating the signal and background contributions and the uncertainty on these estimates.

A.2.1 Radiative Tau-Pair Production

The tau-pair Monte Carlo, KORALB,[17] used to estimate the selection efficiency for tau events simulates the process $e^+e^- \rightarrow \tau^+\tau^-(\gamma)$, where a real photon may be emitted from the initial state e^-/e^+ or from the final state τ^-/τ^+. Tau-pair events were generated where one tau decays to $\nu \, \mu \, \bar{\nu}$ and the other tau to all modes listed in Table A.1.

With a $\tau^- \rightarrow \nu_\tau \, \mu^- \, \bar{\nu}_\mu$ branching ratio of (17.8±.4)% [13], a total tau-pair production cross section of $\sigma(e^+e^- \rightarrow \tau^+\tau^-(\gamma)) = 135$ pb, and a total integrated luminosity

of $(207.9 \pm .5 \pm 2.8\ \text{pb}^{-1})$[35,33], the total number of muonic tau decays expected in the data is 9992 ± 263. After passing the Monte Carlo events through the selection criteria, an estimated 40.7 events are expected to be detected. Table A.2 lists the event cuts where most of the detection inefficiencies occurs. There are two major inefficiencies: 1) incomplete muon detector coverage, the $(1 + \cos^2\theta)$ tau-pair polar angle distribution combined with 2) the requirement that candidate muons have momentum above 2 GeV.

Table A.2. The selection criteria where most of the $e^+e^- \to \tau^+\tau^-\gamma$, with a decay to the inclusive muon mode, events are removed. The first number is the percent of events which survive, relative to the total number of Monte Carlo events generated. Since other event criteria are applied, such as total energy requirements, between the ones listed below, I give a second number showing the effect of the cut alone, the ratio of events before and after the cut.

$e^+e^- \to \tau^+\tau^-\gamma$		
	Events remaining with respect to	
Description of Cut	total number generated	number prior to cut
2–6 charge tracks	76%	76%
1 muon candidate	23%	30%
1 photon candidate within 90° of muon	0.63%	2.9%

The main sources of error in the efficiency estimates come from the uncertainties in the luminosity (1.4%), in the $\tau^- \to \nu_\tau \mu^- \bar{\nu}_\mu$ branching ratio (2.2%), in the photon detection efficiency (3.0%), in the muon identification efficiency (5.0%), and the statistics of the Monte Carlo (3.2%) and the uncertainty in the branching ratios used for the other tau in the Monte Carlo event which is allowed to decay to all modes (4.5%). The last error is estimated by using Monte Carlo events generated

with a different set of of tau decay branching ratios (though all are scaled higher to compensate for the one-prong discrepancy) that are more consistent with the values provided by the Particle Data Group[13]. The various errors give a total uncertainty of $\sim 8\%$ on the radiative tau production contribution.

In addition to estimating the contribution from $O(\alpha^3)$ QED radiative tau production, it is necessary to check if higher order processes contribute as well. This is done using the KORALZ3[44] Monte Carlo which includes contributions from soft photons summed rigorously up to infinite order as well as contributions from multiple hard photons. Multiple QED hard photon emission is permitted from the initial state and single-photon emission from the final state. Therefore, KORALZ3 is useful for estimating events from higher order QED processes such as $e^+e^- \rightarrow \tau^+\tau^-\gamma_{final\ state}(\gamma)_{initial\ state}$, which turn out to have negligible contributions.

A.2.2 Radiative Tau Decay

The expected contribution from radiative tau decay events is also estimated with the tau Monte Carlo, KORALB, where the radiative decay mode, $\nu\,\mu\,\bar{\nu}\gamma$, is incorporated as described in Chapter 3. In order to extract the branching ratio $B(\tau^- \rightarrow \nu_\tau\,\mu^-\,\bar{\nu}_\mu\gamma)$, it is necessary to estimate the efficiency for detecting this decay channel. Including full detector simulation, twenty thousand Monte Carlo tau-pair events are generated with one tau decaying to $\nu\,\mu\,\bar{\nu}\gamma$ and the other tau decaying to all modes (described above). After passing the events through all the selection and background-rejection criteria discussed earlier, about 5.1% of the events remain. Table A.3 shows that the cuts where most events are rejected are very similar to the case for radiative tau production.

A.2.3 Misidentified Tau Processes

Misidentified hadronic tau decays result from the detection of muons from hadron decays or the detection of hadrons which punch through the muon system, combined

Table A.3. The event selection criteria where most of the $\tau^- \to \nu_\tau \mu^- \bar{\nu}_\mu \gamma$ signal is lost. For an explanation of the percentages shown, see Table A.2.

$e^+e^- \to \tau^+\tau^-$, $\tau^- \to \nu_\tau \mu^- \bar{\nu}_\mu$		
	Events remaining with respect to	
Description of Cut	total number generated	number prior to cut
2–6 charge tracks	76%	76%
1 muon candiate	21%	27%
1 photon candiate within 90° of muon	7.5%	40%

with the presence of a photon from QED processes or from pi-zero decay. Because the branching ratio for tau decay to kaons is very small ($\sim$ 2% level), most of the misidentified tau background comes from the decays to the charged-ρ mode.

The total probability of pion decay plus punchthrough is measured in a study separate from the radiative tau analysis, using 1054 pion tracks from $\tau^\pm \to 3\pi^\pm\nu$ and 960 from $\tau^\pm \to \pi^\pm(> 2\gamma)\nu$ to be 0.007 ± 0.002, where the error is mostly statistical. The pion sample is required to pass the same momentum ($\geq$ 2 GeV) and acceptance criteria as those in the event selection and the sample has $\ll$ 1% contamination. Pions decay to muons in distance d with a probablity

$$P(d) = 1 - e^{-d/\gamma\beta c\tau} = 1 - e^{-md/p\tau}$$

which depends on the mass m, lifetime τ, and momentum p of the pion. Therefore, the probability of pion decay decreases with higher momenta. Pion punchthrough, on the other hand, has a probability that increases with momentum. It turns out the total probability (decay plus punchthrough) is insensitive to momentum. For example, in ref. 40, where the two processes are estimated separately, the sum of the two probabilities for different momenta is reasonably constant. (See Table A.4,

where the probabilities shown are based on a narrower search region for hits around the projected drift chamber track into the muon system than the one used in this thesis. See Chapter 4; these probabilities are estimated from hadronic data and Monte Carlo.)

Table A.4. An example of pion decay and punchthrough probabilities measurement from ref. 40, where the error on the punchthrough values is about 40% and on decay about 20%. The sum of the two probabilities is fairly constant for different momenta.

Momentum	Punchthrough	Decay	Sum
2 - 2.5 GeV	.0022	.0035	.0057± .0011
2.5 - 3 GeV	.0024	.0040	.0064± .0012
3 - 3.5 GeV	.0025	.0041	.0066± .0013
3.5 - 4 GeV	.0027	.0039	.0066± .0013
4 - 4.5 GeV	.0028	.0038	.0066± .0014
4.5 - 5 GeV	.0030	.0037	.0067± .0014
5 - 5.5 GeV	.0032	.0034	.0066± .0015
5.5 - 6 GeV	.0036	.0030	.0066± .0016
$\geq$ 6 GeV	.0043	.0020	.0065± .0018

Monte Carlo tau-pair events, with one tau decaying only to hadronic modes and the other tau to all modes, are used to estimate the background from misidentified tau events. The branching ratios used for the hadronic modes are based on the Particle Data Group[13] values, with $\sim$ 23% for the major contribution that is from the $\tau^- \rightarrow \nu_\tau \rho^-$ mode ($\sim$ 39% for the $\tau^- \rightarrow \nu_\tau$ (hadrons)$^-(\geq 1\pi^0)$ mode). The number of charged hadronic decays passing all event selection criteria (except the muon-detector hits requirement) is multiplied by the total misidentification probability to give the

contribution from misidentified hadrons, expected to be 8.9 events (statistical error less than 1%).

This estimate has a systematic error due to the low statistics in the measurement of the pion decay and punchthrough probability ($\sim$ 30%) and due to the uncertainty in the hadronic branching ratios of the tau. Most of the misidentified hadronic tau decays are due to the $\pi^{\pm}\pi^0$ combination. The Particle Data Group[13] tau branching ratio for the rho mode has a 5% error (22.3±1.1)%. To be conservative, a larger uncertainty which takes into account the uncertainty in other hadronic tau decay modes is instead used (*i.e.*, the $\tau^- \rightarrow \nu_\tau$ (hadrons)$^-$($\geq$ 0 neutrals) branching ratio with a $\sim$ 15% uncertainty is used).*

Another source of systematic error that needs to be considered is the accuracy of the Monte Carlo simulation of the detection of single *vs* double photons from pi-zero decay, $\pi^0 \rightarrow \gamma\gamma$. Only the cases where the two photons are emitted very closely and detected as one merged photon or where one photon goes undetected (*e.g.*, passed through the calorimeter gaps) would fake the conditions required by the event selection criteria. The Monte Carlo simulation of the calorimeter used throughout this analysis is the same as that used in a Mark II measurement of the $\tau^- \rightarrow \nu_\tau \rho^-$ branching ratio[49], where the detection efficiency for single vs double photons is an issue. That $\tau^- \rightarrow \nu_\tau \rho^-$ measurement yielded a branching ratio value of $(22.3 \pm 0.6 \pm 1.4)\%$ with a total uncertainty of 7%, which is used here to assign an estimated 10% uncertainty in the modeling of pi-zero detection (also see discussion for fig. 5.9) and is now summed in quadrature with the other two systematic uncertainties. In summary, the misidentified hadronic tau contribution is estimated to be 8.9 ± 3.1 events.

---

* The Particle Data Group finds a fitted value of (50.3±.6)% and an average value of (49±7)%. The uncertainty on the second value is used.

A.2.4 Radiative Mu-Pair Processes

The small background from radiative mu-pair events is estimated with the KORALZ3 Monte Carlo, described in section A.3.1, which includes multiple initial state and single final state bremsstrahlung. An estimated 2.6±0.3 (statistical error) Monte Carlo events survive the event selection criteria, and Table A.5 shows that the total energy cut is very effective in removing this background, particularly for the $O(\alpha^3)$ QED $e^+e^- \rightarrow \mu^+\mu^-\gamma$ process. For removing higher order (*e.g.*, $O(\alpha^4)$) QED processes such as $e^+e^- \rightarrow \mu^+\mu^-\gamma(\gamma)_{beam}$ background where initial state hard bremsstrahlung is primarily near the beam direction and goes undetected, requiring energy balance along the beam direction and/or missing mass cuts are more effective.

Table A.5. The selection criteria where most of the $O(\alpha^3)$ and $O(\alpha^4)$ mu-pair production backgrounds are removed. For an explanation of the percentages shown, see Table A.3.

$e^+e^- \rightarrow \mu^+\mu^-\gamma(\gamma)$		
	Events remaining with respect to	
Description of Cut	total number generated	number prior to cut
1 muon candiate	26%	-
total energy <24GeV	3.7%	15%
1 photon candiate within 90° of muon	.2%	6.9%
energy balance along beam direction	.05%	28%
missing mass and kinematic constraints	.015%	33%

Order (α^3) QED Monte Carlo calculations from KORALB predict less than .5 events background contribution from the $O(\alpha^3)$ $e^+e^- \rightarrow \mu^+\mu^-\gamma$ process. Therefore,

most of the 2.6 events from radiative mu-pair background comes from yet-higher order QED processes like $e^+e^- \rightarrow \mu^+\mu^-\gamma(\gamma)$ estimated using the algorithm of the other tau Monte Carlo, KORALZ3. As shown in fig. A.1, KORALZ3 reproduces the observed shapes of kinematic variables such as the photon energy, aplanarity and mass spectra, for $e^+e^- \rightarrow \mu^+\mu^-\gamma(\gamma)_{\rm beam}$ events selected by requiring two muons and good χ^2 from a kinematic constraint for the $e^+e^- \rightarrow \mu^+\mu^-\gamma(\gamma)_{beam}$ configuration where the undetected photon must lie along the beam axis (see tau analysis background rejection cuts in Chapter 5).

Systematic errors on the estimate of the $O(\geq \alpha^3)$ radiative mu-pair contribution are difficult to assess partly because $O(\geq \alpha^4)$ QED processes are rarely measured and only recently included in "standard" Monte Carlo programs. One source of uncertainty is the effectiveness of the kinematic cuts used to reject radiative mu-pairs, cuts selected and tuned based on the kinematics of the Monte Carlo KORALB ($e^+e^- \rightarrow \mu^+\mu^-\gamma$) and KORALZ3 events. The kinematic-constraint cuts used in the tau analysis require an accurate Monte Carlo simulation of several detector resolutions and an accurate measurement of several quantities (*i.e.*, accurate momentum, energy and position measurements). The tendency is for the Monte Carlo simulation of detector resolutions to be better than actual.

A large sample of radiative mu-pair events is needed to study the possible Monte Carlo resolution simulation inaccuracy. In a separate analysis, such a sample of events is selected from the data (442 events) by requiring 1) two well-identified muons, 2) one photon with energy > 0.3 GeV, and 3) total visible energy of the event to be greater than 12 GeV (this is to reject two-photon $e^+e^- \rightarrow e^+e^-\mu^+\mu^-\gamma$ events). A χ^2 variable is formed from the measured and predicted momentum of the two charged and photon tracks, and the errors on the measured values. This is the same kinematic constraint where a $\frac{\chi^2}{3} > 30$ is used to reject $e^+e^- \rightarrow \mu^+\mu^-\gamma(\gamma)_{beam}$ events in the tau analysis (see Chapter 5; the calculated momentum for the two muons and the

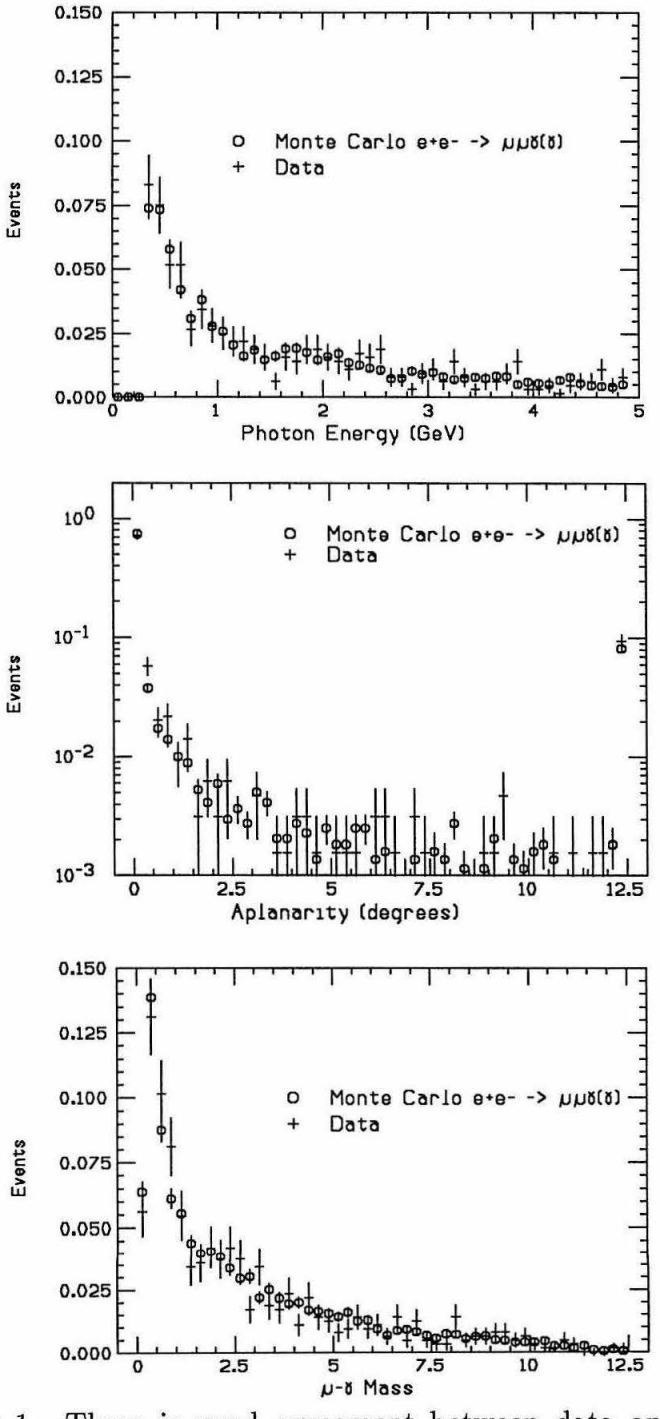

Figure A.1. There is good agreement between data and Monte Carlo in the shapes of the spectra for the detected photon energy, for the aplanarity (360 degrees – sum of angles between the 3 detected tracks), and for the μ-γ mass.

calculated energy for the photon are obtained from a kinematic constraint for the $e^+e^- \rightarrow \mu^+\mu^-\gamma(\gamma)_{beam}$ configuration where the undetected photon must lie along the beam axis). There is a background of $\sim$ 2 events from taus, both having high χ^2 values. This small background is subtracted from the observed number of events; the data for high values of χ^2 is not significantly biased by a non-radiative-mu-pair background. After correction for known detector and measurement inefficiencies in the Monte Carlo (*e.g.*, muon identification efficiency is higher for the Monte Carlo than for the data), the total number of observed events is lower than that predicted by the KORALZ3 Monte Carlo by $\sim$ 15% over the entire range of χ^2 values. However, for large values of χ^2 ($\frac{\chi^2}{3} > 30$), the data (24 events) contains $\sim$ 25% more events than predicted by KORALZ3 (19 events). The smaller average value of the χ^2 for the Monte Carlo events is attributed to a somewhat over-optimistic simulation of the detector resolutions. Because of the limited statistics in the high χ^2 region, and of the difference in event selection criteria for this radiative mu-pair sample vs the tau analysis sample, the prediction of 2.6 radiative mu-pair background in the tau analysis is not re-scaled. Instead, the $\sim$ 25% difference is used as an estimate of the uncertainty in the efficiency of the background rejection cuts (*e.g.*, the χ^2 cut) devised to remove higher order radiative mu-pair events. Together with the statistical error ($\sim$ 10%), the total uncertainty in the estimated 2.6 event contribution is about 30%, giving $2.6 \pm .8$ events.

A.2.5 Two-Photon Processes

Two-photon events such as $e^+e^- \rightarrow e^+e^-\mu^+\mu^-$ are $O(\alpha^4)$ QED processes (see fig. A.2) with large total cross sections ($>$ 100 nb for $e^+e^- \rightarrow e^+e^-\mu^+\mu^-$ at $E_{cm} = 29$ GeV), due mainly to the multiperipheral diagram (a) in fig. A.2. Because of low total visible energy, most of these events produced will not pass the tau event selection criteria; however, two photon events would still be an intolerable background if not

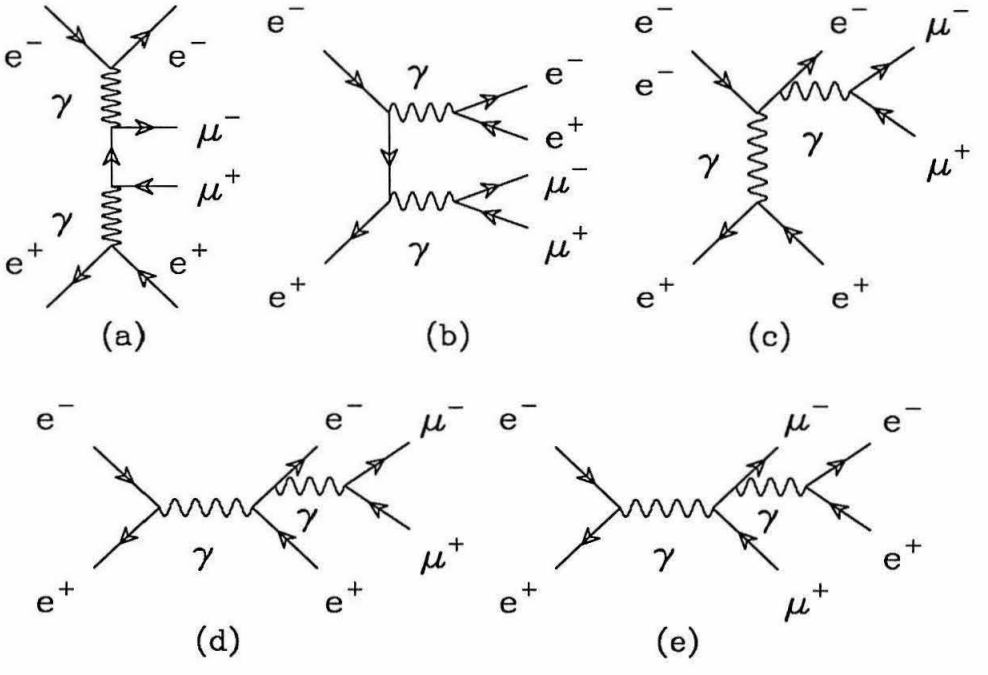

Figure A.2. Examples of Feynman diagrams for the production of an electron and muon pair, (a) multiperipheral, (b) conversion, (c) bremsstrahlung and (d–e) annihilation.

for the additional suppression due to the requirement of detectable bremsstrahlung at wide angles.

There are several major two-photon processes having event characteristics which can pass the tau analysis selection cuts, including $e^+e^- \to e^+e^-\pi^+\pi^-\gamma$, $e^+e^- \to e^+e^-\rho^+\rho^-(\rho^\pm \to \pi^\pm\pi^0)$, $e^+e^- \to e^+e^-\tau^+\tau^-(\gamma)$ and $e^+e^- \to e^+e^-\mu^+\mu^-\gamma$. The first two are a background when a charged pion track decays to a muon or punches through the muon detector. After the total energy requirements (see Chapter 5), the remaining two-photon background is small, and because the pion punchthrough and decay probability is less than 1% (see the section on the misidentified tau contribution), the $e^+e^- \to e^+e^-\pi^+\pi^-\gamma$ and $e^+e^- \to e^+e^-\rho^+\rho^-$ backgrounds turn out to be negligible.

The backgrounds from $e^+e^- \rightarrow e^+e^-\mu^+\mu^-\gamma$ and $e^+e^- \rightarrow e^+e^-\tau^+\tau^-(\gamma)$ are estimated using the Monte Carlo GGDEPA[43], which is based on the double equivalent photon approximation (which relates the cross section for two-photon process $e^+e^- \rightarrow e^+e^-X$ to that of $\gamma\gamma \rightarrow X$).[50] Because GGDEPA and other existing two-photon Monte Carlos don't include internal final-state radiation, it is necessary first to estimate from the data the relative rates of radiative to non-radiative two-photon events. The ratio

$$\frac{e^+e^- \rightarrow e^+e^-\mu^+\mu^-\gamma}{e^+e^- \rightarrow e^+e^-\mu^+\mu^-}$$

is measured from the data by selecting events with two detected muon tracks, low total visible energy and a SAT-tagged (see Small Angle Tagger system in Chapter 4) charged track with $\geq$ 1 GeV energy deposition due to the scattering electron or positron. The SAT tag requirement is very useful for removing background to $e^+e^- \rightarrow e^+e^-\mu^+\mu^-(\gamma)$ events from (radiative) muon and tau pair events. The ratio of radiative (where the emitted photon may be from the external electron/positron legs or from the internal muon legs) to non-radiative $e^+e^- \rightarrow e^+e^-\mu^+\mu^-$ events is found to be $\sim 0.012 \pm 0.005$ where the error is statistical and the .012 value is an average of the results where the selection criteria are varied (the total visible energy is varied between 14–24 GeV, and a cut on the vector sum of the tracks' momenta transverse to the beam direction of < 2.5 GeV is sometimes included).

Monte Carlo GGDEPA $e^+e^- \rightarrow e^+e^-\mu^+\mu^-$ events are generated (no photon) and passed through a revised set of tau event selection criteria in order to estimate this background. The revised cuts do not include the requirements of a detected photon or of a large event acoplanarity. The acoplanarity cut is removed because its efficiency for eliminating $e^+e^- \rightarrow e^+e^-\mu^+\mu^-$ events is much higher than for $e^+e^- \rightarrow e^+e^-\mu^+\mu^-\gamma$ events and because the double equivalent photon approximation may not adequately model the acoplanarity of two-photon events.[51] Multiplying the measured rate of radiative events by the number of Monte Carlo $e^+e^- \rightarrow e^+e^-\mu^+\mu^-$ events

surviving the cuts, the $e^+e^- \rightarrow e^+e^-\mu^+\mu^-\gamma$ background contribution is estimated to be 3.2 ± 1.3 events.

The background from $e^+e^- \rightarrow e^+e^-\tau^+\tau^-$ events, estimated using the GGDEPA Monte Carlo and the exact tau selection criteria, is negligible. To check if $e^+e^- \rightarrow e^+e^-\tau^+\tau^-(\gamma)$ is a background, Monte Carlo $e^+e^- \rightarrow e^+e^-\tau^+\tau^-$ events are passed through a set of less stringent tau analysis cuts. The surviving number of events is multiplied by the rate of radiative events, though the rate used is that measured for $e^+e^- \rightarrow e^+e^-\mu^+\mu^-\gamma$ events and not for $e^+e^- \rightarrow e^+e^-\tau^+\tau^-\gamma$ (the radiative process, $e^+e^- \rightarrow e^+e^-\tau^+\tau^-\gamma$ is much harder to measure but the rate for $e^+e^- \rightarrow e^+e^-\tau^+\tau^-\gamma$ events should be smaller than for $e^+e^- \rightarrow e^+e^-\mu^+\mu^-\gamma$ events because of the larger tau mass). The result is less than 0.1 events and therefore this background is neglected.

The double equivalent photon approximation is useful for obtaining reasonably accurate simulation of two-photon events when the electron/positron scatter at low angles. Although the GGDEPA Monte Carlo events used for the background estimate include a simulation for cases where the electron scatters at large angles, another, more accurate two-photon Monte Carlo is employed to crosscheck the above results. In addition to the multiperipheral diagrams, the second Monte Carlo[52] also includes contributions from the other four-lepton diagrams shown in fig. A.2 (b-e). The Monte Carlo calculates exactly the complete matrix element squared for all 36 permutations of the Feynman diagrams shown in fig. A.2. This Monte Carlo indicates there is negligible background from the non-multiperipheral diagrams and gives results consistent with the predictions obtained from GGDEPA.

Because the Monte Carlo events do not include actual photons (from QED), it is necessary to use the $e^+e^- \rightarrow e^+e^-\mu^+\mu^-\gamma$ events from the data to obtain the spectral shapes for variables such as the μ-γ mass. In Chapter 5, the μ-γ mass spectrum from the signal and from backgrounds like $e^+e^- \rightarrow e^+e^-\mu^+\mu^-\gamma$ are used in a maximum

likelihood calculation to extract the branching ratio for the signal. Since the μ-γ mass spectrum in $e^+e^- \rightarrow e^+e^-\mu^+\mu^-\gamma$ events from data suffers from limited statistics, it is better to use smooth functions that parametrize this background in the likelihood calculation. Two particular choices, shown in fig. A.3, are tried, as well as the *data* spectrum itself in the likelihood fit; as shown in Chapter 5, the calculation is not very sensitive to exact shape of this small background.

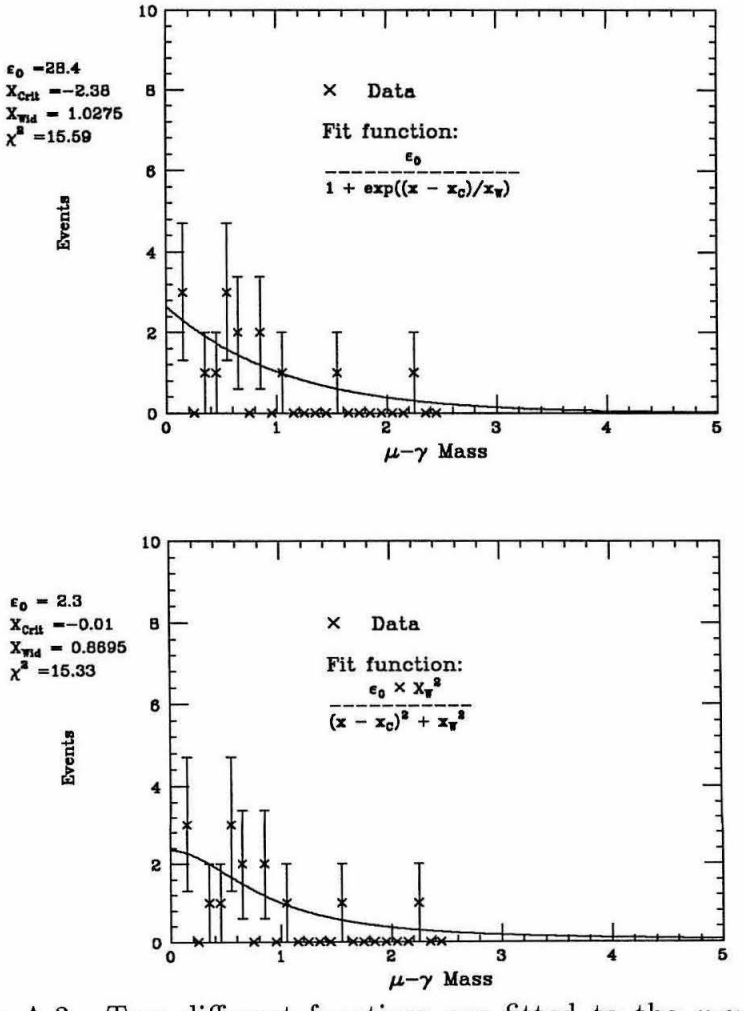

Figure A.3. Two different functions are fitted to the μ-γ mass spectrum for data $e^+e^- \rightarrow e^+e^-\mu^+\mu^-\gamma$ events.

A.2.6 Miscellaneous Small Backgrounds

There are two additional backgrounds, 1) hadronic events and 2) tau(-like) events with a "fake" photon due to spurious electronic noise in the calorimeter, to consider.

Accurately estimating the background from multihadronic events is very difficult because of the lack of experimental verification of low-charged-multiplicity jets in hadronic events at high energies. The LUND Monte Carlo[53] is used to estimate multihadronic background after performing the following check to see that the data and Monte Carlo agree reasonably in the charged-multiplicity distribution. Events with $\geq$ 6 charged tracks and event thrust axis lying within the detector ($|\cos\theta| < .7$), are selected from the data and from two different sets of LUND Monte Carlo events, one using the LUND parton shower evolution/LUND symmetric fragmentation scheme (Jetset version 6.3) and the other using the LUND second order matrix element/LUND symmetric fragmentation scheme (Jetset version 5.2). The number of charged tracks in each hemisphere (defined with respect to the thrust axis) are counted and the smaller of the two numbers is plotted in fig. A.4, and the larger in fig. A.5. Figure A.4 is of particular interest since it shows that there is acceptable agreement between Monte Carlo and data for jets (hemispheres, actually) with low-charged multiplicities in hadronic events; therefore, it is reasonable to use the Monte Carlo to estimate this small background. The number of hadronic events is expected to be $\sim 0.1 \pm .03$, where the error is from pion misidentification uncertainty. The estimate is based on the number of events passing all the tau selection criteria (except muon detector hits) and the total probability for pion punchthrough and decay (see misidentified tau background estimate).

Electronic noise in the calorimeter is a background when the shower algorithm reconstructs the noisy channels as a "photon" cluster with $\geq .3$ GeV energy in an event that would not have otherwise passed the *radiative* tau event selection requirement (the noise probability is measured using SAT Bhabha events – see Chapter 4, which

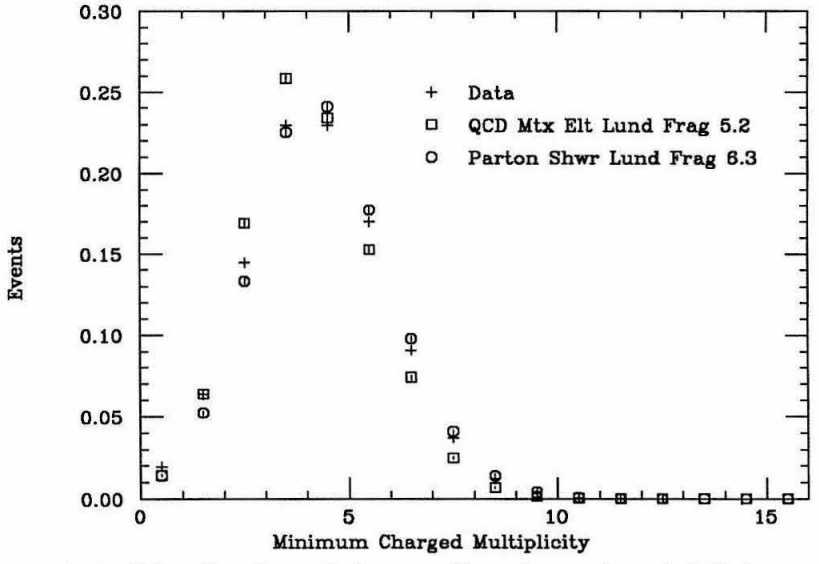

Figure A.4. Distribution of the smaller charged-multiplicity value between the two hemispheres in a hadronic event. The event selection criteria and Monte Carlo samples are described in the text.

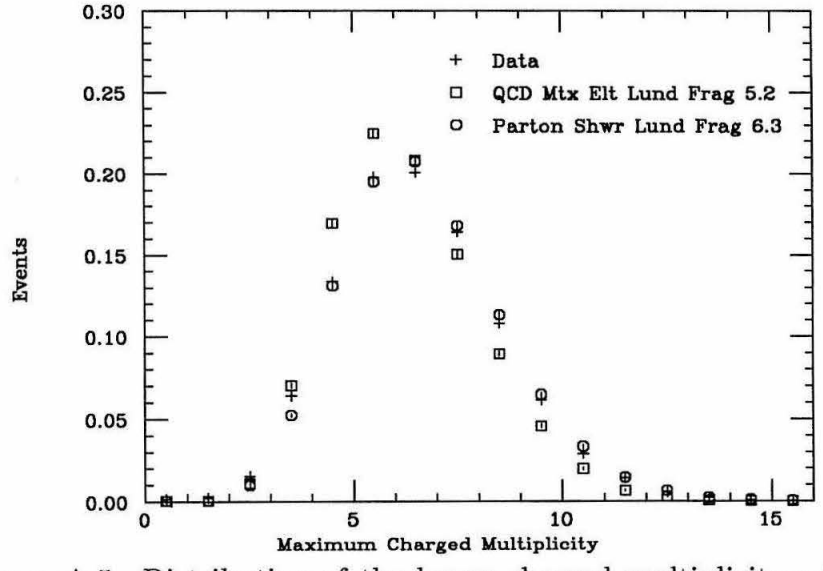

Figure A.5. Distribution of the larger charged multiplicity value between the two hemispheres in a hadronic event, which shows good agreement between the data and LUND Monte Carlo. The event selection criteria and Monte Carlo samples are described in the text.

also discusses the smaller probability of electronic noise correlated with the presence of a muon track in a calorimeter module). Using the probability for calorimeter noise, its energy distribution and angular distribution, non-radiative Monte Carlo tau events are altered to include a fake photon and passed through the tau selection cuts. The energy spectrum for fake photons is fairly soft and so other spectra that depend on it, such as the μ-γ mass, are also distributed at low energies (see fig. A.6). The number of predicted events is very small, about 0.1 events. The fake photon contribution is combined with the hadronic background to give 0.2 ± 0.06 events.

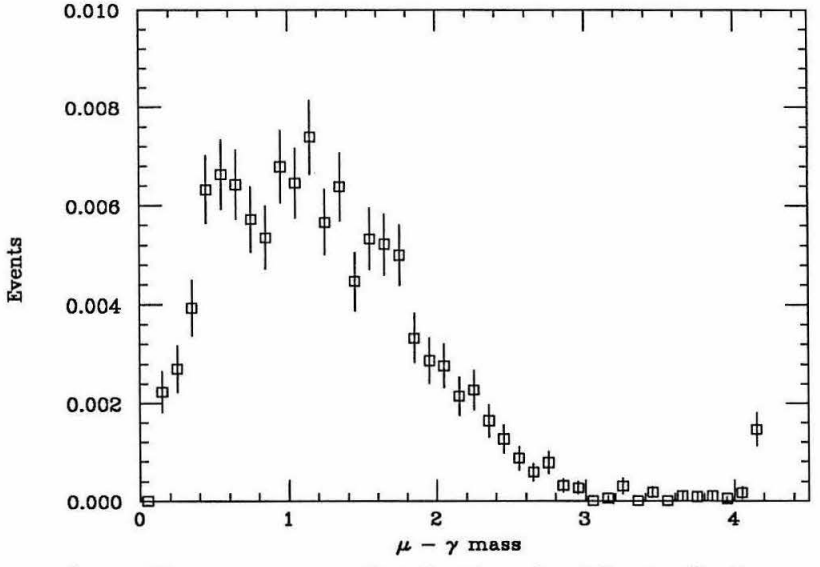

Figure A.6. The μ-γ mass distribution for Monte Carlo $\tau^- \rightarrow \nu_\tau \mu^- \bar{\nu}_\mu$ events combined with a "photon" simulating electronic noise in the calorimeter.

References

1. M.L. Perl, Ann. Rev. Nucl. Part. Sci. **30,** 299 (1980).
2. Y.S. Tsai, Phys. Rev. **D4,** 2821 (1971).
3. B.C. Barish, R. Stroynowski, Phys. Reports **157,** 1 (1988).
4. F. Gilman and S. Rhie, Phys. Rev. **D31,** 1066 (1985).
5. T.N. Truong *et al.*, Phys. Rev. **D30,** 1509 (1984).
6. M.L. Perl, SLAC-PUB-4632 (1988).
7. R. Baltrusaitis *et al.*, Phys. Rev. Lett. **55,** 18 (1985).
8. W.W. Ash *et al.*, Phys. Rev. Lett. **55,** 20 (1985).
9. W. Bartel *et al.*, Phys. Lett. **182B,** 216 (1986).
10. B. Adeva *et al.*, Phys. Lett. **179B,** 1 (1986).
11. W. Bartel *et al.*, Z. Phys. **31C,** 360 (1986).
12. W.J. Marciano and A. Sirlin, Phys. Rev. Lett. **61,** 1815 (1988).
13. Particle Data Group, Phys. Lett. **204B,** 1 (1988).
14. K.G. Hayes SLAC-PUB-5061(1989).
15. F. Gilman, Phys. Rev. **D35,** 3541 (1987).
16. H.J. Behrend *et al.*, DESY-89-126 (1989).
17. S. Jadach and Z. Was, Comp. Phys. Comm. **36,** 191 (1985).
18. K. Riles, Ph.D. thesis, Stanford University, SLAC-342.

19. E.D. Commins and P.H. Bucksbaum, *Weak Interaction of Leptons and Quarks*, Cambridge, 1983, Cambridge University Press.

20. F.A. Berends *et al.*., Acta Phys. Pol. **B14** 413 (1983).

21. M. Gold, Ph.D. thesis, University of California, Berkeley, LBL-22433 (1986).

22. G. Bonneau and F. Martin, Nuc. Phys. B**27,** 381 (1971).

23. F.A. Berends and R. Kleiss, Nuc. Phys. B**177,** 237 (1981).

24. S. Jadach and Z. Was, Acta Phys. Pol. **B15** 1151 (1984).

25. A more detailed description of QCD and the structure of hadrons is given in F. Halzen and A.D. Martin, *Quarks and Leptons*, John Wiley and Sons, 1984.

26. A more detailed description of the weak interaction theory can be found in E.D. Commins and P.H. Bucksbaum, *Weak Interaction of Leptons and Quarks*, Cambridge, 1983, Cambridge University Press.

27. S.M. Berman, Physical Review **112,** 267 (1958).

28. See equation 17b. R.E. Behrends, R.J. Finkelstein and A. Sirlin, Physical Review **101,** 866 (1956).

29. A. Lenard, Physical Review **90,** 968 (1953).

30. W.T. Ford *et al.*, Phys. Rev. **D36,** 1971 (1987).

31. T. Kinoshita and A. Sirlin, Physical Review Letters **2,** 177 (1959).

32. B. LeClaire, Ph.D. thesis, Stanford University, SLAC-321 (1987).

33. D. Karlen, Mark II memo, September 1987. Ph.D. thesis, Stanford University, SLAC-325 (1988).

34. M. Nelson, Ph.D. thesis, University of California, Berkeley, LBL-16724 (1983).

35. D. Karlen, Ph.D. thesis, Stanford University, SLAC-325 (1988).

36. C.W. Fabjan and R. Wigmans, 1989, CERN-EP-89-64.

37. C. Blocker, Ph.D. thesis, University of California, Berkeley, LBL-10801 (1980).

38. R.L. Ford and W.R. Nelson, computer code EGS Version 3, Stanford Linear Accelerator Center, SLAC-PUB-0210 (1978).

39. K. Hayes, Ph.D. thesis, Stanford University, SLAC-237 (1981).

40. R. Ong, Ph.D. thesis, Stanford University, SLAC-320.

41. F.A. Berends, P.H. Daverveldt, and R. Kleiss, Nuc. Phys. **B253,** 421 (1985).

42. D. Stoker *et al.*, Phys. Rev. **D39,** 1811 (1989).

43. J.R. Smith, Ph.D. thesis, University of California, Davis, RX-1171 (1982).

44. S. Jadach *et al.*, KORAL-Z3 LONG WRITE-UP, draft version 3.6, June 1989.

45. F. James and M. Roos, Comp. Phys. Comm. **10** 343 (1985).

46. A.G. Frodesen, O. Skjeggestad, and H. Tofte, *Probability and Statistics in Particle Physics*, Norway, 1979, Universitetsforlaget.

47. B.K. Heltsley CLNS-87-117(1987).

48. P. Burchat *et al.*, Phys. Rev. **D35,** 27 (1987).

49. J.M. Yelton *et al.*, Phys. Rev. Lett. **56,** 812 (1986).

50. R.H. Dalitz and D.R. Yennie, Phys. Rev. **D105,** 1598 (1957).

51. S.J. Brodsky, T. Kinoshita, and H. Terazawa, Phys. Rev. **D4,** 1532 (1971).

52. F.A. Berends, P.H. Daverveldt, and R. Kleiss, Nuc. Phys. **B253,** 441 (1985). F.A. Berends, P.H. Daverveldt, and R. Kleiss, Comp. Phys. Comm. **40,** 271 (1986).

53. T. Sjöstrand, Comp. Phys. Comm. **39,** 347 (1986). T. Sjöstrand and M. Bengtsson, Comp. Phys. Comm. **43,** 367 (1987). A. Bäcker, Z. Phys. **C12,** 161 (1982).